Frequency conversion by the parametric interaction of space-charge waves in thin-film semiconductor structures with negative differential conductivity

A. I. Mikhaĭlov and S. A. Sergeev

(Submitted July 15, 1996)
Pis'ma Zh. Tekh. Fiz. **22**, 75–78 (December 26, 1996)
[S1063-7850(96)03812-8]

A promising class of functional microelectronic microwave devices are those based on space-charge waves (SCWs) in semiconductors with negative differential conductivity (NDC), resulting from intervalley electron transitions in strong electric fields. In Ref. 1 it is pointed out that these devices, of which a typical example is a thin-film traveling-wave amplifier, can be used as amplifiers, heterodynes (with feedback), delay lines, and switches. In Refs. 2–4 it is shown theoretically and experimentally that the parametric operating regime of such an amplifier with low-frequency pumping not only increases the limiting SCW amplification frequency, but it also makes it possible to add at least two possible functions: mixing with a frequency shift and controllable filtering with tuning by varying the pump frequency. Theoretical investigations of the interaction (parametric amplification, conversion) of space-charge waves in semiconductors with NDC ordinarily employ one-dimensional spatial models, which limits their applicability, because in real amplifiers thin-film semiconductor structures with a working layer whose thickness is comparable to the wavelength of the space charge are used to prevent Gunn oscillations.

In the present Letter, the results of a theoretical investigation of parametric frequency conversion in thin-film semiconductor structures with negative differential conductivity are reported and the effect of the pump parameters and film thickness on the conversion factor is studied.

In the present Letter we investigate frequency conversion theoretically using an approach similar to that described in detail in Ref. 5, where a mathematical model was formulated for analyzing the parametric interaction under study. The coordinate system is chosen so that the y and z axes are oriented perpendicular and parallel, respectively, to the film plane, the latter axis lying in the middle of the film. A strong dc electric field parallel to the film plane and the z axis is produced in the n-GaAs film; the intensity E_0 of this field corresponds to the section of NDC on the curve of the electron drift velocity versus E_0. Let us assume that a more intense pump wave with frequency $f_p < f_s$ (low-frequency pump) and amplitude E_{p0} is also excited in the n-GaAs film in addition to a weak SCW with frequency f_s (signal). As a result of the nonlinearity of the semiconductor, a wave at the idler frequency $f_i = f_s - f_p$ arises in the electron flow. The analysis in Ref. 5 led to a system of two first-order ordinary differential equations for the amplitudes of the coupled signal and idler frequencies. As a result of the numerical solution of this system, in Ref. 5 the amplitudes E_s and E_i associated with the signal f_s and idler f_i frequencies were calculated at the end of the interaction section of length l and the transfer coefficient at the frequency f_s was calculated according to the formula

$$L = 20 \cdot \log(E_s / E_{s0}), \tag{1}$$

where E_{s0} is the amplitude of the space-charge wave of the signal in the initial section of the interaction.

In the analysis of the results in Ref. 5 it was pointed out that effective frequency conversion can be obtained with the

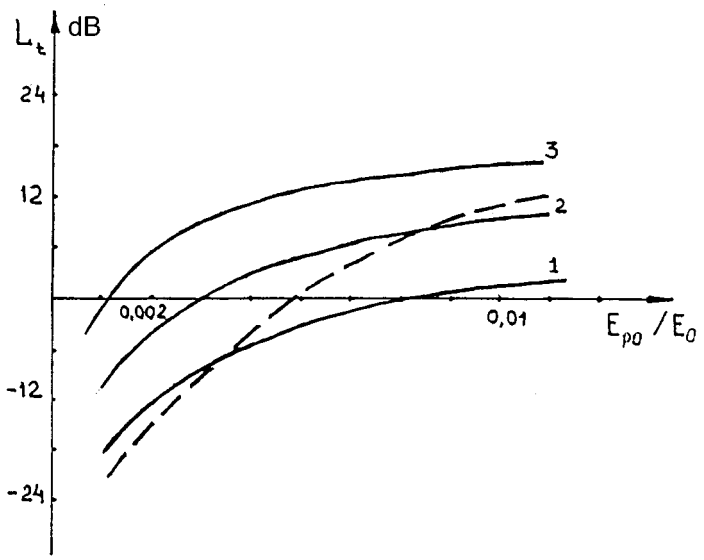

FIG. 1. Conversion factor L_t versus E_{p0}/E_0: $f_s = 35$ GHz, $f_p = 20$ GHz, $f_i = 15$ GHz, $T = 10$ μm, $l = 40$ μm (curve 1), 50 μm (2) and 60 μm (3). Dotted curve — l versus E_{p0}/E_0 for $l = 60$ μm.

 1063-7850/97/010001-02$10.00

parametric interaction studied. In the present Letter we report the computational results for the conversion factor:

$$L_t = 20 \cdot \log(E_i / E_{s0}). \quad (2)$$

For numerical calculations we employed the values of the parameters and physical quantities which are characteristic for *n*-GaAs: The relative permittivity is 12.5, for $E_0 = 5.5$ kV/cm the drift velocity is 1.7×10^7 cm/s, and the diffusion coefficient is 160 cm^2/s. The curves of the differential electron mobility versus frequency, which were calculated by the Monte Carlo method in Ref. 6, correspond to the same value of E_0. The variable parameters in the calculations were f_s, f_p, f_i, E_{p0}/E_0, l, and the film thickness T. The computational results are presented in Fig. 1, which displays curves of L_t versus E_{p0}/E_0 for $f_s = 35$ HGz, $f_p = 20$ GHz, and $f_i = 15$ GHz with film thickness $T = 10$ μm and interaction length $l = 40$ μm (curve 1), 50 μm (2), and 60 μm (3). For comparison, a curve of L versus E_{p0}/E_0 calculated according to Eq. (1) for the same frequencies f_s, f_p, and f_i with film thickness $T = 10$ μm and $l = 60$ μm (dotted curve) is also presented in Fig. 1.

As one can see from the figure, L_t increases with increasing pump amplitude and for certain values ot E_{p0}/E_p it becomes a positive quantity ($L_t > 0$ is the autodyne conversion). The computational results also show that increasing l results in larger L_t, since f_i in the case chosen for the calculations lies below the limiting frequency of the amplified SCWs, as a result of which the idler SCW is increasing even in the absence of parametric interaction. As a result of the weakening of the space charge and the fact that some lines of force exit the film, a decrease of the film thickness T results in a decrease of both L and L_t.

In summary, the results of the present work show that, in agreement with the experimental results of Ref. 4, the parametric interaction of surface-charge waves in *n*-GaAs-based thin-film semiconductor structures with negative differential conductivity with a low-frequency pump can be used for effective frequency conversion in the 8-mm range.

[1] A. A. Barybin *et al.*, Mikroélektronika **8**, 3 (1979).
[2] V. A. Ivanchenko, B. N. Klimov, and A. I. Mikhaĭlov, Fiz. Tekh. Poluprovodn. **13**, 1172 (1979) [Sov. Phys. Semicond. **13**, 687 (1979)].
[3] V. A. Ivanchenko, Yu. M. Ignat'ev, and A. I. Mikhĭlov in *Interaction of Electromagnetic Waves with Semiconductors and Semiconductor–Insulator Structures* [in Russian], Saratov University Press, Saratov, 1988, Part 2, pp. 117–118.
[4] V. A. Ivanchenko and A. I. Mikhaĭlov in *Abstracts of Reports at the All-Union Conference on ''Electronics: Information Converters''* [in Russian], Nizhniĭ Novgorod, Moscow, 1991, pp. 12–14.
[5] A. I. Mikhaĭlov and S. A. Sergeev, Izv. Vyssh. Uchebn. Zaved., Radioélektron. **38**, 43 (1995).
[6] H. D. Rees, Solid State Commn. **7**, 267 (1969).

Translated by M. E. Alferieff

Influence of amplitude modulation of a light beam on electron interference: the Aharonov–Bohm effect

A. N. Ageev and S. Yu. Davydov

A. F. Ioffe Physicotechnical Institute, Russian Academy of Sciences, St. Petersburg
(Submitted October 28, 1996)
Pis'ma Zh. Tekh. Fiz. **23**, 9–12 (January 12, 1997)

Expressions are derived for the change in the width of the central peak in the Aharonov–Bohm effect. [S1063-7850(97)00201-2]

Since the discovery of the Aharonov–Bohm effect,[1] researchers have concentrated their attention on studying the phase characteristics of electron waves in static magnetic fields,[2] whereas the influence of a varying electromagnetic field on the Aharonov–Bohm effect has only been examined in a few publications.[3–6] The authors of Ref. 4 derived an expression relating the broadening of the central interference maximum to the frequency of light ω, the amplitude of the vector potential created by it A_0, and the electron velocity v. These investigations were continued in Refs. 5 and 6. In the present paper the model discussed in Refs. 4–6 is used to analyze the influence of amplitude modulation of an optical signal on the interference pattern in the Aharonov–Bohm effect.

We express the vector potential A in the form[7]

$$A=A_0(1+m\ \cos\ \Omega t)\cos\ \omega t, \tag{1}$$

where $m=\Delta A/A_0$ is the modulation coefficient and Ω is the frequency of the modulating signal. It was shown in Ref. 4 that interference between two electron beams diffracted from two slits separated by the distance d is determined by the probability P

$$P=\frac{1}{2}\left\{1+\cos\left[\frac{2ev}{\hbar}\int_0^t A dt+\frac{ev}{\hbar}\int_{-\tau}^0 A dt-\omega_e\tau\right]\right\}. \tag{2}$$

Here e is the electron charge, $\hbar$ is the reduced Planck's constant, c is the velocity of light, τ is time interval for electrons diffracted from different slits to arrive at the same point on the screen, and ω_e is the angular frequency of the electron wave. Substituting Eq. (1) into Eq. (2) gives

$$P=\frac{1}{2}\left\{1+\cos\left[R\cdot F(t)+\frac{1}{2}R\cdot F(\tau)-\omega_e\tau\right]\right\}, \tag{3}$$

where

$$R=\frac{2evA_0}{\hbar\omega}, \tag{4}$$

$$F(t)=\sin\ \omega t+m\omega\left[\frac{\sin(\omega-\Omega)t}{\omega-\Omega}+\frac{\sin(\omega+\Omega)t}{\omega+\Omega}\right]. \tag{5}$$

We expand expression (5) in the small parameter Ω/ω, which gives

$$F(t)=\sin\ \omega t+2m\left[\sin\ \Omega t\cdot\cos\ \omega t-\frac{\Omega}{\omega}\cos\ \Omega t\cdot\sin\ \omega t\right]. \tag{6}$$

A similar expression is obtained for $F(\tau)$. If the detection system records the buildup of diffracted electrons at each point on the screen, the condition corresponding to the half-height of the central maximum is[4]

$$\omega_e\tau-\left[R\cdot F(t)+\frac{1}{2}R\cdot F(\tau)\right]_{\max}=\frac{\pi}{2}. \tag{7}$$

It can be shown that the principal correction to the function $F(t)$ caused by the modulation is $(-2m\Omega/\omega)$ and consequently

$$F_{\max}(t)\cong 1-2m\frac{\Omega}{\omega}. \tag{8}$$

The correction to the function $F(\tau)$ may be disregarded since $\omega\tau$ is small. Then repeating all the procedures of Ref. 5, we obtain the relative angle for the central diffraction peak

$$\frac{\theta-\theta_0}{\theta_0}=\frac{4}{\pi}\frac{evA_0}{\hbar\omega}\left(1-2m\frac{\Omega}{\omega}+\frac{\pi}{4}\frac{\omega}{\omega_e}\right). \tag{9}$$

Thus amplitude modulation of the optical signal narrows the central diffraction peak.

It is interesting to consider the influence of amplitude modulation on the contrast of the diffraction pattern. By repeating the calculations made in Ref. 6, one can show that the d.c. (low-frequency) component of the diffraction probability $P_{d.c}$ has the form

$$P_{d.c.}=\frac{1}{2}\left\{1+\cos(\beta\omega_e\tau)J_0\left[R\left(1-2m\frac{\Omega}{\omega}\right)\right]\right\}, \tag{10}$$

where $\beta=1-\omega R/2\omega_e$. Thus, the contrast of the interference pattern

$$K\equiv(P_{d.c.\ \max}-P_{d.c.\ \min})/(P_{d.c.\ \max}+P_{d.c.\ \min})$$

is

$$K=\left|J_0\left[R\left(1-2m\frac{\Omega}{\omega}\right)\right]\right|. \tag{11}$$

From this it follows that when $R(1-2m\Omega/\omega)<2.40$ (this is the first zero of the Bessel function J_0), an increase in $m\Omega/\omega$ enhances the contrast of the interference pattern. Conversely, in the range

$$2.40<R(1-2m\Omega/\omega)<3.84,$$

i.e., on the rising part of the function $|J_0[R(1-2m\Omega/\omega)]|$, an increase in $m\Omega/\omega$ reduces K, and so forth. This follows from the oscillating nature of the Bessel function: on the decaying sections of $|J_0|$ an increase in $m\Omega/\omega$ enhances the contrast whereas on the rising parts of $|J_0|$, the opposite effect occurs.

Amplitude modulation therefore narrows the central interference maximum and for small $R<2.40$ enhances the contrast of the diffraction pattern in the Aharonov–Bohm effect.

This work was supported by the Russian Fund for Fundamental Research (Grant RFFI 95-02-04064-a).

[1] Y. Aharonov and D. Bohm, Phys. Rev. **115**, 485 (1959).
[2] M. Peshin and A. Tonomura, Lecture Notes Phys. **340**, 3 (1984).
[3] S. M. Roy and V. Singh, Nuovo Cimento **79**, 391 (1984).
[4] B. Lee, E. Yin, T. K. Gustafson, and R. Chiao, Phys. Rev. A **45**, 4319 (1992).
[5] A. N. Ageev and S. Yu. Davydov, Pis'ma Zh. Tekh. Fiz. **21**(23), 71 (1995) [Tech. Phys. Lett. **21**, 982 (1995)].
[6] A. N. Ageev and S. Yu. Davydov, Pis'ma Zh. Tekh. Fiz. **22**(4), 70 (1996) [Tech. Phys. Lett. **22**, 165 (1996)].
[7] V. V. Potemkin, *Radiophysics* [in Russian], Moscow State University, Moscow (1988).

Translated by R. M. Durham

Influence of active oxygen on the superconducting properties of an yttrium ceramic investigated by a diffraction method

M. U. Kalanov, M. S. Paĭzullakhanov, R. Kh. Maminov, V. M. Rustamova, S. N. Abdurakhmanova, and I. I. Akhmedov

Institute of Nuclear Physics, Academy of Sciences of the Republic of Uzbekistan, Tashkent
(Submitted April 18, 1996)
Pis'ma Zh. Tekh. Fiz. **23**, 13–18 (January 12, 1997)

A diffractometric method of determining the amount of oxygen in intergranular media is described and the superconducting properties of YBaCuO ceramic are related to the intergranular oxygen content. [S1063-7850(97)00301-7]

It has been established that the superconducting properties of YBaCuO ceramic are very sensitive to the oxygen content.[1] Most existing methods determine the concentration of oxygen atoms averaged over the entire volume of high-temperature superconductors.[2] However, a knowledge of this average concentration is insufficient to explain many of the detailed effects observed in these materials. An example of these effects is the loss of superconducting properties in the orthorhombic phase $YBa_2Cu_3O_{7-\delta}$ at $\delta=0.1$ (Ref. 3). This observation indicates that the superconducting properties of this phase are not uniquely determined by a uniform oxygen distribution. In fact, it has been shown by thermostimulated desorption that some of the oxygen atoms in a YBaCuO ceramic are in a weakly bound active state, i.e., in boundary layers between structural units (such as granules and twins), and are easily removed under various external influences.[4,5] In this context, it has also been noted that the products of high-temperature self-propagating synthesis contain a significantly larger amount of weakly bound oxygen compared with ceramics synthesized directly in a furnace.[4] It has therefore become necessary to make a reliable determination of the amount of active oxygen and its influence on the superconducting properties of a granular YBaCuO system as a whole.

The experiment was carried out using a DRON-UM1 (CuK_α) x-ray diffractometer fitted with additional collimating systems to improve the signal-to-noise ratio at small scattering angles.[6] An advantage of this method is that in a single experiment we can obtain information on the phase state of the sample, the structural parameters, and the separate concentrations of oxygen in the bulk of the granules and in the intergranular media. The samples were textured superconducting yttrium ceramic tablets 12 mm in diameter and 0.6 mm thick. The degree of texturing was $F_t=0.64$ (Ref. 5). In the initial state before heat treatment, the composition of the sample was $YBa_2Cu_3O_{6.85}$, slightly below stoichiometric, with the lattice parameters $a=3.823$ Å, $b=3.882$ Å, and $c=11.677$ Å. The superconducting transition temperature was determined by the van der Pauw method and corresponded to $T_c=85$ K with a width of 2 K. With the aim of varying the concentration of active intergranular oxygen atoms, the samples underwent isothermal annealing in vacuum (10^{-4} Pa) at 473 K during which the intragranular oxygen content remained constant. The hold time was 5 h. The concentration of lattice oxygen atoms in the bulk of the granules was determined using the lattice parameter C in accordance with the empirical law

$$(7-\delta)=62.694-4.785C \tag{1}$$

and by measuring the distance between the diffraction peaks (200) and (020) (Ref. 6).

The problem of determining the oxygen content in the intergranular spaces is not a trivial one. A detailed analysis of the intensity of the diffraction peaks observed for YBaCuO ceramic as a function of temperature revealed that some structural peaks of different parity are extremely sensitive to the oxygen content in the intergranular media. The diffraction peak doublet (012) and (102) proved most suitable for x-ray diffraction. Since these peaks occur at small scattering angles ($2\theta\sim 27-28°$), the amplitude of the scattering of x-rays by oxygen atoms is greatest in this case and the negative influence of angular and thermal factors on the intensity of these peaks is the smallest. For a homogeneous orthorhombic phase with $0\leqslant\delta\leqslant 0.5$ the ratio of the structure factors of these peaks, omitting the constant coefficients, is given by

$$\frac{F(012)}{F(102)}=\frac{(f_{\mathrm{Ba}}+f_{\mathrm{Cu}}-f_{\mathrm{Y}})-f_O(1-\delta)}{(f_{\mathrm{Ba}}+f_{\mathrm{Cu}}-f_{\mathrm{Y}})-f_O\delta}, \tag{2}$$

where f_{Ba}, f_{Cu}, f_{Y}, and f_O are the scattering amplitudes of barium, copper, yttrium, and oxygen atoms, respectively. The final empirical dependence of the oxygen content $(7-\delta)_g$ in the intergranular layers on the ratio I_{012}/I_{102} of the peak intensities is a square root dependence and may be expressed as follows:

$$(7-\delta)_g=\frac{126.963(I_{012}/I_{102})^{1/2}+227.053}{27.131(I_{012}/I_{102})^{1/2}+27.333}. \tag{3}$$

When the intergranular oxygen content varies between 7 and 6.5, the ratio $(I_{012}/I_{102})^{1/2}$ varies in the range $0.5674\leqslant(I_{012}/I_{102})^{1/2}\leqslant 1.0$. It follows from expression (3) that the error in the determination of the oxygen content depends mainly on the statistical error in the measurement of

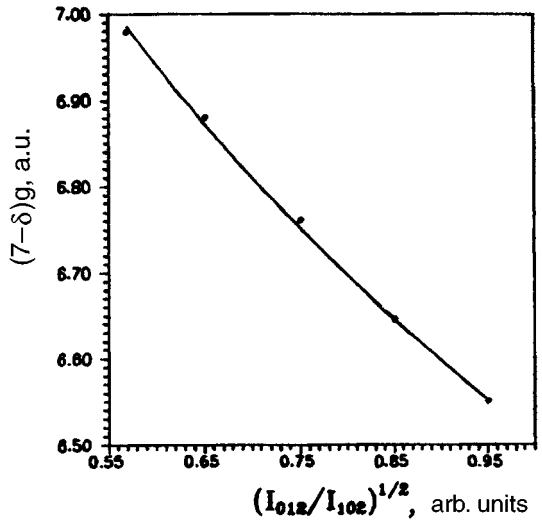

FIG. 1. Intergranular oxygen content $(7-\delta)_g$ versus intensity ratio of (012) and (102) peaks: circles — experimental values, solid curve — calculations using Eq. (3).

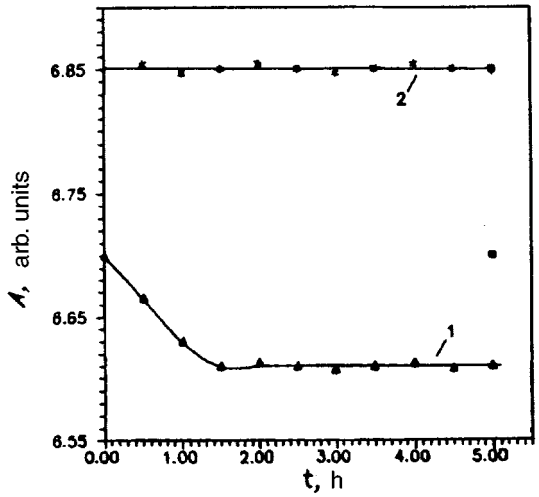

FIG. 2. Time dependence of oxygen content under vacuum isothermal annealing: curve *1* — oxygen content in intergranular media, curve *2* — oxygen content in bulk of granules, ■ — oxygen content in vacuum heat-treated samples after regenerative annealing in air.

the peak intensities, which may be reduced by choosing the appropriate exposure to record the diffraction patterns.

Figure 1 gives the concentration $(7-\delta)_g$ plotted as a function of $(I_{012}/I_{102})^{1/2}$, which differs almost negligibly from linear. The experimental points are a good fit to the solid curve calculated according to Eq. (3). The measurement error in this case was ± 0.005 a.u. Figure 2 gives the oxygen content in the bulk of the granules (curve *2*) and in the intergranular media (curve *1*) plotted as a function of the hold time for soft vacuum heat treatment at $T=473$ K. It can be seen that when the compositions of the initial YBaCuO ceramic is nonstoichiometric $[(7-\delta)<7]$, the concentration of structured oxygen in weakly ordered intergranular media is considerably lower than the concentration of lattice oxygen in the bulk of the granule (the points at $t=0$ in Fig. 2). The critical superconducting transition temperature $T_c=85$ K corresponds to an intergranular oxygen content $(7-\delta)_g=6.70$ a.u. As the hold time was increased to $t=1.5$ h, the concentration of structured oxygen atoms in the intergranular media decreased linearly to $(7-\delta)_g=6.61$ a.u. for this sample. The observed removal of weakly bound oxygen atoms from intergranular structures was accompanied by a 9.2% increase in the background below the diffraction peaks compared with the initial level. In the range $t=1.5$–5 h the curve $(7-\delta)_g(t)$ reaches a plateau, i.e., the mechanism of structural rearrangement involving intergranular oxygen atoms reaches saturation.

It was found that when the intergranular oxygen content was reduced to $(7-\delta)_g=6.61$ a.u., the superconducting transition temperature dropped to $T_c\sim 78$ K. It is important to note that, the oxygen content $(7-\delta)$ in the bulk of the granule remained constant over the entire hold time ($t=0$–5 h) under heat treatment (Fig. 2, curve *2*). This synchronous correlation between the parameters $(7-\delta)$ for the granules and $(7-\delta)_g$ for the intergranular space, and also with the increase in the background level near the (012) and (102) peaks indicates that some of the active structured oxygen is incorporated in the amorphous phase of the intergranular media. This structural rearrangement of the intergranular media with a change in the ratio of the crystalline and amorphous phases towards the latter causes an abrupt deterioration in the superconducting properties of YBaCuO ceramic. In this case the superconducting transition temperature T_c decreases from 85 to 78 K. Under our experimental conditions this process was reversible.

Subsequent heat treatment of the samples in air at 723 K for 5 h completely restored the oxygen content in the intergranular media to its initial value $[(7-\delta)_g=6.70$ a.u.] and thus restored the critical superconducting transition temperature to $T_c=85$ K. It should be stressed that the entire experimental cycle described (vacuum heat treatment at 473 K and regenerative annealing in air at 723 K) can be accurately reproduced both in the change in the intergranular oxygen content and in complete conservation of the bulk oxygen content. Increasing the vacuum heat treatment temperature to 573 K altered the oxygen content in the bulk of the granules and therefore hindered the process.

These results suggest that the superconducting properties of yttrium ceramic depend strongly on the behavior of the active oxygen in the intergranular media and also at twinning boundaries, blocks, and other submicron structural units. Under external influences, complex structural rearrangement takes place in the intergranular media involving weakly bound oxygen and these processes influence the superconducting properties of the YBaCuO ceramic. Further investigations are required to identify the mechanisms for these processes.

[1] Yu. M. Baĭkov, E. A. Shalkova, and T. A. Ushakova, Sverkhprovodimost' (KIAE) **6**, 449 (1993).
[2] A. Amannazarov and A. I. Sharnopol'skiĭ, *Methods and Instruments for Determination of Oxygen* [in Russian], Khimiya, Moscow (1988).
[3] A. G. Merzhanov, Yu. N. Barinov, I. P. Borovinskaya *et al.*, Pis'ma Zh. Tekh. Fiz. **15**(11), 1 (1989) [Sov. Tech. Phys. Lett. **15**, 413 (1989)].

[4] A. G. Merzhanov, A. V. Makarov, G. V. Romanov *et al.*, Pis'ma Zh. Tekh. Fiz. **15**(11), 4 (1989) [Sov. Tech. Phys. Lett. **15**, 414 (1989)].
[5] M. S. Paĭzullakhanov, M. U. Kalanov *et al.*, Sverkhprovodimost' (KIAE) **5**, 2048 (1992). [Superconductivity **5**, 1946 (1992)].
[6] M. U. Kalanov, R. B. Rasulov *et al.*, Preprint No. 9-441 [in Russian], Institute of Nuclear Physics, Academy of Sciences of the Republic of Uzbekistan, Tashkent (1989).

Translated by R. M. Durham

Nonequilibrium fluctuations of the rates of steady-state chemical reactions

A. P. Grigin

A. N. Frumkin Institute of Electrochemistry, Russian Academy of Sciences, Moscow
(Submitted August 6, 1996)
Pis'ma Zh. Tekh. Fiz. **23**, 19–21 (January 12, 1997)

Nonequilibrium fluctuations of the rate of a molecular association–dissociation reaction are analyzed. The correlation function of a Langevin source is obtained as a function of a nonlinear dissipative coefficient. © *1997 American Institute of Physics.* [S1063-7850(97)00401-1]

In the approximation of local thermodynamic equilibrium fluctuations are determined by Langevin sources whose correlation functions depend on dissipative coefficients.[1] If the system is linear and nonequilibrium, the correlation functions of the Langevin source have the same form as those for an equilibrium system. If the system is nonlinear and nonequilibrium, the correlation functions of the Langevin source will generally have a different form. In order to determine these correlation functions, only the thermodynamic forces are varied and all the other parameters are assumed to be constant.

Let us consider nonlinear fluctuations for the case of a molecular association–dissociation reaction: let substance A combine with substance B to form reaction product C. This reaction may be represented schematically as

$$A+B\rightleftarrows C. \tag{1}$$

The mathematical expression describing the rate of this reaction has the form

$$I=wn_1n_2-vm, \tag{2}$$

where n_1 is the concentration of particles A, n_2 is the concentration of particles B, M is the concentration of particles C, w is the probability per unit time of formation of molecule C from atoms A and B, v is the probability of dissociation of molecule C, and I is the reaction rate.

Equation (2) expresses the rate of an association–dissociation reaction in terms of corpuscular kinetic theory. In the local-equilibrium approximation the reaction rate can also be expressed in terms of nonequilibrium thermodynamics, i.e., as the function $I=I(\Delta\mu)$, where $\Delta\mu$ is the difference between the chemical potentials on the left- and right-hand sides of Eq. (1):

$$\Delta\mu=\Delta\mu_0+T\ \ln\left(\frac{n_1n_2}{m}\right), \tag{3}$$

where $\Delta\mu_0$ is a function of pressure and temperature.

The explicit form of the function $I(\Delta\mu)$ may be determined by using the principle of correspondence between the kinetic and thermodynamic descriptions of the reaction rate. The correspondence principle for this reaction may be formulated as: expressions giving I in kinetic and thermodynamic variables should have the same functional form for the particle concentration.[2] The correspondence principle was used in Ref. 2 to obtain the following expression for $I(\Delta\mu)$:

$$I=\varkappa(n_1n_2)^{\alpha}m^{1-\alpha}[e^{(1-\alpha)\frac{\Delta\mu}{T}}-e^{-\alpha\frac{\Delta\mu}{T}}], \tag{4}$$

where $\varkappa$ and α are the linear and nonlinear dissipative coefficients, respectively. In this case the following relations are satisfied

$$w=\varkappa e^{(1-\alpha)\frac{\Delta\mu_0}{T}},\quad v=\varkappa e^{-\alpha\frac{\Delta\mu_0}{T}}, \tag{5}$$

In order to find the current fluctuations δI, we shall postulate that the system is locally in equilibrium and all the thermodynamic parameters do not depend on time. In this approximation the methods described in Ref. 3 may be used to find the fluctuations and we introduce the correspondence:

$$\dot{X}\rightarrow\delta I;\quad X\rightarrow\delta(\Delta\mu). \tag{6}$$

We write the Langevin equation for X

$$\dot{X}+\lambda X=\xi(r,t), \tag{7}$$

where $\xi(r,t)$ is a Langevin source of reaction rate fluctuations. The correlation function ξ may be expressed in the form[3]

$$\langle\xi(r_1,t_1)\xi(r_2,t_2)\rangle=2t\lambda\,\delta(r_1-r_2)\,\delta(t_1-t_2). \tag{8}$$

To find λ we vary Eq. (4) with respect to $\Delta\mu$ to give

$$\lambda=\varkappa(n_1n_2)^{\alpha}m^{1-\alpha}\frac{1}{T}[(1-\alpha)e^{(1-\alpha)\frac{\Delta\mu}{T}}+\alpha e^{-\alpha\frac{\Delta\mu}{T}}]. \tag{9}$$

Equation (5) can then be used to express λ in terms of the probabilities w and v. Converting Eq. (2) to a stochastic equation then gives

$$I=wn_1n_2-vm+\xi, \tag{10}$$

where

$$\langle\xi(r_1,t_1)\xi(r_2,t_2)\rangle=2[(1-\alpha)wn_1n_2+\alpha vm]\times\delta(r_1-r_2)\,\delta(t_1-t_2).$$

The Langevin source of reaction (2) is thus determined not only by the probabilities w and v but also by another

parameter, the nonlinear dissipative coefficient α. If the system is in equilibrium, then $wn_1h_2=v_m$ is found and it can be seen from Eq. (10) that in this case the correlation function of the Langevin source does not depend on α.

It should be noted that in physical terms, the variation in the thermodynamic force $\delta(\Delta\mu)$ is caused not by local changes in the particle concentration but by external forces, i.e., by random redistribution of the molecular momenta. In order to find the fluctuations in the particle concentration, we need to substitute the stochastic expression for the reaction rate (10) into the conservation laws and seek their solution subject to various boundary conditions.

No constraints on the nonlinear dissipative coefficient α were obtained in Ref. 2 although it can be seen from Eq. (10) that if $\alpha>1$ or $\alpha<0$, the system may become unstable far from equilibrium.

Nonequilibrium fluctuations of the particle flux across a phase interface may be analyzed similarly.

[1] R. L. Stratonovich, *Nonlinear Nonequilibrium Thermodynamics* [in Russian], Moscow (1985).
[2] A. P. Grigin, Pis'ma Zh. Tekh. Fiz. **21**(19), 38 (1995) [Tech. Phys. Lett. **21**, 785 (1995)].
[3] L. D. Landau and E. M. Lifshits, Zh. Éksp. Teor. Fiz. **32**, 618 (1957) [Sov. Phys. JETP **5**, 512 (1957)].

Translated by R. M. Durham

Calculation of non-steady-state thermal conduction for low Fourier numbers (Fo<0.001)

V. S. Loginov, A. R. Dorokhov, and N. Yu. Repkina

Tomsk Polytechnic University
(Submitted October 25, 1996)
Pis'ma Zh. Tekh. Fiz. **23**, 22–25 (January 12, 1997)

Assuming that for small Fourier numbers heat transfer is determined by the specific heat of a heated layer of thickness $\delta=\sqrt{a\cdot\tau}$, an equation is derived for the temperature field, whose solution is satisfied in finite quadratures and has a fairly simple form. The results of calculations made using the proposed dependence are compared with the accurate solutions obtained by A. V. Lykov. This suggests that acceptable calculation accuracy may be achieved for Fo<0.001 and Bi<20. In this case the values of the dimensionless temperature do not depend on the shape of the body, and the proposed dependence can be used for calculations of plates, cylinders, or spheres. © *1997 American Institute of Physics.* [S1063-7850(97)00501-6]

Fast thermal processes are being increasingly widely used in various technologies and industrial systems. These include pulsed methods of treating thin films and promising designs of inkjet printers. The important factor here is that the characteristic times of the thermal process are 0.01–1 ms. Calculations of the heat transfer by thermal conduction for such short times are made by various methods.

These methods include first, numerical techniques and second, various analytical techniques (such as the Fourier method, the Laplace method, and so forth). In principle, each of these methods can achieve the required calculation accuracy but the only problem is the feasibility of implementing these methods and their accessibility to a wide range of engineering workers.

The range of small Fourier numbers (Fo<0.001) typical of fast thermal processes is extremely inconvenient for analytical techniques. In the Fourier method for example, there is a substantial increase in the number of terms in the series which must be calculated to achieve an acceptable degree of accuracy. In the Laplace method it is difficult to operate with an error function in practical calculations. It is therefore of some interest to find new methods and procedures for solving non-steady-state heat conduction problems for fast processes.

Here we consider an approximate method of calculation based on the following assumptions.

Experience of the diagnostics of the thermal regime of plasma jets[1] suggests that a procedure using so-called heat flux detectors is well justified. The simplest theory of this type of detector, known as a capacitive detector, is based on using the following relation for the heat flux

$$q=C\cdot\rho\cdot\delta\cdot\frac{\partial T}{\partial\tau}. \tag{1}$$

Here C and ρ are the specific heat and density of the detector material, and δ is the thickness of the sensing element of the detector.

Let us consider the fundamental heat conduction equation

$$\rho\cdot C\cdot\frac{\partial T}{\partial\tau}=\mathrm{div}(q). \tag{2}$$

The next step in the transformation of Eq. (2) usually involves assuming the Fourier hypothesis for the heat flux:

$$q=-\lambda\cdot\mathrm{grad}(T), \tag{3}$$

where λ is the thermal conductivity of the material.

Substituting Eq. (3) into Eq. (2), we obtain the well-known nonsteady-state heat conduction equation:

$$\frac{\partial T}{\partial\tau}=a\cdot\frac{\partial^2 T}{\partial x^2}. \tag{4}$$

Here $a=\lambda/(\rho\cdot C)$ is the thermal diffusivity of the body.

It may be supposed that for short times the expression (1) for the heat flux can be justifiably assumed in formula (2). We then have

$$\frac{\partial T}{\partial\tau}=\delta\frac{\partial}{\partial x}\left(\frac{\partial T}{\partial\tau}\right). \tag{5}$$

Introducing the notation $\Psi=\partial T/\partial\tau$, we obtain an ordinary differential equation for the function Ψ, whose solution has the form

$$\Psi(x,\delta)=C_1\cdot\exp\left(\frac{x}{\delta}\right). \tag{6}$$

Assuming $\delta=\sqrt{a\tau}$ in Eq. (6), then with Cauchy boundary conditions and the initial condition $T=T_0$ at $\tau=0$, we obtain

$$\theta(X,\mathrm{Fo})=\frac{\vartheta(x,\tau)}{\vartheta_0}=\frac{T(x,\tau)-T_{zh}}{T_0-T_{zh}}$$
$$=1-\frac{\exp[(X-1)/\sqrt{\mathrm{Fo}}]}{1+[1/(\mathrm{Bi}\sqrt{\mathrm{Fo}})]}. \tag{7}$$

Here the parameters are defined as: $\mathrm{Fo}=(a\tau/R^2)$ is the Fourier number, $\mathrm{Bi}=(aR/\lambda)$ is the Biot number, and $X=(x/R)$ is the dimensionless coordinate.

TABLE I. Comparison between calculations using formula (7) and the exact solutions.[2]

	Formula (7)	Data (Ref. 2)		
Bi	Fo = 0.0003	Plate	Cylinder	Sphere
0.1	0.998	0.999	0.999	0.999
0.5	0.991	0.996	0.991	0.991
1	0.983	0.980	0.987	0.981
4	0.935	0.927	0.925	0.926
10	0.852	0.833	0.830	0.831
20	0.743	0.705	0.701	0.703

In order to assess the applicability of this expression to calculate the temperature field for small Fourier numbers, the calculations using this expression were compared with the solution presented in Ref. 2.

The results of such a comparison for the Fourier number Fo=0.0003 and various Biot numbers are presented in Table I. It can be seen that there is a negligible difference between the calculations according to formula (7) and the accurate solution, although they are more cumbersome.

This solution is of practical use since it can give a direct estimate of the heat flux for small Fo. We obtain

$$q=-\lambda\frac{\partial\vartheta}{\partial x}=\sqrt{\frac{\lambda\rho C}{\tau}}\{\vartheta_0[-\theta(X,\mathrm{Fo})+1]\}. \tag{8}$$

It is readily established that solution (7) satisfies the limiting cases: for $\mathrm{Fo}\to 0$, $\theta(X,\mathrm{Fo})\to 1$ and for $\mathrm{Fo}\to\infty$, $\theta(X,\mathrm{Fo})\to 0$.

In Table I the results of calculations of the dimensionless temperature made using formula (7) are compared with the calculations made in Ref. 2 [p. 209, formula (40)]. It can be seen that as far as Biot numbers Bi=20 the calculations using the approximate formula (7) provide entirely satisfactory accuracy. This conclusion applies to all bodies of canonical form (plates, spheres, and cylinders).

Similar comparisons were made for other Fourier numbers. The upper limit of the range of validity of this formula may be taken as $\mathrm{Fo}\leqslant 0.001$.

On the basis of the agreement between the approximate and exact solutions for a specific range of Biot and Fourier numbers, we can draw some conclusions on the validity of the assumptions made to derive the initial equation whose solution yielded formula (7).

Two factors are clearly fundamental here—the specific expression for the heat flux in the form (1) and the determination of the expression for the scale δ. This reduces the order of the resulting differential equation. Similar transformations and assumption were made in Ref. 3 to calculate the heat flux but in this case the order of the differential equation was of third order in the temperature. For the range of dimensionless parameters determining the process of nonsteady-state heat exchange by heat conduction, the assumptions made can be considered to be entirely justified.

[1] Yu. V. Polezhaev and F. V. Yurevich, in *Heat Protection*, ed. by A. V. Lykov [in Russian], Énergiya, Moscow (1976).
[2] A. V. Lykov, *Theory of Heat Conduction* [in Russian], Vyssh. Shkola, Moscow (1967).
[3] N. M. Galin and L. P. Kirillov, *Heat and Mass Exchange (in Nuclear Power Engineering)* [in Russian], Énergoatomizdat, Moscow (1987).

Translated by R. M. Durham

Generation of vibrationally excited H_2 molecules in a hydrogen stream flowing through a cesium–hydrogen discharge

F. G. Baksht and V. G. Ivanov

A. F. Ioffe Physicotechnical Institute, Russian Academy of Sciences, St. Petersburg
(Submitted November 5, 1996)
Pis'ma Zh. Tekh. Fiz. **23**, 26–32 (January 12, 1997)

A theoretical analysis is made of the electronic–vibrational kinetics in a stream of molecular hydrogen flowing through a cesium–hydrogen discharge. An analysis is made of the vibrational pumping of hydrogen molecules in the discharge and vibrational relaxation is studied in the cold flow zone beyond the discharge. It is shown that a very substantial increase in the concentration of vibrationally excited H_2 molecules may be achieved in the old zone. © *1997 American Institute of Physics.* [S1063-7850(97)00601-0]

1. Methods of generating fairly highly vibrationally excited H_2 molecules are now attracting increased interest because of their plasma-chemical applications and the development of volume plasma sources of H^- ions.[1] It was shown in Refs. 2–5 that a low-voltage cesium–hydrogen discharge may be used for efficient generation of vibrationally excited H_2 molecules. In the present paper we report the first results of a theoretical analysis of the vibrational kinetics in a hydrogen stream flowing through this type of discharge plasma. It is shown that by selecting suitable discharge and flow conditions, a very substantial ($\sim 10^3$–10^4) increase in the concentration of excited molecules may be achieved in a particular part of the vibrational spectrum as compared with their concentration in a steady-state discharge.

2. The flow model studied is illustrated in Fig. 1a. A stream of hydrogen flows in a plane channel, passing successively through sections I and II. A low-voltage Cs–H_2 discharge is initiated in section I and the H_2 molecules undergo vibrational excitation, forming the initial vibrational distribution function $f_v(0)$ over the vibrational levels v. In the following section II the hydrogen stream flows between cold planes whose temperature T is close to room temperature.

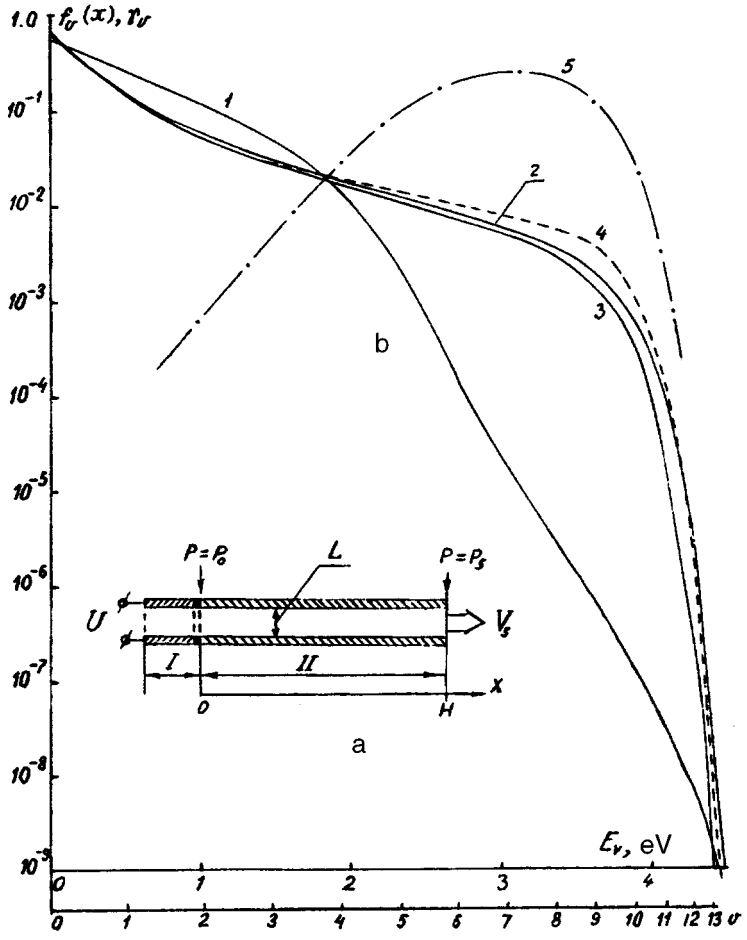

FIG. 1. a — Diagram showing hydrogen flow in channel: I — discharge zone and II — gas flow in cold channel; b — vibrational distribution function of H_2 molecules in section II: *1* — $f_v(0)$ [$N_{H_2}(0)=3\times10^{16}$ cm^{-3}], *2* — $f_v(x_m)$ [$x_m=4.12$ cm, $N_{H_2}(x_m)=1.94\times10^{16}$ cm^{-3}], *3* — $f_v(H)$ [$H=7$ cm, $N_{H_2}(H)=3.76\times10^{15}$ cm^{-3}], calculated with allowance for vibrational relaxation of molecules at the walls, *4* — $f_v(H)$ calculated same as curve *3* but neglecting vibrational relaxation at the walls, and *5* — probability of formation of an H^- ion by dissociative attachment of an electron to level v ($T_e=0.7$ eV).

Here the tail of the distribution becomes populated as a result of Treanor diffusion of quanta into the range of high v. At the edge of the channel ($x=H$) the vibrationally excited gas flows out at the velocity of sound V_s.

3. The vibrational distribution function of the molecules formed in the discharge, i.e., in section I, was determined by solving a system of rate equations[6] for the vibrational level populations N_v with allowance for $e-v$ exchange, $v-v$ and $v-t$ exchange, transitions between vibrational levels as a result of interaction between H_2 molecules and Cs atoms, dissociative attachment, associative detachment, and transitions between H_2 vibrational levels due to stripping of H^- ions. Vibrational deexcitation of H_2 molecules at the electrodes was also taken into account in the model.[2,5] For the upper vibrational levels in the model interaction between an H_2 molecule excited to level v and the wall results in the establishment of an approximately plateau-shaped distribution over levels v' between $v'=v$ and $v'=0$ after collision with the wall.[7] For the $v=1$ lower excited level the model[2,5] yields [in agreement with the experiment (Ref. 8, p. 38)] an extremely low probability $w_{10}=10^{-3}$. The plasma was assumed to be homogeneous over the gap. The plasma parameters were determined as a result of a self-consistent solution of the equations describing the particle and energy balance in the plasma and the electronic–vibrational kinetics.[5]

Figure 1b gives an example of the calculated distribution function $f_v(0)$ of H_2 molecules in the discharge, normalized to unity. The initial discharge parameters were: hydrogen concentration $N_{H_2}^{(0)}=3\times10^{16}$ cm^{-3}, total cesium density $N_{Cs}^{(0)}=10^{14}$ cm^{-3}, interelectrode gap $L=0.3$ cm, cathode emission current $j_s=10$ A/cm^2, and discharge voltage $U=6.9$ V. The calculated electron temperature and density are: $T_e=0.7$ eV and $n_e=6.4\times10^{13}$ cm^{-3}.

4. The molecular distribution function established gas flow in section II was determined assuming a decrease in the molecular density N_{H_2} as a result of a drop in the gas pressure over the length of the channel. The fundamental relations determining the flow of hydrogen in section II may be obtained by assuming, as in Ref. 9, Poiseuille flow for a compressible gas in a long ($H\gg L$) channel between two parallel planes and approximating the average velocity over the cross section (Ref. 10, p. 81) at the edge of the channel ($x=H$) to the velocity of sound V_s. This yields the following relation between the channel length H and the pressure p_s at the channel edge, i.e., at the gas outflow point:

$$H/L=(R_s/24)(c_p/c_v)^{-1}[(p_0/p_s)^2-1]. \tag{1}$$

Here p_0 is the hydrogen pressure at $x=0$, i.e., approximately the pressure in the discharge, $R_s=\rho_s L V_s/\eta$ is the Reynolds number calculated for the velocity of sound V_s and the channel width L, η is the viscosity of hydrogen (Ref. 11, p. 365), and $\rho_s=M_{H_2}p_s/kT$ is the gas density at $x=H$.

The pressure distribution $p(x)$ over the channel length in section II is given by

$$p(x)=[p_0^2-(p_0^2-p_s^2)\cdot x/H]^{1/2}. \tag{2}$$

In the calculations the channel length H was varied to obtain the highest population $N_{v*}(H)$ at the channel edge for any level v^* is the upper part of the spectrum. In our example this level is $v^*=10$. Note that the distribution $N_v(x)$ of the level populations over length in the upper part of the spectrum is nonmonotonic so that the maximum population is achieved at a certain point $x=x_m<H$ (Fig. 2).

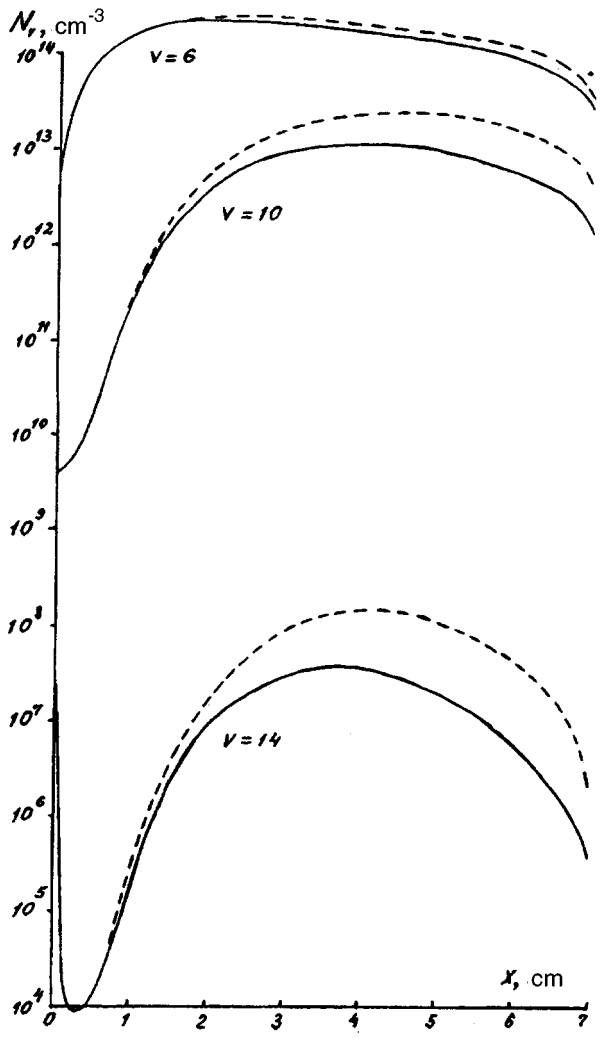

FIG. 2. Absolute populations of vibrational levels of H_2 molecules as a function of channel length in section II. Solid curves — calculated with allowance for vibrational relaxation at the walls. Dashed curves — neglecting vibrational relaxation at the walls.

The vibrational distribution function of the H_2 molecules in section II was determined by solving the following system of equations:

$$\frac{d(N_v\cdot V)}{dx}=I_v^{vv}\{N_v\}+I_{vM}^{vt}\{N_v\}+\frac{1}{\tau}\left[\sum_{v'>v}N_{v'}w_{v'v}-N_v\sum_{v'<v}w_{vv'}\right] \tag{3}$$

$(v,v'=0,1,2,\ldots,14)$,

where $V(x)=V_s p_s/p(x)$ is the gas flow rate in the channel averaged over the cross section.

The terms on the right-hand side of Eq. (3) describe $v-v$ and $v-t$ exchange with H_2 molecules and vibrational

relaxation of H_2 molecules at the walls: $\tau \approx I^2/D_{sd}$ is the average drift time for H_2 molecules between the electrodes, D_{sd} is the coefficient of self-diffusion of the H_2 molecules (Ref. 11, p. 375), and $w_{vv'}$ is the probability of vibrational deexcitation at the walls. The populations $N_v(0)$ in the discharge are used as the initial conditions for Eq. (3). It is assumed that Cs freezes out at the cold walls and does not influence the vibrational relaxation of H_2 in section II.

5. The results of the calculations are plotted in Figs. 1b and 2. Figure 1b gives the functions $f_v(H)$ in the stream flowing out of the channel and $f_v(x_m)$ corresponding to maximum excitation of the $v^*=10$ level inside the channel, normalized to unity. The dashed curves give the distribution function at the edge ($x=H$) calculated neglecting vibrational deexcitation of H_2 molecules at the channel walls. Figure 2 gives the absolute populations $N_v(x)$ of various vibrational levels in the upper part of the spectrum. The solid and dashed curves, respectively in Fig. 2 were calculated with and without allowance for vibrational deexcitation of H_2 molecules at the walls. It can be seen from Fig. 1b that drift in the channel is accompanied by a very substantial increase in the populations of vibrationally excited states in a certain part of the vibrational spectrum ($v=8-11$). To a considerable extent, this applies to those vibrational levels whose vibrational excitation is important for the generation of H^- ions by dissociative attachment. This is illustrated in Fig. 1b, which gives $\gamma_v(T_e)=K_v(T_e)\cdot f_v(H)/\Sigma_v K_v(T_e)\cdot f_v(H)$, this being the probability of the formation of an H^- ion by attachment of an electron to an H_2 molecule excited to level v, normalized to unity.[12] Since the vibrational relaxation time is increased substantially when molecules are injected into a large chamber, this method of producing vibrational distribution functions of H_2 molecules may be promising for two-chamber sources of H^- ions. In these sources the vibrational excitation of H_2 molecules and generation of H^- ions by dissociative attachment of electrons to vibrationally excited molecules are spatially separated.

This work was supported by a grant from INTAS (Grant No. 94-316 and by a grant from the International Science Foundation and the Russian Government (Grant No. NTZ000).

[1] M. Bacal and D. A. Skinner, Comments At. Mol. Phys. **23**, 283 (1990).
[2] F. G. Baksht and V. G. Ivanov, Zh. Tekh. Fiz. **62**(2), 195 (1992) [Sov. Phys. Tech. Phys. **37**, 223 [1992)].
[3] F. G. Baksht, G. A. Dyuzhev, L. I. Elizarov, V. G. Ivanov, A. G. Nikitin, and S. M. Shkol'nik, Pis'ma Zh. Tekh. Fiz. **19**(22), 39 (1993) [Tech. Phys. Lett. **19**, 716 (1993].
[4] F. G. Baksht, V. G. Ivanov, A. G. Nikitin, and S. M. Shkol'nik, Pis'ma Zh. Tekh. Fiz. **20**(22), 83 (1994) [Tech. Phys. Lett. **20**, 927 (1994)].
[5] F. G. Baksht, G. A. Djuzhev, L. L. Elizarov, V. G. Ivanov, A. A. Kostin, and S. M. Shkol'nĭk, Plasma Sources Sci. Technol. **3**, 88 (1994).
[6] F. G. Baksht and V. G. Ivanov, Zh. Tekh. Fiz. **66**(9), 58 (1996) [Tech. Phys. **41**, 890 (1996)].
[7] J. R. Hiskes and A. M. Karo, J. Appl. Phys. **56**, 1927 (1984).
[8] *Nonequilibrium Vibrational Kinetics*, ed. by M. Capitelli (Springer-Verlag, Berlin, 1986) [Russ. transl., Mir, Moscow, 1989].
[9] S. Dushman and J. M. Lafferty, *Scientific Foundations of Vacuum Technique*, 2nd ed., ed. by J. M. Lafferty (Wiley, New York, 1976) [Russ. transl., Mir, Moscow, 1986].
[10] L. D. Landau and E. M. Lifshitz, *Fluid Mechanics*, 2nd ed. (Pergamon Press, Oxford, 1987) [Russ. original, 3rd ed., Nauka, Moscow (1986].
[11] *Physical Quantities*, edited by I. S. Grigor'ev and E. Z. Meĭlikhov [in Russian], Energoizdat, Moscow (1991)
[12] J. M. Wadehra, Phys. Rev. A **29**, 106 (1984)

Translated by R. M. Durham

Lasing in submonolayer CdSe structures in a ZnSe matrix without external optical confinement

I. L. Krestnikov, N. N. Ledentsov, M. V. Maksimov, A. V. Sakharov, S. V. Ivanov, S. V. Sorokin, L. N. Tenishev, P. S. Kop'ev, and Zh. I. Alferov

A. F. Ioffe Physicotechnical Institute, Russian Academy of Sciences, St. Petersburg
(Submitted November 12, 1996)
Pis'ma Zh. Tekh. Fiz. **23**, 33–38 (January 12, 1997)

It is shown that in order to achieve lasing in structures with CdSe submonolayers inserted in a ZnSe matrix, no additional optical confinement of the active region using thick wide-gap layers is required. The high oscillator strength of the excitons trapped at CdSe islands modulates the permittivity and thus produces a natural exciton-induced waveguiding effect. © *1997 American Institute of Physics.* [S1063-7850(97)00701-5]

It has recently been shown that by using tunnel-coupled vertically self-organized quantum dots in the active region of a III–V double-heterostructure heterolaser, lasing can be achieved via the exciton ground state in quantum dots up to room temperature.[1] In this case however, the actual design of the laser waveguide[2] was the same as before, i.e., the active region with the quantum dots was confined by thick wide-gap layers of lower refractive index.

In many cases, it is difficult to fabricate thick wide-gap layers either because there is no suitable heteropair (for the silicon matrix) or because of the difficulties of doping a wide-gap compound (for *p*-ZnMgSSe, *p*-GaN layers). In the present paper we shall show that at least in structures with CdSe quantum islands in a ZnSe matrix, there is no strict need for additional optical confinement, since a waveguiding effect may be produced by an increase in the refractive index in the exciton resonance range. Lasing even occurs if the average CdSe content in the quantum island region is only 4%.

The deposition of submonolayer coatings in III–V compounds results in the formation of ordered arrays of two-dimensional monolayer-high islands with good size uniformity.[3–5] Submonolayer insertions in wide-gap matrices have been studied in detail for InAs–GaAs systems, where it has been demonstrated that the exciton transitions have an ultrahigh oscillator strength,[6] the momentum selection rules are lifted,[7] and the exciton binding energy is enhanced.[8] In this system however, the total exciton localization energy relative to states in the barrier is only between a few meV and ~20 meV, which is insufficient for most instrumental applications at room temperature. On the other hand the high carrier effective masses in wide-gap II–VI compounds and group-three nitrides, which are responsible for the small Bohr radius of the exciton, give rise to an appreciable exciton localization energy at the islands, making these structures highly promising for applications in optoelectronics.

We have investigated a structure whose active region had no additional optical confinement by thick wide-gap layers with a significantly lower refractive index. A short-period superlattice of twenty periods, consisting of submonolayer CdSe insertions with an average thickness of 0.4 monolayer, separated by 28 Å ZnSe barriers, was grown on a GaAs(100) substrate by molecular beam epitaxy.[9] The superlattice was separated from the substrate and the surface by 1.5 μm- and 500 Å-thick ZnSSe layers whose lattices were matched with GaAs. Thin layers of ZnMgSSe ~100 Å thick located at a

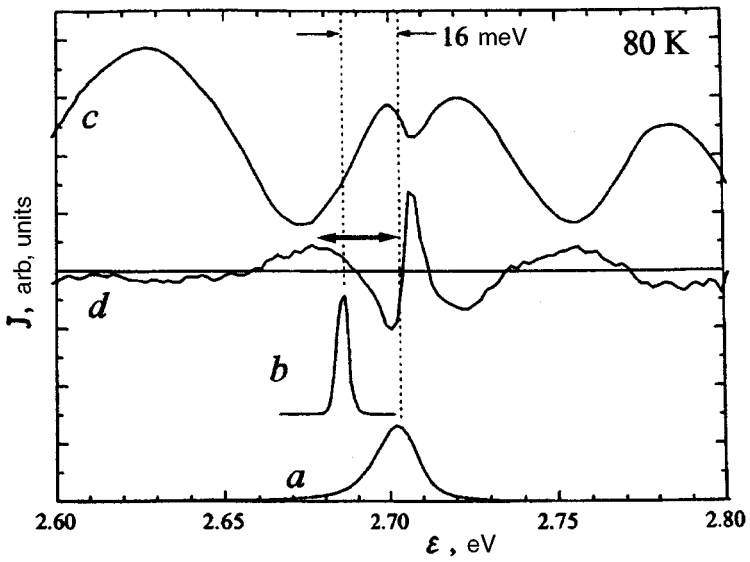

FIG. 1. Surface photoluminescence spectra at a pump power density of 1 W/cm^2 (a), lasing from the end for pump power 50 kW/cm^2 (b), optical reflection (c), and its second energy derivative (d). (The arrow indicates the range of the exciton-induced waveguiding effect).

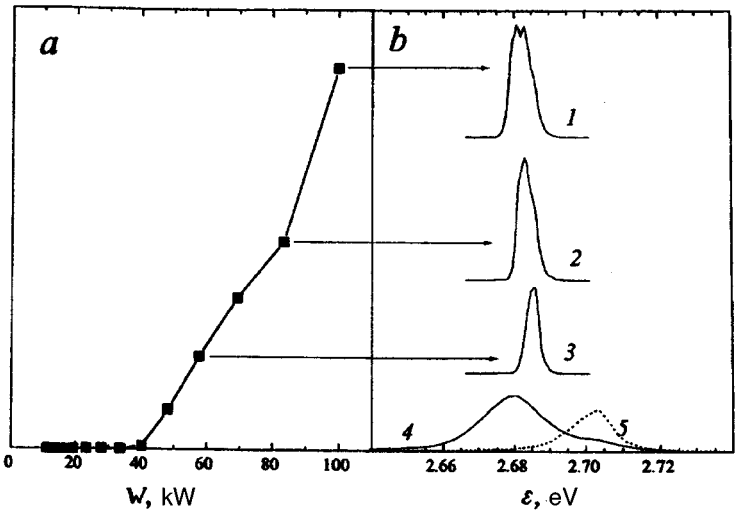

FIG. 2. Integrated laser radiation intensity versus pump power density (a). Lasing spectra obtained at various pump power densities (b): 100 kW/cm^2 (*1*), 83 kW/cm^2 (*2*), 58 kW/cm^2 (*3*), and 28 kW/cm^2 (*4*), and surface photoluminescence spectra at a pump power density of 1 W/cm^2 (*5*).

distance of 500 Å on both sides of the superlattice were used for electronic confinement of the carriers in the superlattice region.

The structures with submonolayer CdSe coatings in a ZnSe matrix were investigated by high-resolution transmission electron microscopy.[10] It was shown that the submonolayer coating forms itself into an array of quantum islands with average dimensions of ~4 nm in the lateral plane and ~1.2 ML in the direction of growth. Under repeated deposition cycles the islands are mainly formed one on top of the other, similar to the quantum dots in an InAs–GaAs system.[11]

The photoluminescence, reflection, and lasing spectra of this structure are shown in Fig. 1. It can be seen that the reflection spectrum exhibits a conspicuous feature caused by the high oscillator strength of the excitons bound at quantum islands. The range of appreciable modulation of the refractive index extends by 25 meV in both the long-wavelength and short-wavelength directions, which can be identified particularly clearly on the graph of the second derivative of the energy reflection coefficient. It was shown in Ref. 12 that an increase in the refractive index occurs in the energy range near the exciton resonance on the long-wavelength side, which induces a waveguide effect. It can be seen from Fig. 1 that the lasing line is only shifted by 16 meV in the long-wavelength direction from the exciton resonance energy, i.e., lasing takes place directly in the range of exciton modulation of the refractive index.

It was shown in Ref. 13 that the feasibility of lasing via exciton states arises from the lifting of the momentum selection rules caused by the spatial localization of the exciton and the reduced symmetry of the system. In ZnCdSe/ZnSe quantum-well structures the lasing wavelength is usually shifted by 30–60 meV in the long-wavelength direction due to the exciton–phonon amplification mechanism in free-exciton structures,[14] since a ''hot'' exciton with a large wave vector cannot undergo radiative recombination.[15] It was also demonstrated in Ref. 13 that lasing may be achieved in a structure with CdSe/ZnSSe submonolayers. In this case however, the active region was confined by thick wide-gap layers of significantly lower refractive index, which made it difficult to estimate the actual exciton waveguiding efficiency. The structure studied here has no thick wide-gap layers and lasing is achieved as a result of the exciton-induced waveguiding effect.

Figure 2 gives lasing spectra for various pump power densities and the integrated luminescence intensity is also plotted as a function of pump power density. It can be seen that above 40 kW/cm^2, the photoluminescence line narrows abruptly to 3 meV and a sharp increase is observed in the differential efficiency of the radiation, suggesting a transition to lasing. As the pump power density is increased to 100 kW/cm^2, the lasing line is broadened to 7 meV as a result of multimode lasing and at 100 kW/cm^2 the lasing line is a superposition of two lines with half-widths of 2.5 and 4 meV.

CONCLUSIONS

We have demonstrated that in semiconductor structures with CdSe/ZnSe quantum islands, lasing may be achieved as a result of the formation of an exciton waveguide without any thick wide-gap emitters having a reduced refractive index compared with the active region. In addition, the spatial localization of the excitons in these islands lifts the momentum selection rules.

This work was supported by Grant No. INTAS-94-481 and by a Grant from the Russian Fund for Fundamental Research, No. 95-02-04056.

[1] N. N. Ledentsov, M. Grundmann, N. Kirstaedter, O. Schmidt, R. Heitz, J. Bzhrer, D. Bimberg, V. M. Ustinov, V. A. Shchukin, P. S. Kop'ev, Zh. I. Alferov, S. S. Ruvimov, A. O. Kosogov, P. Werner, U. Richter, U. Gzsele, and J. Heydenreich, Solid State. Electron. **40**, 785 (1996).

[2] Zh. I. Alferov, N. A. Bert, A. Yu. Egorov, A. E. Zhukov, P. S. Kop'ev, A. O. Kosogov, I. L. Krestnikov, N. N. Lebentsov, A. V. Lunev, M. V. Maksimov, A. V. Skharov, V. M. Ustinov, A. F. Tsatsul'nikov, Yu. M. Shernyakov, and D. Bimberg, Fiz. Tekh. Poluprovodn. **30**, 351 (1996) [Semiconductors **30**, 194 (1996)].

[3] V. I. Marchenko, Zh. Éksp. Teor. Fiz. **81**, 1141 (1981) [Sov. Phys. JETP **54**, 605 (1981)].

[4] P. D. Wang, N. N. Ledentsov, C. M. Sotomayor Torres, P. S. Kop'ev, and V. M. Ustinov, Appl. Phys. Lett. **64**, 1526 (1994).

[5] V. Bressler-Hill, A. Lorke, S. Varma, P. M. Petrov, K. Pond, and W. H. Weinberg, Phys. Rev. B **50**, 8479 (1994).
[6] M. V. Belousov, N. N. Ledentsov, M. V. Maksimov, P. D. Wang, I. N. Yassievich, N. N. Faleev, I. A. Kozin, V. M. Ustinov, P. S. Kop'ev, and C. M. Sotomayor Torres, Phys. Rev. B **51**, 14346 (1995).
[7] A. A. Sirenko, T. Ruf, N. N. Ledentsov, A. Yu. Egorov, P. S. Kop'ev, V. M. Ustinov, and A. E. Zhukov, Solid State Commun. **97**, 169 (1996).
[8] P. D. Wang, N. N. Ledentsov, C. M. Sotomayor Torres, I. N. Yassievich, A. Pakhomov, A. Yu. Egorov, P. S. Kop'ev, and V. M. Ustinov, Phys. Rev. B **50** (1994).
[9] S. V. Ivanov, S. V. Sorokin, P. S. Kop'ev, J. R. Kim, H. D. Jung, and H. S. Park, J. Cryst. Growth **159**, 16 (1996).
[10] D. Gerthsen and A. Rosenauer, to be published.
[11] L. Goldstein, F. Glas, J. Y. Marzin, M. N. Charasse, and G. LeRoux, Appl. Phys. Lett. **47**, 1099 (1985).
[12] Zh. I. Alferov, S. V. Ivanov, P. S. Kop'ev, A. V. Lebedev, N. N. Ledentsov, M. V. Maximov, I. V. Sedova, T. V. Shubina, and A. A. Toropov, Superlat. Microstruct. **15**(2) (1994).
[13] N. N. Ledentsov, I. L. Krestnikov, M. V. Maximov, S. V. Ivanov, S. V. Sorokin, P. S. Kop'ev, Zh. I. Alferov, D. Bimberg, and C. M. Sotomayor Torres, Appl. Phys. Lett. **69**, 1343 (1996).
[14] Y. Kawakami, I. Hauksson, H. Stewart, J. Simpson, I. Galbraith, K. A. Prior, and B. C. Cavenett, Phys. Rev. B **48**, 11994 (1993).
[15] S. A. Permogorov, Phys. Status Solidi B **68**, 9 (1975).

Translated by R. M. Durham

Self-consistent model of a low-pressure rf capacitive discharge

A. S. Smirnov and K. E. Orlov

St. Petersburg State Technical University
(Submitted November 5, 1996)
Pis'ma Zh. Tekh. Fiz. **23**, 39–45 (January 12, 1997)

A simple self-consistent model of a low-pressure rf capacitive discharge is formulated. Effects associated with stochastic heating of the electrons and the nonlocal nature of the electric field are taken into account. The relations obtained can be used for a qualitative analysis of the main features of these low-pressure discharges. The results of the numerical calculations show good agreement with available experimental data. © *1997 American Institute of Physics.* [S1063-7850(97)00801-X]

Radio-frequency capacitive discharges are widely used in plasma technologies for semiconductor materials.[1] In many respects, the quality and efficiency of the plasma treatment processes depend on the parameters of the plasma and the electrode sheaths of the discharge. This has been responsible for the sustained interest in the development of simple methods of calculating the characteristics of rf discharges over a wide range of external parameters (pressure and composition of working gas, dimensions of chamber and electrodes, power input to discharge, and so forth). In most cases of practical importance, low-pressure discharges are used, where $p \cdot L_0 = 0.1-0.001$ cm·Torr (where p is the pressure in the discharge chamber and L_0 is the length of the interelectrode gap). Under these conditions, the electron energy relaxation length may exceed the characteristic dimensions of the system, the electron distribution function becomes nonlocal, and the energy spectrum is determined by the distribution of the oscillatory conduction field over the total length of the discharge gap. Rare-gas discharges are the simplest to analyze theoretically. Even in this case however, it is not possible to obtain an accurate analytic solution. In principle, all the plasma parameters of an rf capacitive discharge can be obtained by the now commonly used numerical simulation based on the Monte Carlo method and its modifications, but these procedures require a large amount of computer time. In addition, it is generally difficult to construct physical scaling laws based on these calculations because of the difficulties involved in identifying the role of the various physical mechanisms responsible for the processes in the plasma. A method of calculating the electron distribution functions proposed in Ref. 2, based on averaging the transport equation over the range of electron motion, also requires fairly complex numerical calculations. The simple model proposed in Ref. 3 is not closed since the electron temperature in the plasma must be defined using experimental data. In the present paper we propose a simple self-consistent model of a discharge which can be used to calculate its main parameters.

The condition $\omega_i \ll \omega \ll \omega_e$ (where ω_i and ω_e are the ion and electron plasma frequencies, respectively, and ω is the frequency of the rf field) is ordinarily satisfied in rf discharges. In this case, the ions form a steady-state density profile while the electrons oscillate between one electrode and the other at a frequency equal to the rf field frequency, as shown in Fig. 1a. If the Debye length is much shorter than the length of the electrode sheath, the moving plasma–space charge sheath boundary is abrupt and forms a potential barrier of infinite height for the electrons. In the central part of the discharge gap, where the quasineutrality condition is satisfied over the entire period, the ion profile is formed by ambipolar diffusion. In the electrode sheaths drift of ions to the electrodes is governed by the average space charge field over a period. To simplify the following analysis, we shall assume that the densities in the sheath and in the plasma are constant and are respectively n_s and n_p. We shall also approximate the potential drop from the plasma to the sheath by a step profile with a jump at the boundary with the space charge sheath. Corresponding distributions of the ion density and potential are plotted in Figs. 1b and 1c. Subject to these assumptions, the ion flux from the plasma may be estimated as

$$\Gamma_p = n_p \cdot \sqrt{\frac{2\phi}{L_p}\frac{e\lambda_i\sqrt{2}}{M}}, \tag{1}$$

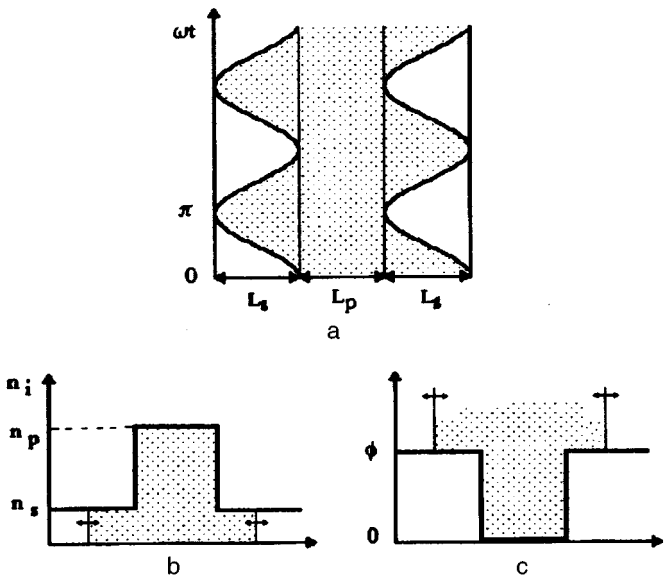

FIG. 1. Position of plasma–space charge sheath boundary as a function of rf voltage phase (a); distribution of ion density (b) and potential (c) in interelectrode gap.

where λ_i and M are the ion mean free path and mass, e is the electron charge, ϕ is the constant plasma potential at the boundary with the sheath, and L_p is the plasma length. Since no ionization takes place in the sheaths, the ion flux in the sheath remains constant and Γ_p is equal to the ion flux to the electrodes;

$$\Gamma_s = n_s \sqrt{\frac{4\pi j_0}{\omega}\frac{e\lambda_i\sqrt{2}}{M}}, \tag{2}$$

where j_0 is the peak discharge current density. The density ratio n_s/n_p may be obtained from Eqs. (1) and (2), where the density n_s is determined by the condition for closure of the discharge current by the displacement current in the sheath in the space charge phase:[3]

$$n_s = \frac{2j_0}{\omega e L_s}, \tag{3}$$

where L_s is the length of the space charge sheath. In the plasma phase the discharge current is transported by the conduction current, and the amplitude of the oscillatory field in the plasma phase is related to the density by the condition of discharge current continuity

$$j_0 = e\cdot b_e\cdot n_p\cdot E_p = e\cdot b_e\cdot n_s\cdot E_s, \tag{4}$$

where $E_{p,s}$ is the amplitude of the conduction field in the plasma and the sheath, and b_e is the electron mobility.

We shall make a qualitative analysis of the processes shaping the electron distribution in the plasma in order to determine the discharge parameters. Heating of electrons with energies $\varepsilon > e\phi$ is determined by the spatially averaged oscillatory field. For a simple ''two-stage'' model of the plasma density distribution between the electrodes, trivial averaging is performed and the energy flux for the high-energy part of the distribution function is given by

$$\Gamma_{\varepsilon,H} = \left[\frac{L_p}{L_0}E_p^2 + \frac{L_s}{L_0}E_s^2\right]\frac{e^2\nu\varepsilon^{3/2}}{6m^2(\omega^2+\nu^2)}\frac{\partial f_H}{\partial\varepsilon} = D_{\varepsilon,H}\frac{\partial f_H}{\partial\varepsilon}, \tag{5}$$

where m is the electron mass, ν is the transport frequency of the electron collisions, and ε is the electron energy. Electrons with energies $\varepsilon < e\phi$ do not enter the sheath and the field for the low-energy part of the distribution function is equal to the oscillatory field in the plasma. The energy flux for the low-energy part of the distribution is therefore

$$\Gamma_{\varepsilon,C} = E_p^2\,\frac{e^2\nu\varepsilon^{3/2}}{6m^2(\omega^2+\nu^2)}\frac{\partial f_C}{\partial\varepsilon} = D_{\varepsilon,C}\frac{\partial f_C}{\partial\varepsilon}. \tag{6}$$

Assuming that f_C has no singularities for $\varepsilon\to 0$ and $e\phi < \varepsilon^*$, where ε^* is the energy of the first excitation level of the gas atoms, we introduce the following approximate normalization conditions for the functions f_C and f_H:

$$n_p = \frac{4\pi}{3} f_C^0 (e\phi)^{3/2}, \tag{7}$$

$$n_s = \frac{4\pi}{3} f_H^0 (e^{*3/2} - e\phi^{3/2}). \tag{8}$$

These conditions hold for $n_p \gg n_s$. We shall assume that as a result of inelastic collisions with atoms, electrons lose all their kinetic energy and return to the low-energy part of the distribution with $\varepsilon = 0$. Then when $0 < \varepsilon < \varepsilon^*$, the flux Γ_ε is conserved and $\Gamma_{\varepsilon,C} = \Gamma_{\varepsilon,H} = \text{const}(\varepsilon)$. Equating Eqs. (5) and (6) with allowance for Eqs. (7) and (8) we obtain

$$\left(\frac{\varepsilon^*}{\varepsilon_\phi}\right)^{3/2} - 1 = \frac{n_s}{n_p}\left(1 + \left[\frac{L_p}{L_0} + \frac{L_s}{L_0}\frac{E_s^2}{E_p^2}\right]\right). \tag{9}$$

The Townsend formula for a static field can be used to calculate the ionization frequency.[4] Then the number of ionizations in the plasma volume is:

$$Z = n_s\cdot E_{\text{eff}}\cdot b_e\cdot A\cdot p\cdot\exp\left(-\frac{Bp}{E_{\text{eff}}}\right) \tag{10}$$

where

$$E_{\text{eff}}^2 = \frac{1}{2}\left[\frac{L_p}{L_0}E_p^2 + \frac{L_s}{L_0}E_s^2\right]\frac{\nu^2}{(\omega^2+\nu^2)} \quad \text{(from Ref. 5)},$$

p is the gas pressure, and A and B are empirical constants. The charged particle losses from the plasma volume may be expressed in terms of the ion flux in the space charge sheath (2). Equating Γ_s/L_p and Z, we obtain an equation for the charged particle balance in the plasma volume. By solving

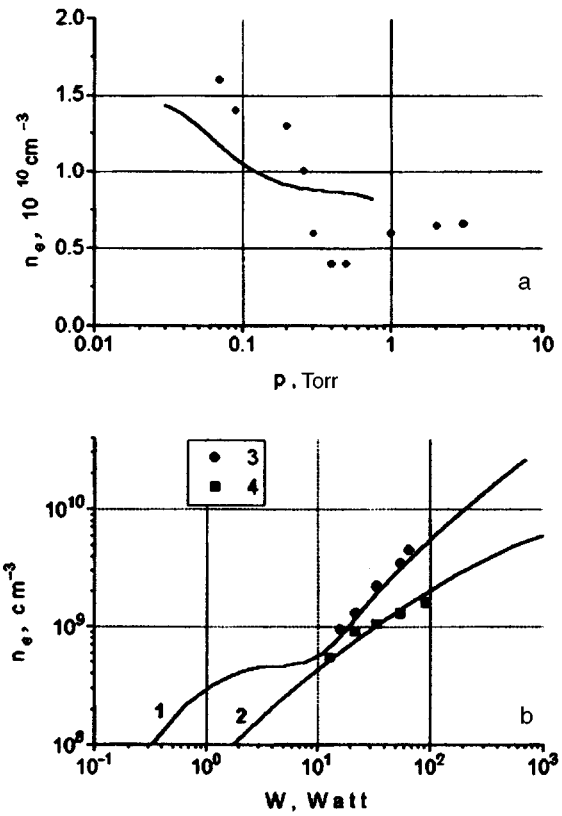

FIG. 2. a — Electron density (n_e) at center of discharge gap versus pressure (p) for argon; $L_0 = 2$ cm, and $j_0 = 2.67$ mA/cm^2. Solid curve — calculations, points — experimental values.[6] b — Average electron density (n_e) in plasma versus power (W) deposited in discharge for argon, $L_0 = 4$ cm; *1, 3* — $p = 0.11$ Torr, *2, 4* — $p = 0.02$ Torr, *1, 2* — calculations, and *3, 4* — experimental values.[7]

Eqs. (9) and (10) simultaneously, we can determine $L_s(j_0)$ and $\phi(j_0)$. Then all the plasma parameters can be calculated using these values of L_s and ϕ (Ref. 3).

At low pressures (when $\lambda_e \geqslant L_s$, where λ_e is the electron mean free path), stochastic heating of the electrons becomes an important factor.[2] This effect can be approximately taken into account by incorporating the additional term $\frac{3}{2}(\Omega_B/\nu)E_s^2$ in Eq. (5), where $\Omega_B = \sqrt{2\varepsilon/m}/L_p$ is the frequency of electron collisions with moving plasma–sheath boundaries.

Figure 2a gives the density n_p in the plasma as a function of pressure for an argon discharge ($j_0 = 2.67$ mA/cm^2, $L_0 = 2$ cm) calculated using Eqs. (9) and (10). The results of the calculations agree with the experimental data[6] within measurement error and reflect the qualitative dependence obtained from Eqs. (1)–(3):

$$n_p(p) \propto \frac{1}{L_s}\sqrt{\frac{L_p}{|\phi|}} \propto \sqrt{\frac{1}{|\phi|}}\,. \tag{11}$$

In a highly asymmetric discharge, where the influence of a small sheath can be disregarded, L_s should be replaced by $L_s/2$ in the formula for the averaged electric field (5). The results of calculations for an asymmetric argon discharge ($L_0 = 4$ cm, $p = 0.02$ and 0.11 Torr) are plotted in Fig. 2b. The power deposited in the discharge is calculated as the sum of the powers deposited in the electron and ion components. It can be seen that the experimental results[7] agree with the calculations over a wide range of input powers.

Despite the simplifications, the proposed model correctly takes into account the main characteristics of a low-pressure rf capacitive discharge. The results of the numerical calculations yield accurate qualitative relationships and reasonable quantitative agreement with the available experimental data.

This work was supported by the Russian Fund for Fundamental Research (Grant No. 96-02-16918), the International Atomic Energy Agency (Grant No. 9238), and INTAS (Grant No. 94-0740).

[1] *Plasma Processing for VLSI*, ed. by N. G. Einspruch and D. M. Brown, Vol. 8 of VLSI Electronics (Academic Press, New York, 1984) [Russ transl. Mir, Moscow, 1987].
[2] I. D. Kaganovic and L. D. Tsendin, IEEE Trans. Plasma Sci. **20**(7), 86 (1992).
[3] A. E. Dul'kin, S. A. Moshkalev, A. S. Smirnov *et al.*, Zh. Tekh. Fiz. **63**(7), 64 (1993) [Tech. Phys. **38**, 564 (1993)].
[4] Yu. P. Raĭzer, *Physics of Gas Discharges* [in Russian], Nauka, Moscow (1992).
[5] V. E. Golant, A. P. Zhilinskiĭ, and S. A. Sakharov, *Principles of Plasma Physics* [in Russian], Atomizdat, Moscow (1997).
[6] V. A. Godyak and R. B. Piejak, Phys. Rev. Lett. **65**, 996 (1990).
[7] A. S. Smirnov, A. Yu. Ustavchikov, and K. S. Frolov, Prib. Tekh. Éksp. No. 3, 129 (1994).

Translated by R. M. Durham

Simultaneous recording and readout of $\chi^{(2)}$-holograms in glasses

A. I. Valeev and V. M. Churikov

University Academic Department of Nonlinear Optics, Institute of Electrophysics, Urals Branch of the Russian Academy of Sciences and Chelyabinsk State Technical University
(Submitted June 5, 1996)
Pis'ma Zh. Tekh. Fiz. **23**, 46–51 (January 12, 1997)

A new method for readout of $\chi^{(2)}$-holograms recorded by noncollinearly polarized light beams of different frequencies is proposed and implemented. The hologram is read out and recorded simultaneously by the same reference beam, thus eliminating any influence of the readout radiation on the recorded hologram. © *1997 American Institute of Physics.* [S1063-7850(97)00901-4]

In 1986 Österberg and Margulis[1] first observed efficient second harmonic generation in a germanosilicate fiber. After high-power neodymium laser radiation has propagated for a long time in the fiber (the so-called preparation process), the fiber begins to convert the infrared radiation to the second harmonic. This discovery was unexpected, since the quadratic susceptibility in glass is zero and the phase-matching condition is not satisfied. Stolen and Tom[2] showed that the preparation process may be speeded up considerably by coupling both the infrared radiation and its second harmonic simultaneously into the fiber. It was shown in Refs. 2 and 3 that mutually coherent optical fields at frequencies ω and 2ω write a quadratic susceptibility grating ($\chi^{(2)}$-hologram) in a fiber. The authors of Ref. 4 recorded $\chi^{(2)}$-holograms in bulk glasses. Experiments to study the tensor properties of $\chi^{(2)}$-gratings indicated that a spatially periodic electrostatic field with a period satisfying the phase-matching condition for second harmonic generation is produced in the fiber[5,6] or in bulk glass.[7,8] However, these experiments did not identify the mechanism responsible for produced this field. It was also shown[9] that this mechanism may differ for different glasses. Additional information on the mechanism for recording of $\chi^{(2)}$-holograms could be provided by experiments to study the dynamics of recording for various ratios between the intensities of the ω and 2ω beams. However, such investigations encounter serious problems because recording must be terminated to measure the signal level reconstructed by the hologram and this is accompanied by periodic erasure of the recorded hologram by the readout radiation,[4] which distorts the results. These distortions will obviously be greater, the more points we try to measure.

In the present paper we propose a new method for readout of $\chi^{(2)}$-holograms which, in our view, can avoid these difficulties. The method essentially involves simultaneously recording the hologram and reading the signal from the hologram by the same reference beam. Since the frequency and direction of propagation of the signal and the external second harmonic are the same, these waves can only be separated if their polarizations differ. Thus at the exit from the sample, the external second harmonic may be quenched by the analyzer. In that case the fraction of the signal intensity proportional to $\sin^2\theta$, where θ is the angle between the polarizations of the external second harmonic and the signal, passes through the analyzer and may be recorded by the photodetector. It was shown in Ref. 7 that the polarizations of the external and readout second harmonic differ if the $\chi^{(2)}$-hologram is recorded by linearly polarized ω and 2ω waves for which the angle between the polarizations is neither zero nor 90°. Interference between an external second harmonic and a signal whose intensity was equalized by an exit analyzer was observed in Ref. 10. The results of these studies suggested that the proposed method could be implemented experimentally.

The apparatus is shown schematically in Fig. 1. The radiation source was a Q-switched actively mode-locked Nd:YAG laser. The pulse length was 100 ps, each train contained 30 pulses, and the repetition frequency of the trains was 7 kHz. The average infrared radiation power in the glass was ~400 mW and the second harmonic power was approximately 0.1 mW. The holograms were recorded using ZhS-4 glass from the GOST 9411-81 set of light filters. The laser radiation was partially converted to the second harmonic in a KTP crystal and was then passed through a polarizing system, after which the ω and 2ω waves were linearly polarized

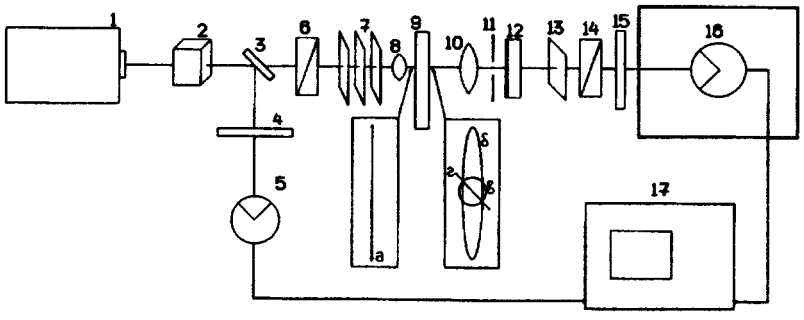

FIG. 1. Diagram of apparatus: *1* — laser, *2* — KTP crystal, *3* — plane plate, *4*, *15* — SZS-23 filter, *5* — FD-24 photodiode, *6* — input polarizer, *7* — polarizing system consisting of three mica plates, *8*, *10* — lenses, *9* — glass sample, *11* — diaphragm, *12* — infrared mirror, *13* — birefringent plate, *14* — analyzer, *16* — photomultiplier, and *17* — oscilloscope.

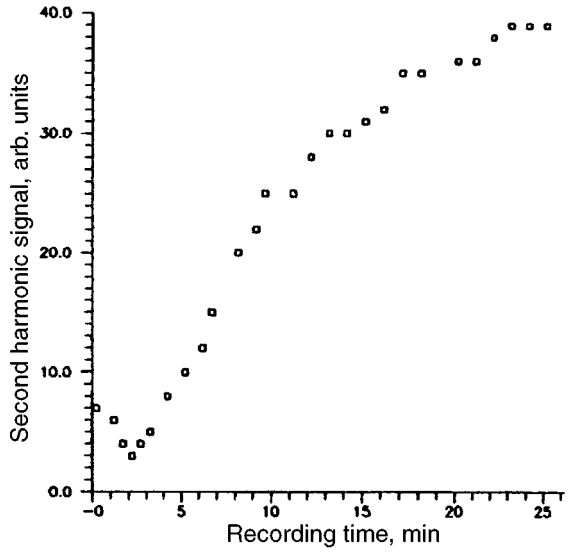

FIG. 2. Intensity of second harmonic after propagating through analyzer versus hologram recording time.

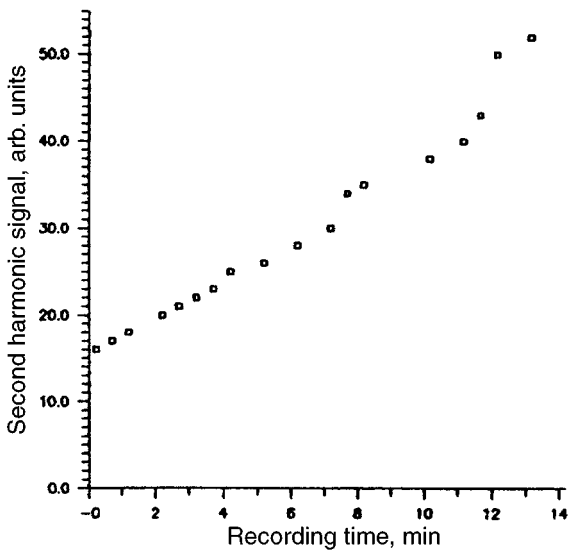

FIG. 3. Time dependence of second harmonic intensity when the polarization ellipticity of the external second harmonic is compensated by a birefringent plate.

at an angle of 45° to each other. A calibrated FD-24 photodiode was used to measure the radiation intensity. The radiation was focused into the ZhS-4 glass sample by means of a microscope objective having a focal length of 5 mm. An exit analyzer (Glan prism) was used to separate the second harmonic signal reconstructed by the recorded hologram. The signal was recorded with an FEU-127V photomultiplier. The analyzer almost completely quenched the external second harmonic in the absence of the ZhS-4 glass. When the glass was present, total quenching was not achieved for two reasons. First, induced birefringence (the optical Kerr effect) occurs in the field of the ω high-power light wave in the glass so that the 2ω external linearly polarized radiation (Fig. 1a) was elliptically polarized at the exit from the glass. Second, the light underwent depolarization in the glass as a result of scattering. Thus, in addition to the reconstructed signal (Fig. 1d), depolarized radiation (Fig. 1c) and radiation corresponding to the minor axis of the ellipse (Fig. 1b) also propagated through the analyzer. The signal read out from the hologram is obviously summed differently with the depolarized and Kerr components of the parasitic signal. In the first case, the intensities are simply summed whereas in the second case, it is the amplitudes that are summed, but in antiphase, since the phases of the waves corresponding to the major and minor axes of the ellipse differ by $\pi/2$ and the phase of the wave corresponding to the major axis of the ellipse, i.e., the external second harmonic, differs by $\pi/2$ from the phase of the second harmonic signal read out from the hologram.[10] This factor explains the drop in the total second harmonic intensity at the beginning of recording. When the amplitude of the signal from the hologram was equal to the amplitude corresponding to the minor axis of the ellipse, these signals canceled each other and the photodetector only recorded the depolarized component of the radiation. To check out this statement, we ''linearized'' the Kerr ellipse using a birefringent plate at the beginning of recording. In this case, the intensity recorded by the photodetector was reduced to the level observed at the minimum of the curve in Fig. 2. This indicates that the influence of the Kerr effect may be eliminated and the parasitic signal will be determined only by the depolarized component. Figure 3 gives the time dependence of the intensity of the second harmonic propagating through the analyzer during recording. The polarization ellipticity induced by the Kerr effect was eliminated by using a birefringent plate. Thus, if the signal from the hologram is not too strong compared with the parasitic signal, the Kerr effect must first be eliminated and then, when analyzing the results, the intensity corresponding to the depolarized radiation must be subtracted. If the signal is fairly strong, these effects can be neglected.

It has therefore been demonstrated that a $\chi^{(2)}$-hologram can be read out and recorded simultaneously by the same reference beam, without separating these two processes in time. The proposed method can be used to study the growth dynamics and for continuous monitoring of the power of recorded $\chi^{(2)}$-holograms, and also to record short-lived quadratic polarizability gratings.

This work was supported by the Russian Fund for Fundamental Research (Grant No. 96-02-16059-a). The authors would like to thank B. Ya. Zel'dovich and Yu. V. Miklyaev for useful discussions of this problem.

[1] U. Österberg and W. Margulis, Opt. Lett. **11**, 516 (1986).
[2] R. H. Stolen and H. W. Tom, Opt. Lett. **12**, 585 (1987).
[3] N. B. Baranova and B. Ya. Zel'dovich, JETP Lett. **45**, 717 (1987).
[4] B. Ya. Zel'dovich, Yu. E. Kapitskiĭ, and V. M. Churikov, JETP Lett. **53**, 78 (1991).
[5] V. Mizrahi, Y. Hibino, and G. Stegeman, Opt. Commun. **78**, 283 (1990).
[6] F. Ouellette, K. O. Hill, and D. C. Johnson, Opt. Lett. **13**, 515 (1988).
[7] M. A. Bolshtyansky, V. M. Churikov, Yu. E. Kapitzky, A. Yu.

Savchenko, and B. Ya. Zel'dovich, Pure Appl. Opt. **1**, 289 (1992).
[8] V. M. Churikov, Yu. E. Kapitzky, V. N. Lukyanov, and B. Ya. Zel'dovich, Sov. Lightwave Commun. **1**, 389 (1991).
[9] E. M. Dianov, P. G. Kazansky, D. S. Starodubov, and D. Yu. Stepanov, Sov. Lightwave Commun. **2**, 83 (1992).
[10] M. A. Bolshtyansky, V. M. Churikov, Yu. E. Kapitzky, A. Yu. Savchenko, and B. Ya. Zel'dovich, Opt. Lett. **18**, 1217 (1993).

Translated by R. M. Durham

Luminescence of erbium-doped porous silicon

V. P. Bondarenko, N. N. Vorozov, L. N. Dolgiĭ, A. M. Dorofeev, N. M. Kazyuchits, A. A. Leshok, and G. N. Troyanova

Belarus State University of Information Science and Radio Electronics, Minsk
(Submitted August 15, 1996)
Pis'ma Zh. Tekh. Fiz. **22**, 84–87 (December 26, 1996)

[S1063-7850(96)03912-2]

Doping of silicon with erbium is a promising direction in optoelectronics, since Si:Er structures emit light with a wavelength of 1.54 μm, which corresponds to a minimum of losses and dispersion in quartz optical fibers.[1] The formation of a surface layer of porous silicon makes it possible to simplify substantially the doping of silicon with erbium. It was previously established that erbium-doped porous silicon with a porosity of 60–80% luminesces in the visible region of the spectrum and efficiently emits light with wavelength 1.54 μm.[2–5] However, highly porous structures have a low mechanical strength, high resistivity, and unstable physicochemical properties.[6]

In the present Letter, it is demonstrated for the first time that intense 1.54-μm luminescence can be obtained in layers of dense porous silicon formed with a different structure on silicon single crystals with n-type and p-type conduction.

The initial samples consisted of p and n^+ silicon single crystals doped with boron and antimony up to 8×10^{16} and 4×10^{18} cm^{-3}, respectively. Layers of porous silicon with thickness 1–20 μm were formed by anodization in 12–48% HF with a current density of 2–40 mA/cm^2. Cathodic deposition of erbium was conducted from an alcohol solution of $Er(NO_3)_3 5H_2O$ with a current density of 125 μA/cm^2 in a period of 30 min. Next, the samples were subjected to heat treatment at 800–1200 °C in air, by means of halogen lamps, for 30 s or in a diffusion furnace for 2–10 min. Control samples of single-crystalline silicon with electrochemically deposited erbium were fabricated in the same conditions. The luminescence was excited with an Ar laser ($\lambda_{exc}=488$ nm). The emission spectra were recorded at 77 and 300 K with an MDR-23 grating monochromator with a liquid-nitrogen-cooled Ge:Cu photodetector.

Two wide bands with maxima at 1.3 and 0.85 μm were recorded in the luminescence spectrum of p-type porous silicon. There was no luminescence in the n^+-type porous silicon samples. Electrochemical deposition of erbium had virtually no effect on the luminescence spectrum of porous silicon.

After high-temperature (800–1200 °C) annealing, an additional narrow luminescence peak with wavelength 1.54 μm characteristic for erbium was recorded on all erbium-doped porous silicon samples. There was no such luminescence in the control samples without the porous silicon, but with electrochemically deposited Er. The intensity of the 1.54-μm luminescence of porous silicon layers on n^+ silicon was much lower than that of porous silicon on p-silicon. This difference could be due to the different structures of the p- and n^+-type porous materials[7] and/or the presence of radiation with wavelength less than 1.54 μm, giving rise to additional excitation of erbium, in the spectrum of p-type porous silicon.

The intensity of the radiation associated with the optically active Er depended on the heat-treatment temperature. For p-type porous silicon an increase in the annealing temperature up to 1000 °C was accompanied by an increase in the intensity of the 1.54-μm peak (Fig. 1). This is apparently associated with an increase in the degree of oxidation of the surface of pores and, correspondingly, with an increase in the degree of optical activation of the erbium ions, a necessary condition for which is the formation of complexes of an Er^{+3} ion with six oxygen atoms.[8] A further increase of the temperature resulted in weaker erbium luminescence (Fig. 1). This could be due to the dissociation of ''erbium–oxygen'' impurity complexes and/or the formation of crystallographic defects, which increase the probability of nonradiative recombination, in the silicon core of the porous layer.[1] For a more dense n^+-type porous material a higher temperature (up to 1200 °C) and 5–10 min anneal were required for 1.54-μm luminescence to appear.

Increasing the thickness of the porous silicon layer under the same erbium deposition conditions resulted in stronger 1.54-μm luminescence (Fig. 2). With constant deposition times and constant cathode current density the amount of erbium introduced should be the same. Therefore an increase in the 1.54-μm radiation intensity indicates that the fraction of optically active Er increases with increasing thickness of the porous silicon layer. This confirms indirectly that the

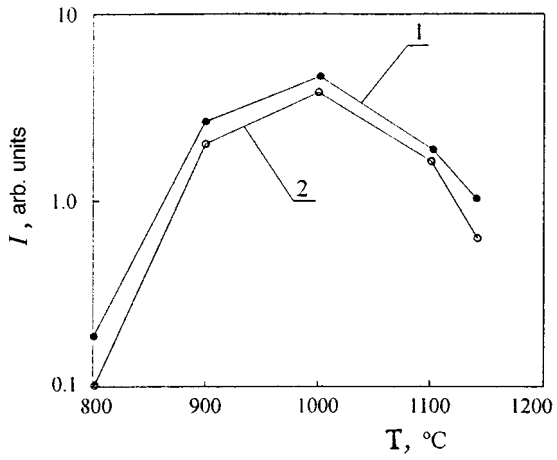

FIG. 1. Intensity of the 1.54-μm photoluminescence of erbium-doped p-type porous silicon versus the erbium activation temperature. The porous silicon layer is 5 μm thick. Measurement temperatures: *1*—77 K; *2*—300 K.

 1063-7850/97/010003-02$10.00

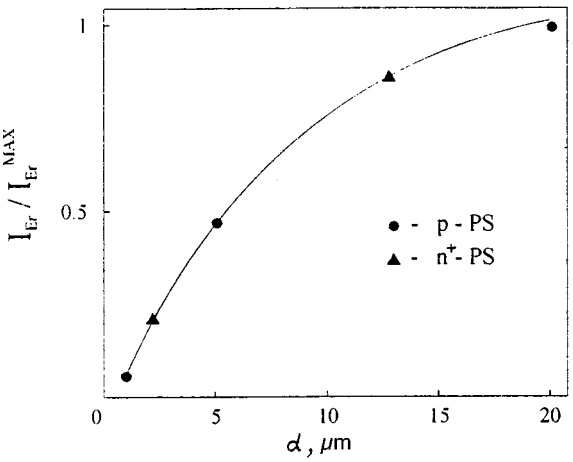

FIG. 2. Intensity of 1.54-μm photoluminescence versus the thickness d of the erbium-doped p-type porous silicon layer. Optical activation of erbium with halogen lamps: temperature — 1000 °C; duration — 30 s, medium — air.

deposition of metal occurs predominantly on the walls of the pores and not on the surface of the sample.

It should be especially noted that the intensity of the Er peak remained practically unchanged when the measurement temperature was increased from 77 K up to room temperature. This contrasts with erbium-doped single-crystal silicon for which the 1.54-μm luminescence intensity characteristically drops sharply by several orders of magnitude.[1] A comparative analysis[2] of different erbium-doped semiconductors showed that as the band gap of the semiconductor increases from 0.807 eV (for GaInAsP) up to 2.42 eV (for CdS), the thermal quenching of the Er radiation decreases. The experimentally observed (Fig. 1) weak temperature dependence of the 1.54-μm radiation intensity could indicate that the Er^{+3} ion is located in material with a larger bandgap than in the initial silicon single crystal. This material could be silicon nanocrystals, whose band structure is modifed by the quantum size effect, or an amorphous layer on their surface.

In summary, the experimental results obtained show that the low-porosity materials, sponge-type material on p-type silicon and dendritic porous silicon based on n^+-type silicon can be used for light-emitting structures. The latter material is widely employed for gettering of defects, formation of insulating regions and ''silicon on insulator'' structures, and as a buffer layer in homo- and heteroepitaxial structures.[9] Doping of such a material with erbium makes it possible to expand the range of device structures. Specifically, the introduction of erbium into integrated optical waveguides based on porous silicon[10] can be used for devices for filtering, amplification, and generation of optical signals.

[1] N. A. Sobolev, Fiz. Tekh. Poluprovodn. **29**, 1153 (1995) [Semiconductors **29**, 595 (1995)].
[2] F. Namavar, F. Lu, C. H. Perry *et al.*, MRS Symp. Proc. **358**, 375 (1995).
[3] J. H. Shin, G. N. Hoven, and A. Polman, Appl. Phys. Lett. **66**, 2379 (1995).
[4] T. Kimura, A. Yokoi, H. Horiguchi *et al.*, Appl. Phys. Lett. **65**, 983 (1994).
[5] A. M. Dorofeev, N. V. Gaponenko, V. P. Bondarenko *et al.*, J. Appl. Phys. **77**, 2679 (1995).
[6] A. Bsiesy, J. C. Vial, F. Gaspard *et al.*, Surf. Sci. **254**, 195 (1991).
[7] R. L. Smith and S. D. Collins, J. Appl. Phys. **71**, R1 (1992).
[8] D. L. Adler, D. C. Jacobson, and D. J. Eaglesham, Appl. Phys. Lett. **61**, 2181 (1992).
[9] V. P. Bondarenko, V. E. Brisenko, L. N. Glanenko, and V. A. Raĭko, Zarubezhnaya élektronnaya tekhnika, No. 9, 55 (1989).
[10] V. P. Bondarenko, A. M. Dorofeev, N. M. Kazyuchits *et al.*, Pis'ma Zh. Tekh. Fiz. **19**(14), 73 (1993) [Tech. Phys. Lett. **19**, 463 (1993)].

Translated by M. E. Alferieff

Wall effects in improved confinement modes in the FT-2 tokamak

V. N. Budnikov, V. V. D'yachenko, L. A. Esipov, E. R. Its, S. I. Lashkul, A. D. Lebedev, A. Yu. Stepanov, I. E. Sakharov, V. Yu. Shorikov, S. V. Shatalin, E. O. Chechik, and O. N. Shcherbinin

A. F. Ioffe Physicotechnical Institute, Russian Academy of Sciences, St. Petersburg
(Submitted November 10, 1996)
Pis'ma Zh. Tekh. Fiz. **23**, 52–57 (January 12, 1997)

An analysis is made of the transition to improved confinement (H-mode) observed in lower hybrid heating experiments in the FT-2 tokamak. Particular attention is paid to processes taking place near the wall, including the suppression of microfluctuations accompanying the L–H transition and the buildup of edge-localized modes (ELM activity). The conditions for transition to the H-mode are discussed only for Ohmic heating. The data are compared with the results of large tokamak experiments. © *1997 American Institute of Physics.*
[S1063-7850(97)01001-X]

A transition to improved energy and particle confinement in the FT-2 tokamak ($a=8$ cm, $R=55$ cm, $B_t=2.2$ T, and $I_p=22-40$ kA) has been observed in lower hybrid heating experiments ($P_{\mathrm{RF}}\leqslant 150$ kW, $f=920$ MHz) after the end of the rf pulse: an abrupt decrease in the emission on the H_β line was observed with an increase in the average density and the diamagnetic signal. It was also observed that MHD oscillations were suppressed and the plasma loop voltage U_p decreased slightly. The energy lifetime, which is ~ 0.8 ms for Ohmic heating, was doubled or trebled after the end of the rf pulse and was comparable with estimates obtained using the Kaye–Goldstone scaling and DIIID-JET scaling.[1] From the effects observed, this regime could be identified as the H-mode. In the present paper we report new experimental data on the transition to improved confinement.

It has been established that the anomalously high heat and particle transport in a tokamak and its reduction in the H-mode are caused by plasma microfluctuations and their suppression. In this study plasma oscillations in the frequency range $f<500$ kHz were investigated by enhanced scattering diagnostics and reflectometry.[2] The plasma was probed on the strong magnetic field side by an extraordinary wave at frequencies of 53–78 GHz. Depending on the frequency, the wave was either backscattered outside the toroidal plasma in its upper hybrid resonance (amplified scattering) or in the cutoff region on the inside (reflectometry). It was observed that during the rf pulse the plasma oscillations are reduced by $\sim 50\%$ and maximum suppression is achieved at the edge of the discharge at the radius $r=\pm 7$ cm. In addition, as a result of the L–H transition the level of oscillations on the inside of the torus was also lower after the end of the rf pulse. It was difficult to estimate the change in the energy lifetime in the plasma during the additional heating because of the neglected rf power losses in the grill region. Nevertheless, the increase in the particle lifetime and the suppression of the fluctuations suggested that the transport losses are reduced in the course of lower hybrid heating. The actual transition to improved confinement is masked by an additional flux of neutral hydrogen from the walls caused by bombardment of the surface with epithermal high-energy particles. In cases where the additional influx of neutral hydrogen from the wall was small, as for example in experiments with a large plasma current $I_{pl}=40$ kA and $P_{\mathrm{LH}}=100$ kW, characteristic decay of the H_β emission was observed during the rf pulse.

It was noted in Ref. 1 that on transition to the H-mode,

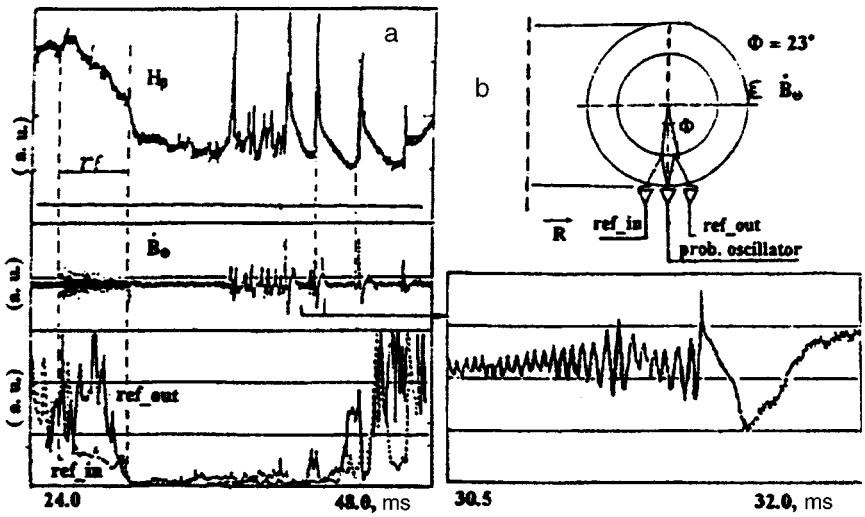

FIG. 1. a—Oscilloscope traces of H_β emission, magnetic probe signal $\dot{B}_\Theta$, and reflectometer signal on transition to the H-mode. The H_β spikes are associated with ELM instability. The magnetic precursor indicated by the arrow is given on an enlarged scale. The dotted curve gives the reflectometer signal from the inner antenna — (ref_in); (ref_out) — signal from outer antenna; b—arrangement of the reflectometer antennas.

the oscilloscope traces of the H_β emission sometimes revealed sharp peaks attributable to edge-localized modes known as ELMs. Additional information on the nature of these effects was also obtained during recent experiments on the FT-2 tokamak. Figure 1a shows oscilloscope traces of the magnetic probe signals and reflectometer signals integrated over the frequency band between 10 and 500 kHz, where ELM activity was observed in the H-mode. It was observed that before the ELM spikes the magnetic probes record characteristic coherent oscillations. The frequencies of these magnetic precursor oscillations were in the range $\nu_{\text{prec}} \approx$ (24–32) kHz. A cross correlation analysis of the magnetic probe signals revealed a high-m poloidal mode in this case, probably $m \sim 9$, developing on the $q = 4.5$ resonant magnetic surface. The configuration of the reflectometer antennae is shown schematically in Fig. 1b. In these measurements the plasma was probed at a frequency of 27 GHz. Power was coupled in as an ordinary wave via an antenna located below the toroidal chamber. Two other neighboring antennae (ref_in) and (ref_out), positioned in this poloidal cross section were used to detect the signal reflected from the inner and outer regions of the toroidal plasma filament, respectively. Information on the plasma oscillations was contained in the amplitude modulation of the reflected radiation. On transition to the H-mode, the reflectometer, as did the magnetic probes, recorded the suppression of microfluctuations. This was accompanied by reduced turbulence throughout the spectral range $f < 500$ kHz. In addition, each ELM spike was preceded by the buildup of coherent oscillations at frequencies corresponding to the mode determined by the magnetic probes and these oscillations were synchronized with the magnetic precursor. The oscillations were localized at the edge of the discharge on the weak magnetic field side at the radius $r = 6$ cm, where $q = 4$. It can be seen from Fig. 1a that they are mainly observed on the signal from the outer antenna (ref_out). The results of our measurements can be compared with large tokamak experiments to explain these phenomena. For example, under conditions of transition to the H-mode and the buildup ELM-instabilities, the appearance of a characteristic magnetic precursor was attributed to the evolution of resistive ballooning modes at the discharge edge. These ELM-instabilities were classified as type-III ELMs as opposed to the types-I and II ELMs whose peak was considered mainly in terms of the buildup of ideal ballooning modes.[3]

It has been established that a transition takes place from the L- to the H-mode when the thermal flux across the plasma separatrix reaches a certain threshold value P_{thr} (Ref. 4). For example, using the scaling obtained for the ASDEX tokamak $P_{\text{thr}} = 0.04 \times n_e \times S \cdot B_t$ [MW, $\text{m}^{-3} \cdot 10^{20}$, m^{-2}, T], for $\overline{n_e} = 3 \times 10^{19}$ m^{-3} the threshold value for the FT-2 tokamak is $P_{\text{thr}} = 55$ kW. At the same time, on the basis of the experimental data for Ohmic heating, the heat flux across the last closed flux surface (LCFS) of the discharge allowing for radiative losses P_{rad} and losses due to changes in the internal energy, dW/dt, was estimated as $P_{\text{LCFS}} = P_{\text{OH}} - P_{\text{rad}} - dW/dt = (30\text{–}40)$ kW. It therefore follows that $P_{\text{thr}} > P_{\text{LCFS}}$ and the L–H transition would thus require an additional input of energy which was provided by the lower hybrid heating. It may be postulated that the improved confinement initiated under lower hybrid heating was only sustained after the end of this heating by virtue of a hysteresis effect, i.e., on account of the condition $P_{\text{thr}}^{\text{L-H}} > P_{\text{thr}}^{\text{H-L}}$ This has already been observed in large tokamaks.[4] The threshold power for the reverse H–L transition is lower, evidently because of broadening of the current channel profile and reduced hydrogen recycling at the discharge edge.[1]

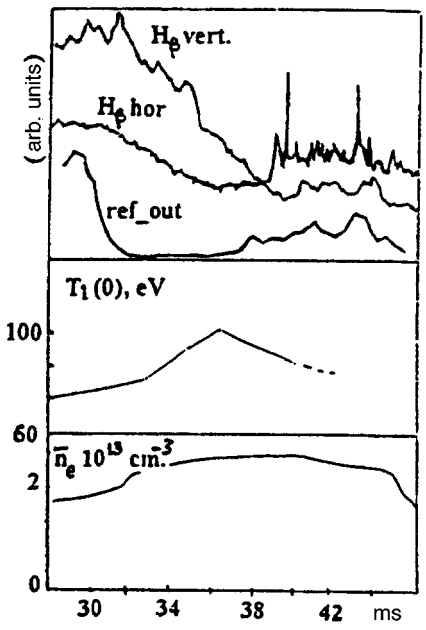

FIG. 2. Experimental data for the Ohmic L–H transition: H_β^{vert} and H_β^{hor} are the spectral signals along two mutually perpendicular chords, vertical and horizontal, respectively; (ref_out), $T_i(0)$, and $\overline{n_e}$ are the reflectometer signal from the outer antenna, the central ion temperature, and the average density, respectively.

The transition to improved confinement in recent experiments on the FT-2 tokamak was achieved under conditions of purely Ohmic heating. For this purpose the plasma was pressed toward the outside of the toroidal chamber by means of control fields in the third millisecond of the discharge. This controlled displacement (within 0.5 cm) caused a characteristic drop in the H_β emission as shown in Fig. 2 for two mutually perpendicular central chords. This was accompanied by suppression of microfluctuations and by an increase in the average density and ion temperature $T_i(0)$ of the plasma. In this case, the condition $P_{\text{LCFS}} \geqslant P_{\text{thr}}^{\text{L-H}}$ was satisfied by a reduction in P_{rad}. Measurements in the shadow of the limiter using a Langmuir probe showed that an appreciable increase in the density n_{eL} from $(1-1.5) \times 10^{12}$ cm^{-3} to 3×10^{-12} cm^{-3} and in the temperature T_{eL} from 5 to 10 eV may be observed as a result of this displacement on the outside of the toroidal plasma in the shadow of the limiter at the radius $r = 8.5$ cm (as compared with the inside). It may be noted that in this case a plasma state free from ELM instabilities in the H-mode is sustained for a longer time. Several mechanisms are considered in the literature as possible reasons for the suppression of plasma turbulence at the discharge edge, particularly increased shear of the plasma rotation. A reduction in the frictional forces caused by a decrease

in the neutral hydrogen concentration may also play a decisive role.[5]

These experimental investigations therefore indicate that the parameters of the wall plasma play an important part in influencing the conditions for the L–H transition. It has been observed that when the microfluctuations are suppressed, their changes exhibit poloidal asymmetry. A particularly important role in the transition to improved confinement is played by the conditions established on the outside of the toroidal plasma on the strong magnetic field side, where the greatest reduction in plasma fluctuations and H_β emission is observed as a result of the L–H transition. In this respect the results of our measurements agree with the conclusions obtained on other larger tokamaks.[6]

This work was supported by the Russian Fund for Fundamental Research, Project No. 95-02-04072.

[1] V. N. Budnikov *et al.*, JETP Lett. **59**, 685 (1994).
[2] V. N. Budnikov *et al.*, Fiz. Plazmy **21**, 865 (1995) [Plasma Phys. Rep. **21**, 817 (1995)].
[3] H. Zohm *et al.*, Nucl. Fusion **32**, 481 (1992).
[4] H. Zohm *et al.*, Plasma Phys. Contr. Nucl. Fusion **37**, 437 (1995).
[5] T. S. Hahm and K. N. Burrell, Phys. Plasma **2**, 1648 (1995).
[6] T. L. Rhode *et al.*, Nucl. Fusion **33**, 1787 (1993).

Translated by R. M. Durham

Influence of surface wettability on the cathodic electroluminescence of porous silicon

D. N. Goryachev, O. M. Sreseli, and L. V. Belyakov

A. F. Ioffe Physicotechnical Institute, Russian Academy of Sciences, St. Petersburg
(Submitted November 12, 1996)
Pis'ma Zh. Tekh. Fiz. **23**, 58–63 (January 12, 1997)

It is shown that the wettability of porous silicon influences the efficiency of its cathodic electroluminescence in electrolytes. A model is proposed to explain the nature of the electroluminescence in a system consisting of porous silicon and an oxidizing electrolyte.
 [S1063-7850(97)01101-4]

It has been established that the electroluminescence efficiency of porous silicon is highest in systems consisting of porous silicon and an electrolyte, especially when the silicon is used as the cathode.[1,2] In this case however, the luminescence quantum yield does not exceed 10^{-2} and the stability of the systems is poor. Investigations of the processes taking place at the interphase boundary with the electrolyte are therefore urgently required. The pore sizes are small (<10 nm) (Ref. 3) and their surface is strongly hydrophobic.[4] These factors fundamentally influence the nature of the luminescence. It was shown in Ref. 5 for the case of anodic luminescence that preliminary (before immersion in the electrolyte) wetting of the surface of porous silicon with ethanol appreciably enhances the emission. In the present paper we study the influence of the wettability of silicon on its cathodic electroluminescence in the visible range and we put forward some new ideas on the mechanism of current flow in this system.

Layers of porous silicon were prepared by anodic etching of n-Si(100) samples with a resistivity of 2 $\Omega\cdot$cm in an electrolyte containing 48% hydrofluoric acid and ethanol in the ratio 1:1 by volume, under intense illumination by white light. The anodic current density was 10–20 mA/cm^2 and the total charge was 5–12 C/cm^2. An Ohmic contact had been deposited previously on the back of the substrates.

Electroluminescence was observed in an electrolytic cell containing an oxidizing but nonetching potassium persulfate (0.1N $K_2S_2O_8$ + 1N H_2SO_4) electrolyte when the sample was connected as the cathode.[1] The solvent was a mixture of water and acetone. It is known that the surface of porous silicon is lyophilic to organic compounds.[4] It could thus be expected that these mixtures would efficiently wet the surface and enhance the electrical contact. A linearly increasing voltage was applied to the cell at a sweep rate of 80 mV/s and the polarization curve was recorded, i.e., the density of the current (j) flowing through the cell as a function of the cathode potential (φ) measured relative to a saturated calomel electrode, and the time for the onset of luminescence was identified. The quality of the contact between the electrolyte and the porous silicon layer was assessed from the cathode resistivity, which was determined by a graphical method by linearizing the polarization curves plotted in semilogarithmic coordinates $\log j(\varphi)$. Preliminary experiments have shown that for a smooth silicon surface the resistivity does not exceed 1 $\Omega\cdot$cm^2.

Figure 1 gives the resistivity of a porous silicon cathode as a function of the acetone content in the electrolyte. It can be seen that the addition of up to 50% acetone to the electrolyte reduces the cathode resistivity more than twenty times, i.e., to values typical of a smooth silicon substrate. These results indicate that this electrolyte almost completely impregnates the porous silicon layer and provides electrical

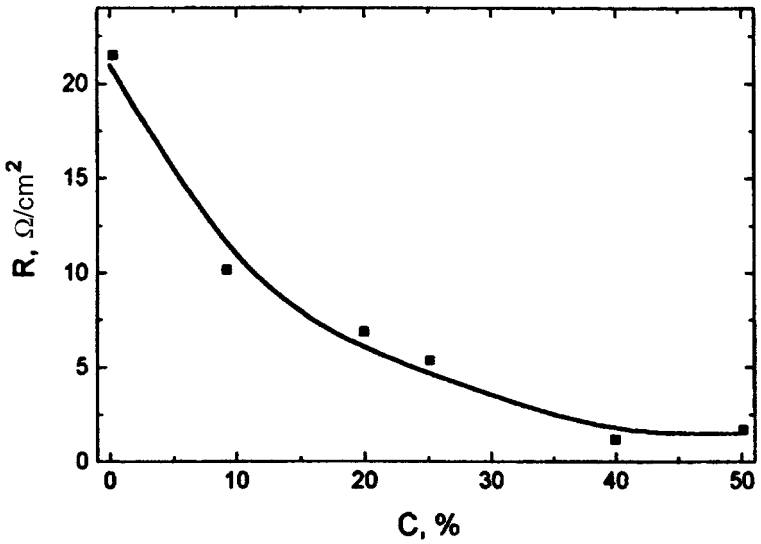

FIG. 1. Cathode resistivity R versus acetone concentration C in electrolyte. Wetting time 20 min.

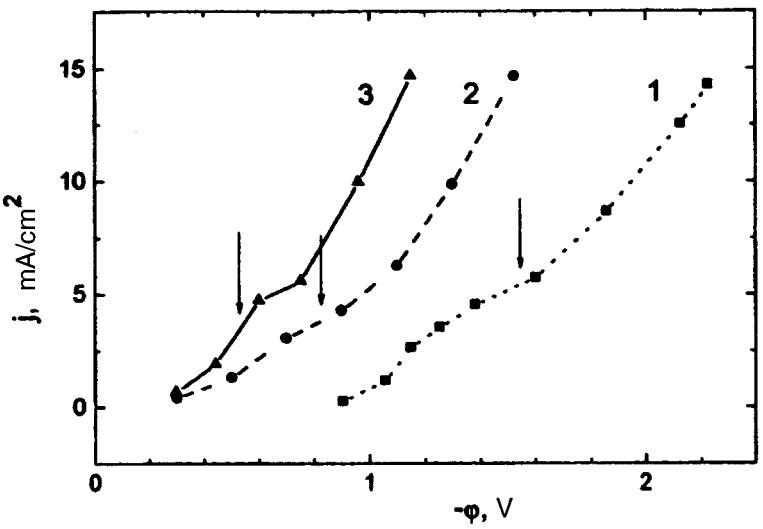

FIG. 2. Current density j versus cathode potential φ relative to saturated calomel electrode. The arrows indicate the onset of visible luminescence from the porous silicon. The acetone concentration (%) in the electrolyte is: *1* — 0, *2* — 25, and *3* — 50.

contact directly with the silicon substrate or with macrocrystallites on the substrate. The resistivity of the electrolyte is approximately 10 $\Omega\cdot$cm and as a result of quantum-well broadening of the band gap, the resistivity of the microcrystallites is 10^6–10^8 times higher than that of the substrate.[6] It can therefore be confirmed that the electrolyte efficiently shunts the high-resistivity microcrystallites. Under these conditions, electroluminescence should be completely absent in the visible range, which does not correlate with the experimentally achieved luminescence quantum yield of around 10^{-2} (Ref. 1). This contradiction has not yet been adequately explained.

Note that the visible luminescence occurs at the point where the polarization curves flatten out, and the potential at which this occurs and the potential for the onset of hydrogen evolution decrease with increasing acetone concentration in the electrolyte. Thus a clear correlation can be established between the occurrence of emission and the onset of hydrogen evolution.

The visible luminescence is caused by the recombination of electrons and holes in microcrystallites. Since the microcrystallites are not electrically conducting, the carriers must obviously be transferred to the microcrystallites by a different method. The mechanism for injection of holes in semiconductors with a smooth surface in contact with a persulfate electrolyte is fairly well-known.[7] Short-lived but extremely active electron acceptors known as ion radicals, $(SO_4)^-$, are formed at the cathode as the current flows. These ion radicals interact with the surface of the semiconductor, trapping electrons from the valence band, i.e., injecting holes. If we assume that the ion radicals possess finite lifetimes and are capable of diffusing in the electrolyte, this mechanism may be extended to porous silicon. By diffusing in the electrolyte and becoming adsorbed at the surface of microcrystallites, these ion radicals may inject holes into the microcrystallites. The holes are therefore transported to the microcrystallites in the porous crystal by a diffusive ionic mechanism.

It has already been noted that when the electrode potential is sufficiently negative, hydrogen ions begin to be reduced with the formation of atomic hydrogen, which is a strong reducing agent, i.e., an electron donor. Some of the hydrogen atoms then associate to form molecules and gaseous hydrogen is released at the electrode. Other hydrogen atoms diffuse in the electrolyte and may become adsorbed on the surface of the electrically neutral size-quantized microcrystallites. A comparison between the standard electrochemical potential of atomic hydrogen (-2.1 V relative to a saturated calomel electrode) with the position of the Fermi level in silicon shows that atomic hydrogen is an energetic electron donor relative to silicon and is capable of injecting electrons directly into the conduction band of the microcrystallites (Fig. 2).

Both holes and electrons can therefore be injected from the electrolyte into porous silicon microcrystallites which possess only intrinsic conductance or are not even coupled electrically to the substrate. In this case the electrical neutrality of the microcrystallites is conserved and the bipolar injection of carriers into the microcrystallites produces visible luminescence.

An increase in the wettability of porous silicon by the electrolyte enhances the contact with the substrate and ensures that sufficient charge carriers are generated, both ion radicals and hydrogen atoms. At the same time, this good wettability establishes contact between the electrolyte and an extensive surface, which results in adsorption of $(SO_4)^-$ ions and hydrogen atoms by numerous microcrystallites, efficient injection of charges into these microcrystallites, and thus produces more efficient electroluminescence.

In systems comprising porous silicon and an electrolyte, it has therefore been found that charges are transferred to the electroluminescence centers of the microcrystallites by an ion diffusion mechanism rather than an electron mechanism. This should give rise to delayed luminescence kinetics in these systems. In our experiments[8] we did in fact observe millisecond time delays of the emission pulses relative to the current pulses. This observation gives strong support to the proposed concept.

This work was partially supported by the Russian Fund for Fundamental Research (Grant No. 96-02-17903) and by INTAS (Grant No. 93-3325-ext).

[1] P. M. M. C. Bressers, J. W. J. Knapen, E. A. Meulenkamp *et al.*, Appl. Phys. Lett. **61**, 108 (1992).
[2] L. V. Belyakov, D. N. Goryachev, O. M. Sreseli *et al.*, Fiz. Tekh. Poluprovodn. **27**, 1815 (1993) [Semiconductors **27**, 999 (1993)].
[3] R. Herino, G. Bomchil, K. Barla *et al.*, J. Electrochem. Soc. **134**, 1994 (1987).
[4] L. Canham and A. Groszek, J. Appl. Phys. **72**, 1558 (1992).
[5] A. Halimaoui, Appl. Phys. Lett. **63**, 1264 (1993).
[6] S. P. Zimin, Pis'ma Zh. Tekh. Fiz. **20**(7), 55 (1994) [Tech. Phys. Lett. **20**, 285 (1994)].
[7] R. Memming, J. Electrochem. Soc. **116**, 785 (1969).
[8] O. M. Sreseli, D. I. Kovalev, G. Polisskiĭ *et al.*, Abstracts of papers presented at the Second Russian Conference on Semiconductor Physics, Vol. 2, [in Russian], Russian Academy of Sciences (1996), p. 218.

Translated by R. M. Durham

Kinetic model of GaAs(100) growth from molecular beams

S. Yu. Karpov and M. A. Maĭorov

Advanced Technology and Development Center, St. Petersburg
(Submitted November 10, 1996)
Pis'ma Zh. Tekh. Fiz. **23**, 64–71 (January 12, 1997)

A kinetic model for the growth of GaAs(100) by molecular beam epitaxy is constructed. The elementary processes at the surface are analyzed, including chemisorption of atoms and molecules, incorporation of atoms into the crystal, decomposition of the crystal, and desorption of group-III atoms and group-V molecules in vacuum. The sticking coefficients and rate constants are obtained from a direct comparison with experimental data. The model can be used to determine the desorbed and reflected fluxes, the growth rate, and the coverage by groups III and V atoms as functions of the incident fluxes and temperature. The model can also be used to estimate the limits of validity of the thermodynamic approach and the minimum epitaxy temperature. The results of the calculations show good agreement with the experimental observations. [S1063-7850(97)01201-9]

A kinetic model is proposed for the growth of GaAs(100) by molecular beam epitaxy, with a minimum number of parameters that can be estimated by comparison with experiment.

We consider the elementary processes taking place at the surface of GaAs(100): chemisorption of group-III atoms and group-V molecules, incorporation of group-III and group-V atoms from the adsorbed layer into the crystal, decomposition of the crystal, where atoms are transferred back to the adsorbed layer, and desorption of atoms and molecules from the adsorbed layer into vacuum. We confine ourselves to the processes taking place in a single adsorbed layer incorporating anion and cation sublayers. We shall assume that the crystal grows layer-by-layer and that the probability of nucleation on terraces between steps is low. The cation sublayer adjacent to the crystal is assumed to be filled with gallium (Ga) atoms while the anionic (upper) sublayer may contain chemisorbed gallium and arsenic (As) atoms. The unoccupied sites in the anionic layer are assumed to be vacancies. We assume that the adsorbed atoms are distributed statistically over the surface, i.e., we neglect cooperative effects, dimerization of atoms, and the influence of surface reconstruction.

It is well known that the sticking coefficient of Ga atoms on a GaAs(100) surface is close to unity and does not depend on its state. This implies that the lifetime of the gallium-on-gallium and gallium-on-arsenic complexes formed in the adsorption process is considerably longer than the characteristic time for hopping of atoms between neighboring lattice sites. In this case, the interaction between Ga atoms and the surface is nonlocal: an atom migrates and finds a vacant site before it is desorbed from the adsorbed layer. It is assumed that the Ga atoms exhibit similar behavior when the crystal undergoes decomposition.

The sticking coefficient of As_n molecules depends on the coverage by adsorbed As atoms and on the type of interacting molecules (As_2 or As_4). In Ref. 1 we constructed a model where the sticking coefficients of dimers (As_2) and tetramers (As_4) on a GaAs(100) surface are related to the arsenic coverage θ_{As} by

$$S_{As_2}=(1-\theta_{As})^2; \quad S_{As_4}=\frac{s_m\cdot(1-\theta_{As})^2}{1-s_m+s_m\cdot(1-\theta_{As})^2}, \qquad (1)$$

where $s_m=0.5$ is the maximum sticking coefficient of As_4 on a GaAs(100) surface.[2]

The growth rate v_g is determined by competing processes of incorporation of atoms into the crystal and decomposition of the crystal. Introducing the incorporation (γ) and decomposition (d) rate constants and assuming that the atoms obey a statistical distribution in the adsorbed layer, and imposing above assumptions, we can derive

$$\nu_g=\gamma\cdot\theta_{Ga}\cdot\theta_{As}-d\cdot(1-\theta_{As}), \qquad (2)$$

where θ_{Ga} is the gallium atom coverage.

The main particles desorbed from the GaAs(100) surface are gallium atoms and arsenic dimers.[3] The rate of desorption is governed by the appropriate desorption rate constant (k_{Ga} or k_{As_2}) and by the coverage (θ_{Ga} or θ_{As}). In this case, desorption of As_2 is a second-order reaction.[4,5]

With this reasoning in mind and assuming that the growing crystal is stoichiometric, we can obtain rate equations describing the dynamics of the change in the coverage by groups III and V atoms:

$$\frac{\partial\theta_{Ga}}{\partial t}=F_{Ga}-k_{Ga}\cdot\theta_{Ga}-\nu_g(\theta_{Ga},\theta_{As}),$$

$$\frac{\partial\theta_{As}}{\partial t}=n\cdot s_{As_n}\cdot F_{As_n}-2k_{As_2}\theta_{As}^2-\nu_g(\theta_{Ga},\theta_{As}), \qquad (3)$$

where F_{Ga} and F_{As_n} are the external fluxes of the components measured in monolayers per second. The system (3) can be used to calculate the surface coverage by groups III and V atoms, the crystal growth rate, the sticking coefficient of group-V molecules, and the desorbed fluxes of the components as functions of the external fluxes and temperature.

A solution of system (3) exists for $\theta_{Ga}+\theta_{As}\leqslant 1$. This condition follows from the assumption that the surface processes take place in a single adsorbed layer. Otherwise, excess Ga or As builds up on the surface. Under steady-state conditions, the inequality $\theta_{Ga}+\theta_{As}\leqslant 1$ is satisfied when

$$\theta_- \leqslant \theta_{\mathrm{As}} \leqslant \theta_+ ,$$

where

$$\theta_\pm = (2\gamma)^{-1}[(\gamma + d - k_{\mathrm{Ga}}) \pm \sqrt{(\gamma - d + k_{\mathrm{Ga}})^2 - 4\gamma F_{\mathrm{Ga}}}]. \quad (4)$$

The rate constants generally depend exponentially on the reciprocal temperature. It can be seen from Eq. (4) that at low enough temperatures when the rate constants are comparable with or smaller than the external fluxes, the steady-state solution of system (3) vanishes. This takes place at the temperature T_e which may be estimated from

$$F_{\mathrm{Ga}} = \frac{1}{4}\gamma^{-1}(\gamma - d + k_{\mathrm{Ga}})^2 \cong \frac{1}{4}\gamma(T_e) \quad \text{for } \gamma \gg d,\ k_{\mathrm{Ga}}. \quad (5)$$

In fact T_e is the minimum epitaxy temperature below which layer-by-layer crystal growth is terminated because of the accumulation of excess group III or V atoms on the surface.

We need to estimate the constants k_{Ga}, k_{As_2}, γ, and d to compare theory with experiment. The constant k_{As_2} is taken in accordance with the recommendations made in Refs. 2 and 5. It was shown in Ref. 6 that the rate of desorption of group-III atoms from a III–V surface is similar to the rate of vaporization of the corresponding element from the liquid phase. The desorption constant of Ga was determined using data on its saturated vapor pressure above the liquid phase.[7]

We estimated γ using experimental data on the phase diagram of a GaAs(100) surface.[8] It was noted in Ref. 8 that for any external Ga flux, there exists a temperature below which the growing surface suddenly exhibits roughness. Associating this temperature with the minimum epitaxy temperature T_e and using relation (5), we can estimate the constant γ and its temperature dependence from a comparison with the data from Ref. 8.

The other constant d may be found by considering ''vapor–crystal'' thermodynamic equilibrium for which two conditions are satisfied: a) the rate of growth (vaporization) is zero and b) the component fluxes leaving the surface have the same magnitude and composition as the incoming fluxes. For gallium arsenide the equilibrium vapor contains predominantly As_2 dimers and Ga atoms.[9,10]

In equilibrium the Ga and As_2 fluxes ($F_{\mathrm{Ga}}^{\mathrm{eq}}$ and $F_{\mathrm{As}_2}^{\mathrm{eq}}$) are interrelated in accordance with the law of mass action:

$$F_{\mathrm{Ga}}^{\mathrm{eq}} \cdot (F_{\mathrm{As}_2}^{\mathrm{eq}})^{1/2} = K_{\mathrm{GaAs}}^{*} \beta_{\mathrm{Ga}} \beta_{\mathrm{As}_2}^{1/2} = K_{\mathrm{GaAs}}, \quad (6)$$

where K_{GaAs}^{*} is the equilibrium constant of GaAs formation from the gas phase, $\beta_\nu = (2\pi m_\nu k_B T)^{-1/2}$ is the Hertz–Knudsen factor, m_ν is the atomic (molecular) mass, and k_{B} is the Boltzmann constant. Expressing the equilibrium conditions (a) and (b) from Eqs. (2) and (3), and using Eq. (6), we can obtain a relation linking the rate constants of the elementary processes:

$$k_{\mathrm{Ga}} \cdot d \cdot k_{\mathrm{As}_2}^{1/2} / \gamma = K_{\mathrm{GaAs}}. \quad (7)$$

Table I gives the activation energies and preexponential factors of the rate constants extrapolated in Arrhenius form. For external Ga and As_2 fluxes the system (3) can have the approximate analytic solutions:

$$\theta_{\mathrm{As}} \cong 1 - \sqrt{F_{\mathrm{Ga}}/2F_{\mathrm{As}_2}}, \quad \nu_g \cong F_{\mathrm{Ga}}$$
$$\text{for } K_{\mathrm{GaAs}}^{2/3} \ll k_{\mathrm{As}_2} \ll F_{\mathrm{As}_2},\ F_{\mathrm{Ga}}, \quad (8)$$

$$\theta_{\mathrm{As}} \cong \sqrt{\Delta F / k_{\mathrm{As}_2}}, \quad \nu_g = F_{\mathrm{Ga}} - K_{\mathrm{GaAs}}/(\Delta F)^{1/2}$$
$$\text{for } K_{\mathrm{GaAs}}^{2/3} \ll F_{\mathrm{As}_2},\ F_{\mathrm{Ga}} \ll k_{\mathrm{As}_2}, \quad (9)$$

where $\Delta F = F_{\mathrm{As}_2} - \frac{1}{2}F_{\mathrm{Ga}}$. Solution (8a) corresponds to moderate and low temperatures while solution (8b) corresponds to high temperatures, where the growth rate decreases with increasing temperature as a result of desorption of gallium. Expression (8b) is also valid for an As_4 flux if F_{As_2} is replaced by $2s_m F_{\mathrm{As}_4}$.

We calculated the temperature dependence of the GaAs(100) growth rate to compare theory with experiment (Fig. 1). The data taken from Ref. 11 correspond to an external gallium flux of 1 ML/s. The experimental points in Ref. 11 were obtained for an external flux $F_{\mathrm{As}_2} = 1.9$ ML/s and $F_{\mathrm{As}_4} = 3.8$ ML/s. A numerical solution of system (3) and the analytical relations (8) yielded curves of $\nu_g(T)$ with a relative temperature shift of less than 2 K.

TABLE I. Activation energies and preexponential factors of rate constants extrapolated in the form $R = R_0 \exp(-E_a/k_B T)$.

R	R_0	E_a, eV
K_{GaAs}	1.03×10^{23} (ML/s)$^{3/2}$	4.56
k_{As_2}	2.21×10^{22} (ML/s)	3.90
k_{Ga}	4.16×10^{13} (ML/s)	2.71
γ	5.36×10^{8} (ML/s)	1.07
d	8.89×10^{6} (ML/s)	0.97

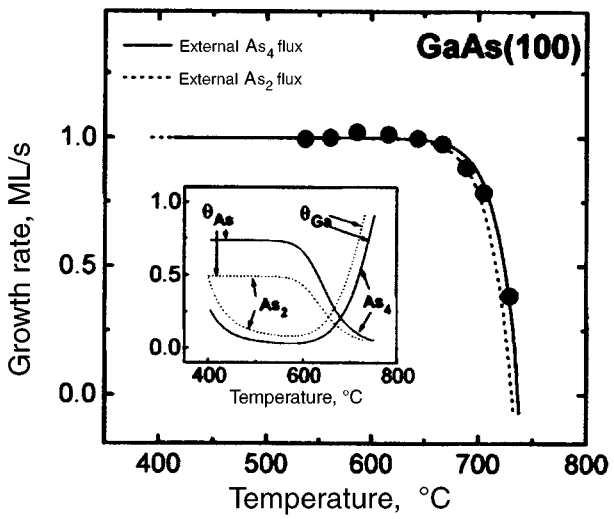

FIG. 1. Growth rate versus temperature. Data[11] obtained for an incoming arsenic flux $F_{\mathrm{As}_2} = 1.9$ ML/s and $F_{\mathrm{As}_4} = 3.8$ ML/s. The dashed and solid lines give the theoretical curves. The inset shows the change in coverage for these cases.

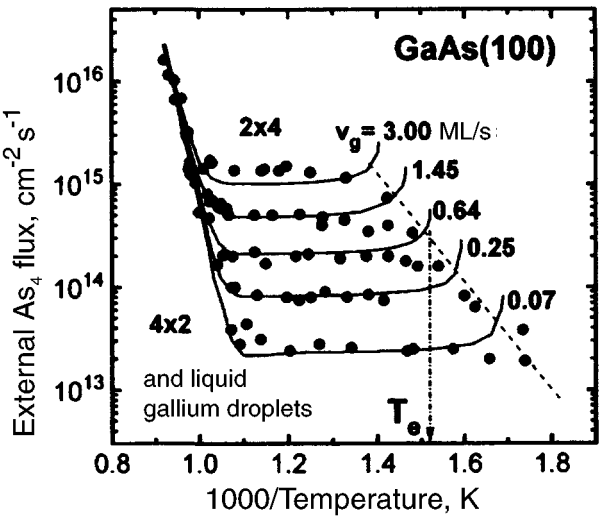

FIG. 2. Limit of formation of the liquid phase. The experimental points[8] corresponds to a $(2\times4)\rightarrow(4\times2)$ transition at various growth rates. The minimum epitaxy temperature is indicated at a growth rate of 0.64 ML/s.

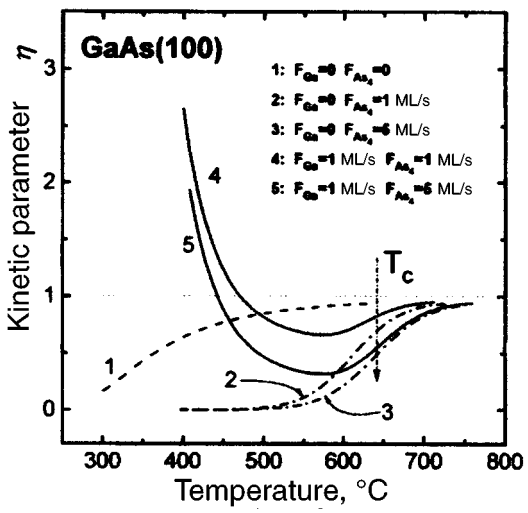

FIG. 3. Kinetic parameter η as a function of external fluxes and temperature. The thermodynamic approach is valid for $\eta\approx1$.

It has been noted[8] that the accumulation of more than one monolayer of gallium atoms on a GaAs surface results in the formation of a liquid phase. In our model this corresponds to a decrease in the coverage θ_{As} to values less than θ_- [see Eq. (4)]. Estimates show that at temperatures exceeding T_e by more than 40 K and θ_{As} close to θ_-, the adsorbed layer is almost completely filled with gallium atoms. The condition $\theta_{\mathrm{As}}\cong\theta_-$ can thus be taken as the limit for the appearance of the liquid phase on the surface. In Fig. 2 the curves calculated from the condition $\theta_{\mathrm{As}}\cong\theta_-$ are compared with the experimental points corresponding to the transition to a Ga-stabilized (4×2) surface, which is accompanied by the formation of liquid gallium droplets.[9] It can also be seen from Fig. 2 that the minimum epitaxy temperature for $F_{\mathrm{Ga}}=0.64$ ML/s is $T_e\approx370$°C.

In the thermodynamic approach[10,12,13] frequently used to describe the growth of III–V compounds, the fluxes of desorbed components from the surface (F^d_{Ga} and $F^d_{\mathrm{As}_2}$) are assumed to be interrelated as in Eq. (6). In order to estimate the limits of validity of the thermodynamic calculations, we introduced the parameter η:

$$\eta=\frac{F^d_{\mathrm{Ga}}(F^d_{\mathrm{As}_2})^{1/2}}{K_{\mathrm{GaAs}}}\ . \tag{10}$$

Values of η close to unity correspond to validity of the thermodynamic approach, but, as can be seen from Fig. 3, except for the case of free vaporization this condition is only satisfied in a limited range of relatively high temperatures.

The proposed kinetic model may be generalized to other III–V semiconductors, including multicomponent compounds.

This work was supported by the International Science Foundation (Grant No. 16300).

[1] S. Yu. Karpov and M. A. Maiorov, Surf. Sci. **344**, 11 (1995).
[2] C. T. Foxon and B. A. Joyce, Surf. Sci. **50**, 434 (1975).
[3] T. M. Brennan, J. Y. Tsao, and B. E. Hammons, J. Vac. Sci. Technol. A **10**, 33 (1992).
[4] J. R. Arthur, Surf. Sci. **43**, 449 (1974).
[5] J. Y. Tsao, T. M. Brennan, J. F. Klem, and B. E. Hammons, J. Vac. Sci. Technol. A **7**, 2138 (1989).
[6] J. A. McCaulley and V. M. Donnelly, J. Chem. Phys. **91**, 4330 (1989).
[7] *Tables of Physical Quantities: Handbook*, ed. by I. K. Kikoin [in Russian], Atomizdat, Moscow (1976).
[8] S. M. Newstead, R. A. A. Kubiak, and E. H. C. Parker, J. Cryst. Growth **81**, 49 (1987).
[9] J. R. Arthur, J. Phys. Chem. Solids **28**, 2257 (1967).
[10] H. Seki and A. Koukitu, J. Cryst. Growth **78**, 342 (1986).
[11] A. J. SpringThorpe and P. Mandeville, J. Vac. Sci. Technol. B **6**, 754 (1988).
[12] R. Heckingbottom, in *Molecular Beam Epitaxy and Heterostructures*, NATO-ASI Series E: Applied Science, No. 87, ed. by L. L. Chang and K. Ploog (Martinus Nijhoff, Dordrecht, 1985) [Russ. transl., Mir, Moscow, 1989].
[13] J.-Y. Shen and C. Chatillon, J. Cryst. Growth **106**, 553 (1990).

Translated by R. M. Durham

Mesa stripe for the 3–3.6 μm range lasers utilizing gadolinium-doped InAsSbP/InGaAsSb double heterostructures

N. V. Zotova, S. A. Karandashev, B. A. Matveev, M. A. Remennyĭ, N. M. Stus', and G. N. Talalakin

A. F. Ioffe Physicotechnical Institute, Russian Academy of Sciences, St. Petersburg
(Submitted November 10, 1996)
Pis'ma Zh. Tekh. Fiz. **23**, 72–76 (January 12, 1997)

Data are presented on diode mesa stripe lasers utilizing InAsSbP/InGaAsSb double heterostructures, which are the first long-wavelength lasers to be doped with the rare-earth element gadolinium. It is shown that doping enhances the threshold characteristics. Measurements made of the current modulation of the laser radiation indicate that these lasers may be used in spectroscopic measurements. © *1997 American Institute of Physics.* [S1063-7850(97)01301-3]

Diode lasers utilizing narrow-gap semiconductors emitting in the middle infrared (3–5 μm) may be used in spectroscopy and to monitor atmospheric pollution since the absorption bands of many industrial gases such as CH_4 (3.3 μm), HCl (3.54 μm), CO_2 (4.2 μm), and CO (4.6 μm) lie in this spectral range. In addition, when these sources are used in conjunction with chalcogenide and fluorite glass fibers, the optical losses are reduced by an order of magnitude compared with quartz fibers, making these lasers promising for applications in fiber-optic communication lines.[1]

In the present paper we report mesa stripe lasers emitting in the 3.2–3.5 μm spectral range, utilizing InAsSbP/InGaAsSb/InAsSbP double heterostructures fabricated by liquid-phase epitaxy on n-InAs(111) substrates with a gadolinium-doped n-InGaAsSb active layer.

The literature contains little information on structures grown on (111)-oriented n-InAs substrates although growing heterostructures on (111)-oriented substrates at high temperatures (conditions for high substrate plasticity) can produce graded-index layers and double heterostructures with a low mismatch dislocation density because of the preferential formation of defects in the substrate.[2,3] To the best of our knowledge, the active region of long-wavelength double-heterostructure lasers has not so far been doped with rare-earth elements.

The double heterostructures were prepared as described in Ref. 4 and consisted of an undoped n-InAs(111) substrate ($n=(1–2)\times10^{16}$ cm^{-3}) and three layers: a wide-gap n-$InAs_{1-x-y}Sb_xP_y$ confining layer, an n-$In_{1-v}Ga_vAs_{1-z}Sb_z$(Gd) laser active layer ($0.01\leqslant v\leqslant0.07$, $0.065\leqslant z\leqslant0.07$), and a p-(Zn)-$InAs_{1-x-y}Sb_xP_y$ wide-gap emitter ($0.05\leqslant x\leqslant0.09$, $0.09\leqslant y\leqslant0.18$). The thickness of the wide-gap layers was 4–6 μm and that of the active layer was 1.5–3 μm. Mesa stripe lasers with a stripe width of 10 or 20 μm were fabricated by photolithography and were 200–1000 μm long.

Measurements of the Hall effect revealed that doping InGaAsSb epitaxial layers with gadolinium reduces the electron concentration from 1×10^{17} to $\sim4\times10^{15}$ cm^{-3} and increases their mobility to $\sim10^5$ cm^2/V·s. When the InGaAsSb active layer in an InAsPb/InGaAsSb/InAsSbP double heterostructure is doped, the half-width of the photoluminescence spectra of the active-layer material is reduced

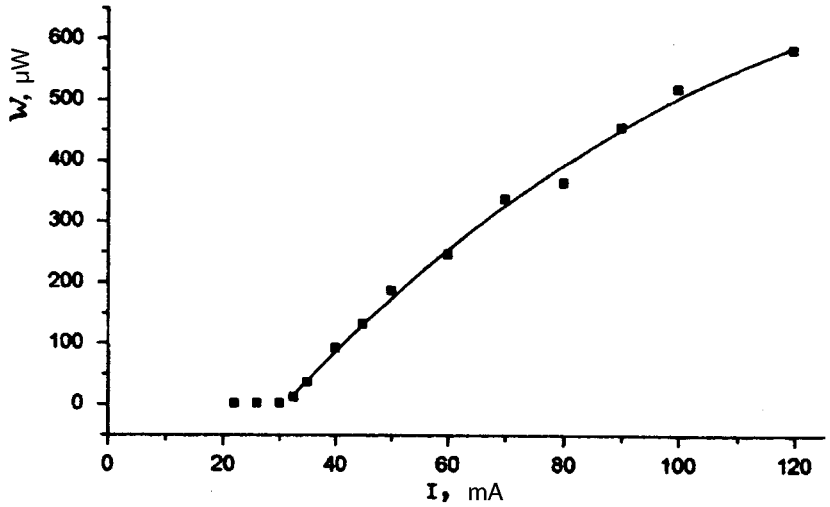

FIG. 1. Current-power characteristic of a pulsed laser (5 μs, 500 Hz), with a gadolinium-doped InGaAsSb active region and a stripe width of 20 μm, T = 77 K (W is the pulse power).

 1063-7850/97/010041-02$10.00

TABLE I.

		W, μm	λ, μm	J_{th}, A/cm^2	I_{th}, A
InGaAsSb	Gd	20	3.335	350	35
InGaAsSb	-	20	3.49	800	70
InGaAsSb	Gd	10	3.355	2000	75
InGaAsSb	-	10	3.324	2600	130
InAs	Gd	10	3.228	950	100
InAs	-	10	3.164	10000	390

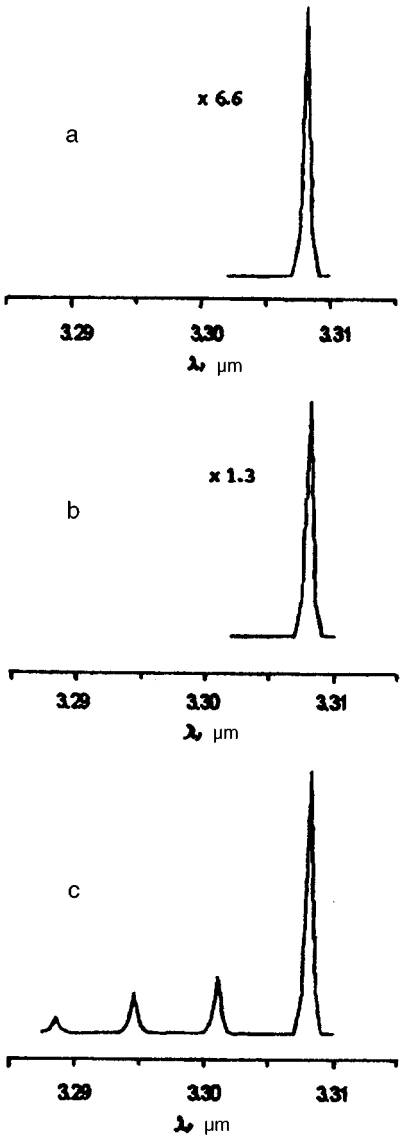

FIG. 2. Laser spectra for various currents: a—I_{th}, b—1.7I_{th}, and c—2I_{th}.

to $\sim$1.5 kT (77 K), the emission intensity is increased $\sim$20–30 times, and the threshold lasing current is reduced, as can be seen from Table I. This behavior may be caused by the formation of complexes[5] which reduce the residual donor concentration.

Table I gives the main parameters of the fabricated lasers: the active region material and dopant, the stripe width W, the lasing wavelength λ, the threshold current density J_{th}, and the threshold current I_{th} at $T=77$ K. An increase in the threshold current with decreasing stripe width is evidently caused by an increase in the leakage current across the side surfaces of the stripe. Figure 1 gives the current-power characteristic of one of these lasers operating in a pulsed mode (pulse length 5 μs and repetition frequency 500 Hz). Figure 2 gives laser radiation spectra for various currents. It can be seen that single-mode lasing is observed in the range $I=(1–2)I_{th}$. A Fabry–Perot resonator was used to measure the shift of the lasing mode with increasing pump current. The tuning rate was $\sim$30 cm^{-1}/A in the long-wavelength direction: for I_{th} = 30 mA, the red shift of the mode was 5.1 Å when the current was increased by 18 mA, which satisfies the requirements for most applications of laser diode spectroscopy. The lasers possess stable parameters (output power and threshold current) and we are hopeful that they can be used in gas analysis systems.

The authors would like to thank M. Aĭdaraliev and N. D. Il'inskaya for help with fabricating the lasers, A. N. Imenkov for making the mode tuning measurements, and also Yu. P. Yakovlev for his attention and interest in this work. This work was carried out as part of the ''Optics. Laser Physics'' program (Project 4.14).

[1] C. H. L. Goodman, Solid State Electron. Dev. **2**(5), 129 (1978).
[2] B. A. Matveeev, N. M. Stus', and G. N. Talalakin, Kristallografiya **33**, 216 (1988) [Sov. J. Crystallogr. **33**, (1988)].
[3] T. S. Argunova, R. N. Kyutt, B. A. Matveev *et al.*, Fiz. Tverd. Tela **36**, 3071 (1994) [Phys. Solid State **36**, 1633 (1994)].
[4] M. Aydaraliev, N. V. Zotova, S. A. Karandashov *et al.*, Semicond. Sci. Technol. **8**, 1575 (1993).
[5] A. N. Baranov, T. I. Voronina, T. S. Lagunova *et al.*, Fiz. Tekh. Poluprovodn. **27**, 421 (1993) [Semiconductors **27**, 236 (1993)].

Translated by R. M. Durham

Use of a scanning charge-coupled photodetector for compression of optical signals with linear wavelength modulation

N. A. Esepkina and A. P. Lavrov

St. Petersburg State Technical University
(Submitted October 28, 1996)
Pis'ma Zh. Tekh. Fiz. **23**, 77–81 (January 12, 1997)

An analysis is made of a processor for compression of optical signals with linear wavelength modulation. The processor system is equivalent to a diffraction spectrometer except that a linear charge-coupled photodetector operating in a delay-and-add mode is inserted in its spectral plane. By this means the processor isolates the signal from the noise and is invariant to the signal arrival time, and it can be tuned by a simple electronic technique to select signals with a different rate of change in wavelength. The compression coefficient may be several thousand. Other characteristics of the processor and its maximum capabilities are discussed.
 [S1063-7850(97)01401-8]

1. Optical methods of signal processing are attracting serious attention because of their unique potential. This potential arises from the structure of optical processors and their components whose refinement will enhance their capabilities. However new scope for the development of optical processors is offered by using known components in unconventional operating modes. An example is a processor incorporating multielement charge-coupled photosensitive devices operating not in the standard mode as an optical image detector but in a special delay and add mode, in other words in a continuous scanning mode.[1] Optical processors have therefore been constructed for various applications, including linear signal conversion (convolution, correlation, spectral analysis), formation of a radio image of a region in synthesized-aperture systems, tracking the motion of an image in optical telescopes with fixed mirrors, and so forth.[2–6] We have shown that an efficient acoustooptic processor for compression of radio signals with linear frequency modulation can be developed by incorporating a linear photosensitive charge-coupled device, operating in a delay-and-add mode, in a well-known acoustooptic spectrum analyzer for radio signals.[4,5] In the present paper we consider a similar processor for compression of optical signals with linear wavelength modulation.

2. The optical signal processor is shown schematically in Fig. 1. A collimated light beam of wavelength λ is incident at the angle α to the normal on a plane transmission diffraction grating with the line period d. The diffracted light is collimated by an objective L of focal length F having a linear multielement charged-coupled photodetector operating in a time delay and storage mode, inserted in its focal plane. Clock signals at frequency f are fed to the photodetector from a controller to ensure continuous motion of the potential wells in the photodetector and its coupled elements. The output signal from the charge-coupled photodetector is the processor output signal. This optical system corresponds to a conventional diffraction spectrometer. The angle of diffraction β relative to the normal to the grating is determined by the grating equation[7]

$$n\cdot\lambda = d\cdot(\sin\alpha+\sin\beta), \tag{1}$$

where $n=\pm1,\pm2$, and so forth, is the diffraction order. We shall analyze the first order ($n=1$).

If the collimated beam incident on the diffraction grating is linearly modulated with respect to wavelength in accordance with the expression

$$\lambda(t)=\lambda_0+a\cdot t, \quad 0\leqslant t\leqslant T_c, \tag{2}$$

where a is the rate of change in wavelength (the rate of linear modulation), T_c is the duration of the modulated optical signal, and λ_0 is the average signal wavelength, a narrow spatial distribution or response is formed in the spectral plane of the spectrometer, whose position l is given by

$$l(t)=l_0+v_s\cdot t, \tag{3}$$

where v_s is the rate of displacement of the response, which is determined by the rate of change in the diffraction angle $d\beta/dt$ as given by

$$v_s=F\cdot d\beta/dt; \tag{4}$$

l_0 is the position of the response at time $t=0$. The position of the origin for the coordinate l is not important in this analysis.

In this operating mode the elements of the photodetector, comprising a multielement shift register with optically transparent polycrystalline silicon electrodes, are transported by a continuous ladder network (conveyor) from one end of the photosensitive region to the other and the elements also detect the optical signal and store it in the form of charge packages.[1] At the output of the charge-coupled photosensitive device, these charge packets are converted into the output voltage. The transport rate of the elements v_e is equal to $l_e\cdot f$, where l_e is the spacing of the elements in the photodetector, and f is the clock frequency.

When the transport rate of the photodetector elements and of the spectral response are equal, a group of elements is transported synchronously with the latter, accumulating charge packets proportional to the light intensity in the response. At a time uniquely related to the time of application of an optical linearly wavelength-modulated signal to the spectrometer, a short video pulse is observed at the photode-

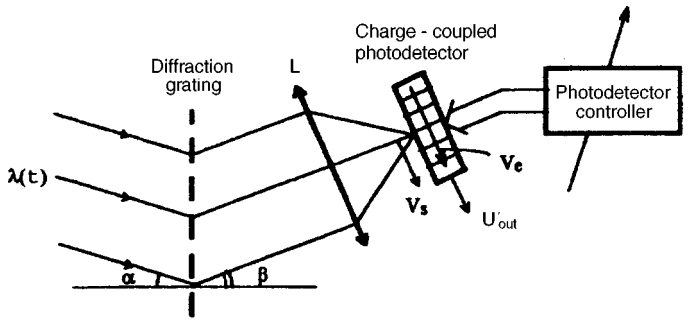

FIG. 1. Schematic diagram of optical processor for compression of linearly wavelength-modulated optical signals.

tector exit, its amplitude proportional to the energy of this signal. The processor thus compresses and detects the linearly modulated signal.

In order to determine the condition for equal velocities of scanning and of the response, we analyze expression (4). Expressing the rate of change in the angle of diffraction in terms of the angular dispersion of the diffraction grating

$$d\beta/dt=(d\beta/d\lambda)\cdot(d\lambda/dt) \tag{5}$$

and using expressions (1) and (2), we obtain

$$d\beta/dt=a/(d\cdot\cos\beta) \tag{6}$$

and thus

$$v_s=F\cdot a/(d\cdot\cos\beta). \tag{7}$$

The rate of displacement of the response must remain constant for the duration of the processed signal in order to obtain the maximum output signal for the minimum duration in this processor. To linearize the time displacement of the response in the spectral plane, it is advisable to select the spectrometer parameters so that for $\lambda=\lambda_0$, the angle of diffraction is $\beta=0$, and the axis of the objective L coincides with the normal to the grating. In this case, the velocity can be assumed to be constant and equal to $v_{s0}=a\cdot F/d$ over a fairly large wavelength range $\lambda_0\pm\Delta\lambda$.

From the condition of equal velocities we then have

$$f=a\cdot F/(d\cdot l_e) \tag{8}$$

from which it can be seen that the required clock frequency of the charge-coupled photodetector is directly proportional to the rate of linear modulation of the wavelength in the processed (compressed) signal. When the rate of linear modulation changes, the clock frequency must be altered by a simple electronic technique. The processor can therefore be tuned electronically to process different linearly wavelength-modulated signals.

When the velocities of the elements and the response differ, the output signal from the charge-coupled photodetector decreases rapidly in magnitude and increases in duration, which makes the processor selective to the modulation rate signals defined by the clock frequency.

It is important to note that background illumination from wide-band and monochromatic noise only alters the constant component in the processor output signal.

We examine the main characteristics of the processor.

A. Duration of compressed output signal from processor.

The duration of the compressed signal is determined by the time δ_t for propagation of the wavelength of the processed signal across the width of an equivalent spectral channel (spectrometer resolution) $\delta\lambda$:

$$\delta_t=\delta\lambda/a. \tag{9}$$

It is known[7] that the resolution of a spectrometer is determined by its resolving power and is

$$\delta\lambda=\lambda_0/N, \tag{10}$$

where N is the number of lines in the diffraction grating. Thus we have

$$\delta_t=\lambda_0/(N\cdot a). \tag{11}$$

B. Compression coefficient of optical signal.

The compression coefficient is given by

$$K_{\text{com}}=T_s/\delta t=T_c\cdot a\cdot N/\lambda_0=N\cdot\Delta\lambda_s/\lambda_0, \tag{12}$$

where $\Delta\lambda_s$ is the range of wavelength variation in the processed signal. Since the resolving power N of the spectrometers may be thousands or tens of thousands, the compression coefficient K_{com} of this processor may be hundreds or even thousands.

C. In addition to the diffraction grating parameters, these processor characteristics are also influenced by the parameters of the charge-coupled photodetectors.

An upper limit on the compression coefficient is imposed by the finite number of elements N_e in the charge-coupled photodetector. When two or three measurements (photodetector elements) are used over the response length $\delta_1=\delta\beta\cdot E$, K_{com} cannot exceed $K_{\text{com}_{\max}}\approx(0.3\text{–}0.4)\cdot N_e$. Note that linear photodetectors with several thousand elements are now coming onto the market. A lower limit on the duration of the compressed signal in the processor is imposed by the response time of the charge-coupled photodetector since the velocity v_e of its components has an upper limit imposed by the inefficiency of the charge packet transfer. For commercially available silicon charge-coupled photodetectors with a bulk channel for charge packet transfer, the maximum clock frequency $f_{\max}$ is 10–20 MHz, which for two or three photodetector elements over the response length yields the estimate $\delta t_{\min}\approx$ 100–200 ns.

D. Range of signal wavelengths.

The range of signal wavelengths which may be processed in the processor is determined by the spectral range of

the photodetector and for silicon devices is 0.4–1.0 μm.

Advantages of this processor are: its indifference to the signal arrival time, its adaptivity—electronic tuning of modulation rate over a wide range, its high selectivity in terms of modulation rate, and its capacity to operate under strong background illumination by wide-band and monochromatic noise.

This processor may be used to develop various measuring systems, remote probing systems, and communication systems. A tunable external-cavity semiconductor laser may be used as a controllable source of linearly wavelength-modulated optical signals. The tuning range of these lasers is tens of nanometers.[8]

[1] D. F. Barb, in *Solid State Imaging*, NATO Advanced Study Institute Series E, No. 16, ed. by P. G. Jespers, F. van der Wiele, and M. F. White (Noordhoff, Leyden, 1976) [Russ transl., Mir, Moscow, 1979].
[2] M. A. Monohan, K. Bromley, and R. P. Bocker, Proc. IEEE **65**, 121 (1977).
[3] D. Psaltis, Proc. IEEE **72**, 962 (1984).
[4] S. Yu. Bondartsev, N. A. Esepkina, and A. P. Lavrov, Avtometriya No. 4, 89 (1986).
[5] N. A. Esepkina, A. P. Lavrov, M. A. Ananev, and N. N. Evtihiev, Proc. SPIE **1704**, 115 (1992).
[6] D. F. Schneider, M. Schmidt, and J. Gunn, Astron. J. **107**, 1245 (1994).
[7] R. A. Sawyer, *Experimental Spectroscopy* (Chapman and Hall, London, 1944) [Russ. transl., Inostr. Lit., Moscow, 1953].
[8] Z. Pang, H. Zhang, J. Yang *et al.*, Proc. SPIE **2482**, 269 (1993).

Translated by R. M. Durham

Acoustooptic interaction in uniaxial gyrotropic paratellurite crystals

G. V. Kulak

Mozyr' State Pedagogical Institute
(Submitted August 19, 1996)
Pis'ma Zh. Tekh. Fiz. **23**, 84–89 (January 12, 1997)

An analysis is made of an intermediate mode of light diffraction by ultrasound in a uniaxial gyrotropic paratellurite crystal. A system of coupled wave equations is presented to calculate the polarization and energy characteristics of the diffracted light for the Raman–Nath, intermediate, and Bragg modes of acoustooptic interaction. The diffraction of light propagating at small angles to the crystal optic axis by a slow ultrasonic shear wave propagating along the [110] crystallographic axis is studied. The amplitude–frequency characteristics of a modulator–deflector for optical radiation are investigated. Curves of the diffraction efficiency as a function of the ultrasonic wave intensity are plotted for various acoustooptic interaction lengths. © *1997 American Institute of Physics.* [S1063-7850(97)01501-2]

Acoustooptic interaction in uniaxial gyrotropic crystals has been investigated in Refs. 1–5. It was shown in Ref. 2 that paratellurite is one of the most promising crystals for fabricating acoustooptic information processing devices (such as modulators, deflectors, filters, processors, and so forth). It was suggested that the acoustooptic diffraction of light propagating at a small angle to the crystal optic axis by a slow ultrasonic shear wave propagating along the [110] crystallographic axis should be used. Highly efficient modulation of arbitrarily polarized multicomponent laser radiation controlled by an acoustic wave was studied in Ref. 5. The authors of Refs. 6 and 7 investigated acoustooptic interaction in the Raman–Nath, intermediate, and Bragg diffraction modes for a nongyrotropic insulator. It was shown that pure Bragg diffraction is not observed in practice. An intermediate interaction mode characterized by angular selectivity and several diffraction maxima is normally observed.

In the present paper the constitutive equations for a gyrotropic insulator[8,9] and the method of slowly varying amplitudes is used to analyze intermediate acoustooptic diffraction close to Bragg diffraction in a uniaxial gyrotropic paratellurite crystal.

When light propagates near the optic axis of an anisotropic crystal, the acoustooptic diffraction is determined by the Klein–Cook wave parameter $Q=f_0^2\lambda_0 l/nv^2$, where n is the refractive index in the direction of propagation of the incident light wave, λ_0 is the wavelength of light in vacuum, $f_0(v)$ is the frequency (phase velocity) of the ultrasonic wave, and l is the length of the acoustooptic interaction region.[6] Bragg diffraction is observed for $Q\to\infty$ and Raman–Nath diffraction is observed for $Q\to 0$ (Ref. 7). For a light wave incident at the Bragg angle $\varphi_B\approx\lambda_0 f_0/2nv$ and not too high ultrasonic power levels we can confine ourselves to four diffraction orders (as opposed to two for Bragg diffraction).[6]

We select the XYZ coordinate system so that the ultrasonic wave is excited in the direction of the X axis and a plane light wave is incident at the angle φ_B to the Z optical axis. The ultrasonic wave occupying the space between the

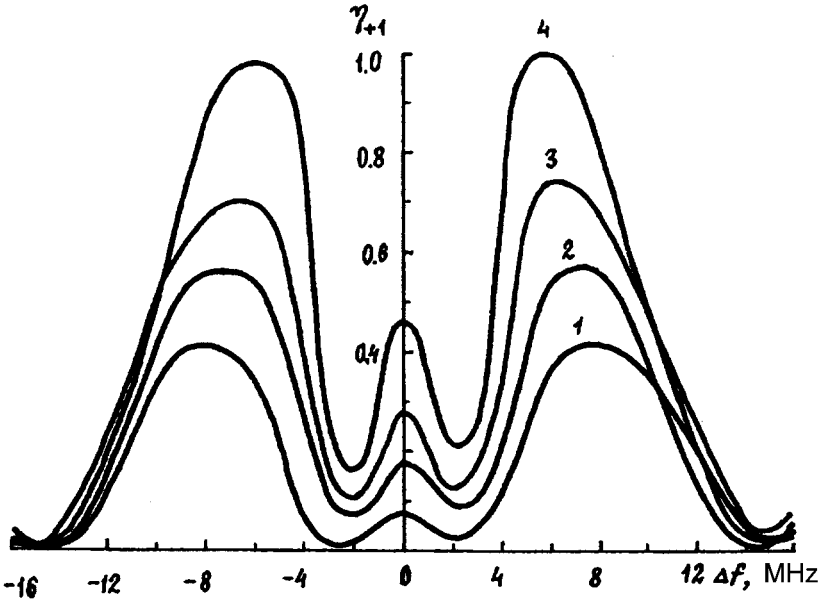

FIG. 1. Relative intensity η_{+1} of diffracted light versus detuning Δf of ultrasound frequency from the Bragg frequency for various ultrasonic wave intensities I_a: *1* — 0.15 W/cm^2, *2* — 0.25 W/cm^2, *3* — 0.35 W/cm^2, and *4* — 0.5 W/cm^2 ($l=1.2$ cm, $A_\parallel=1$, and $A_\perp=0$).

 1063-7850/97/010046-03$10.00

planes $z=0$ and $z=l$ induces a spatially and temporally periodic change in the permittivity tensor $\Delta\varepsilon_{ij}$, which is related to the elastic deformations $\hat{U}_{ik}=(1/2)(\nabla_k U_i+\nabla_i U_k)$ and the photoelastic constants $\hat{P}_{ijkl}$ by: $\Delta\hat{\varepsilon}_{ij}=-\hat{\varepsilon}_{il}\hat{\varepsilon}_{jk}\hat{P}_{lkmn}\hat{U}_{mn}$, where $\hat{\varepsilon}$ is the permittivity tensor of the unperturbed crystal.

The Maxwell equations and the constitutive equations[8,9] for a gyrotropic insulator yield the wave equation for the optical field intensity in the region occupied by the ultrasound, which is given in Refs. 4 and 10.

Using the results of Refs. 4 and 10, we derive a system of coupled wave equations for the complex amplitudes polarized in the diffraction plane (A_m) and orthogonal to the diffraction plane (B_m):

$$\frac{dA_m}{dz}=i\Delta^{an}_{ma}\cdot A_m+\rho_m\cdot B_m+i\chi^{a,a}_{m,m+1}A_{m+1}\exp(-i\delta_m z)$$
$$+i\chi^{a,b}_{m,m+1}B_{m+1}\exp(-i\delta_m z)$$
$$+i\chi^{a,a}_{m,m-1}A_{m-1}\exp(i\delta_{m-1}z)$$
$$+i\chi^{a,b}_{m,m-1}B_{m-1}\exp(i\delta_{m-1}z),$$

$$\frac{dB_m}{dz}=i\Delta^{an}_{mb}\cdot B_m-\rho_m\cdot A_m+i\chi^{b,a}_{m,m+1}\cdot A_{m+1}\exp(-i\delta_m z)$$
$$+i\chi^{b,b}_{m,m-1}B_{m+1}\exp(-i\delta_m z)$$
$$+i\chi^{b,a}_{m,m-1}A_{m-1}\exp(i\delta_{m-1}z)$$
$$+i\chi^{b,b}_{m,m-1}B_{m-1}\exp(i\delta_{m-1}z). \qquad (1)$$

Here the following notation is introduced:

$$\Delta^{an}_{ma,b}=q_m[e_{m,2}(\hat{\varepsilon}-\varepsilon)e_{m,2}],\quad \rho_m=(G_m k_m)/|k_m|,$$
$$\chi^{a,b}_{m,m+1}=q_{m+1}(e_m\Delta\hat{\varepsilon}e_2),\quad \chi^{a}_{m,m+1}=q_{m+1}(e_m\Delta\hat{\varepsilon}e_{m\pm1}),$$
$$\chi^{b,b}_{m,m-1}=q_{m-1}(e_2\Delta\hat{\varepsilon}e_2),\quad \chi^{a,a}_{m,m-1}=q_{m-1}(e_m\Delta\hat{\varepsilon}^*e_{m-1}),$$
$$\chi^{a,b}_{m,m-1}=q_{m-1}(e_m\Delta\hat{\varepsilon}^*e_2),\quad \chi^{b,a}_{m,m+1}=q_{m+1}(e_2\Delta\hat{\varepsilon}^*e_{m+1}),$$
$$\chi^{b,a}_{m,m-1}=q_{m-1}(e_2\Delta\hat{\varepsilon}^*e_{m-1}),\quad \chi^{b,b}_{m,m+1}=q_{m+1}(e_2\Delta\hat{\varepsilon}e_2),$$

where k_m is the wave vector of the mth-order ($m=0,\pm1,\pm2,\ldots$) diffracted wave, G_m is the gyration vector,[11] $q_m=\omega_m/2e\sqrt{\varepsilon}\cos\varphi_m$ [ω_m is the frequency of the diffracted wave, φ_m is the angle of diffraction, $\overline{\varepsilon}=(1/3)Sp\hat{\varepsilon}$], and $\delta_m=|k_{mz}-k_{m+1,z}|$ is the detuning of the phase matching. The solution of system (1) should be sought using the boundary conditions: $A_0(0)=A_\parallel$, $B_0(0)=A_\perp$, $A_m(0)=B_m(0)$ for $m\neq 0$, where $A_\perp(A_\parallel)$ is the amplitude of the s-(p-)polarized incident light wave. The relative intensity η_m is given by $\eta_m=(|A_m|^2+|B_m|^2)/(|A_\parallel|^2)+|A_\perp|^2)$.

The system (1) was solved numerically for four diffraction orders when optical radiation with the wavelengths $\lambda_0=0.4416\mu$m, $\lambda_0=0.6328\mu$m, and $\lambda_0=1.06\mu$m is diffracted by an ultrasonic shear wave propagating along the [110] crystallographic axis and polarized along the [110] axis of a paratellurite crystal. The dimensions of the acoustooptic cell corresponded to the dimensions given in Ref. 2 and the specific rotation parameter of TeO_2 was $\rho=20$ deg/mm ($\lambda_0=1.06\mu$m, Ref. 11).

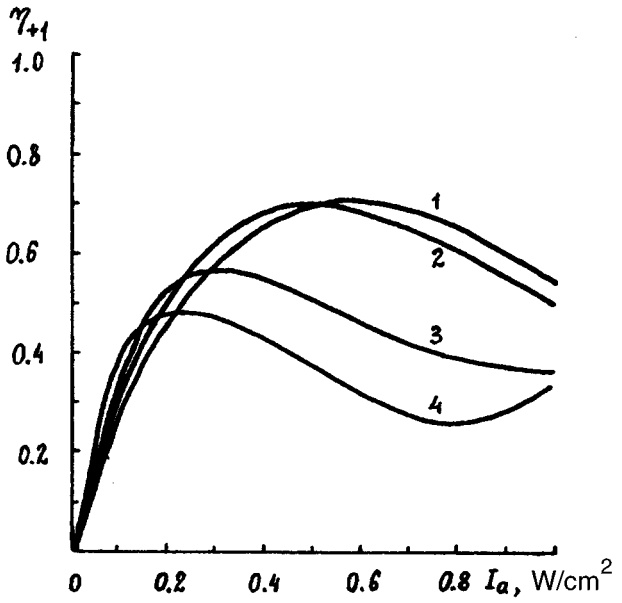

FIG. 2. Relative intensity η_{+1} versus ultrasonic wave intensity I_a for various acoustooptic interaction lengths l: *1* — 1.15 cm, *2* — 1.2 cm, *3* — 1.4 cm, and *4* — 1.6 cm ($I_a=0.25$ W/cm^2, $A_\parallel=1$, $A_\perp=0$, and $\Delta f=-8$ MHz).

The expression $\delta_0=\pi\lambda_0 f_0\Delta f/nv^2$ (Δf is the detuning of the ultrasound frequency from the Bragg frequency f_0) from Ref. 6 was used to investigate the amplitude–frequency characteristics of an acoustooptic light wave modulator-deflector at the wavelength $\lambda_0=1.06$ μm. Figure 1 gives η_{+1} as a function of the detuning parameter Δf for various ultrasonic wave intensities I_a. The central frequency of the ultrasonic wave source was $f_0=28$ MHz. It can be seen that the results of the numerical calculations (curve *3*) agree well with the experimental results presented in Ref. 2. The following characteristics of acoustooptic diffraction are observed: at the center of the amplitude–frequency characteristic the diffraction efficiency is negligible, the right and left sections are asymmetric, and the maxima of η_{+1} are achieved at frequencies f differing from the central frequency f_0. Figure 2 gives the relative intensity η_{+1} as a function of the ultrasonic wave intensity I_a for various acoustooptic interaction lengths l. It can be seen from Figs. 1 and 2 that Bragg diffraction can only be achieved when the interaction length, ultrasound intensity, and frequency detuning parameter are optimized. For light waves in the visible ($\lambda_0=0.6328$ μm) and ultraviolet ($\lambda_0=0.4416\mu$m) the dependences of η_{+1} on Δf and I_a are similar to those plotted in Figs. 1 and 2.

[1] V. V. Lemanov and O. V. Shakin, Fiz. Tverd. Tela (Leningrad) **14**, 229 (1972) [Sov. Phys. Solid State **14**, 184 (1972)].
[2] A. W. Werner, D. L. White and W. A. Bonner, J. Appl. Phys. **43**, 4489 (1972).
[3] I. Yano, M. Kawabuchi, A. Fukumoto,and A. Watanabe, Appl. Phys. Lett. **26**, 689 (1975).
[4] V. N. Belyĭ and G. V. Kulak, Opt. Spektrosk. **75**, 105 (1993) [Opt. Spectrosc. **75**, 63 (1993)].
[5] V. M. Kotov, Zh. Tekh. Fiz. **66**(1), 151 (1996) [Tech. Phys. **41**, 78 (1996)].
[6] V. I. Balakshiĭ, V. N. Parygin, and L. E. Churkov, *Physical Principles of Acoustooptics* [in Russian], Moscow (1985).

[7] V. I. Balakshiĭ and T. G. Kulish, Opt. Spektrosk. **80**, 294 (1996) [Opt. Spectrosc. **80**, 258 (1996)].
[8] B. V. Bokut', A. N. Serdyukov, and F. I. Fedorov, Kristallografiya **15**, 1002 (1970) [Sov. J. Crystallogr. **15**, 871 (1970)].
[9] F. I. Fedorov, *The Theory of Gyrotropy* [in Russian], Minsk (1976).
[10] G. V. Kulak, Opt. Spektrosk **79**, 662 (1995) [Opt. Spectrosc. **79**, 610 (1995)].
[11] V. A. Kizel' and V. I. Burkov, *Gyrotropy of Crystals* [in Russian], Moscow (1980).

Translated by R. M. Durham

Reconstruction of the mass distribution of charged particles in a periodic electric field

Yu. K. Golikov and E. Yu. Flegontova

St. Petersburg State Technical University
(Submitted October 1, 1996)
Pis'ma Zh. Tekh. Fiz. **23**, 1–7 (January 26, 1997)

A method is proposed for determining the mass spectrum of a monochromatic precisely directed source by means of a plane- parallel capacitor with a sinusoidally time-dependent voltage on the plates. The mass spectrum is reconstructed from an integral equation that relates the current to the collector with the amplitude of the ac part of the voltage. [S1063-7850(97)01601-7]

It is well known that the trajectories of charged particles in electric fields do not depend on the mass, and for this reason electric fields are employed in mass analyzers only of the time-of-flight type (see, e.g., Ref. 1). By creating a time-varying field (varying slowly enough so that electromagnetic effects can be neglected) one can mass-separate the flux in space (as was done, for example, in Ref. 2 for pulsed sources synchronized with the field). The integrated nature of the mass analysis method proposed in this paper makes it possible to analyze sources that are not synchronized with the time-varying field (in this particular case a steady-state source) since the analysis takes into account all the trajectories of particles emanating from the source at different instants of time. The simplest and most easily implemented field structure is used (the field of a parallel plate capacitor) along with a very simple time dependences (sinusoidal voltage on the plates). The integral nature of the method, as mentioned above, implies from a mathematical point of view the solution of an integral equation relating the mass spectrum with the dependence of the current to the collector on the ratio of the ac and dc components of the voltage on the plates. The simplicity of this system enabled us to solve this integral equation in quadratures and propose algorithms for reconstructing the mass distribution function in the source.

Let us consider the sinusoidally time-varying electric field of a parallel plate capacitor

$$\Phi = \Phi_0(1+\alpha \sin 2\pi\nu t), \tag{1}$$

where ν is the frequency and t is the time. We assume that a steady-state point source of charged particles is located in the plane of the lower electrode, with the particles emanating from the source with a given initial energy and direction of velocity. We choose a coordinate system such that the X axis coincides with the lower electrode and the Y axis is antiparallel to the field lines. At the point X_s on the X axis we place a collector of finite width along the Y axis. This system may be two-dimensional or axially symmetric (see Fig. 1).

The distribution function at the instant of emission from the source does not depend on the time t_0 of emission, but the trajectories of the particles oscillate depending on t_0 within limits determined by the amplitude of oscillation of the voltage and the mass of the particle. Particles with a mass greater than some threshold value strike the collector regardless of the phase of emission, while the only light particles that strike the collector are those that leave the source in a specific time interval that depends on the mass m and the ratio α of the ac to the dc components of the field. The current to the collector averaged over one period depends on α and is given by the instantaneous value of the current at each point integrated over the collector. This dependence also is an integral equation for the unknown mass spectrum.

Let us write the equation for the charged particle current through a plane perpendicular to the X axis:

$$j(X,Y,t) = \int_0^\infty dm \int_{-\infty}^{t} dt_0 \int_0^\infty dX \int_{-\infty}^{\infty} d\dot{Y}\dot{X} f(m,X,Y,\dot{X},\dot{Y},t,t_0), \tag{2}$$

where $f(m,X,Y,\dot{X},\dot{Y},t,t_0)$, the total distribution function of the particles, satisfies the equation of continuity (see Ref. 3) with the initial condition

$$\begin{aligned} f(m,X,Y,\dot{X},\dot{Y},t)|_{t=t_0} &= f_0(X,Y,\dot{X},\dot{Y}) \\ &= g(m)\,\delta(X-X_0)\,\delta(Y-Y_0) \\ &\times \delta\left(m\frac{\dot{X}^2+\dot{Y}^2}{2}-\varepsilon_0\right) \\ &\times \delta\left(\tan^{-1}\frac{\dot{Y}}{\dot{X}}-\vartheta_0\right), \end{aligned} \tag{3}$$

where $g(m)$ is the mass distribution to be determined, ϑ_0 is the angle of emission, ε_0 is the initial energy and $\delta(\cdot)$ is the Dirac delta function.

It is assumed that the characteristics of the equation of continuity, ψ_1,ψ_2,ψ_3 and ψ_4 are known functions of $m,X,Y,\dot{X},\dot{Y},t$, and t_0. The distribution function is expressed in terms of the characteristics and the initial condition in the following way:[3]

$$f(m,X,Y,\dot{X},\dot{Y},t,t_0) = f_0(m,\psi_1,\psi_2,\psi_3,\psi_4). \tag{4}$$

Substituting Eq. (4) into (3), integrating the current density over the collector, averaging the current to the collector over a period, and changing the order of integration (all the integrals depend uniformly and continuously on the parameters), we obtain

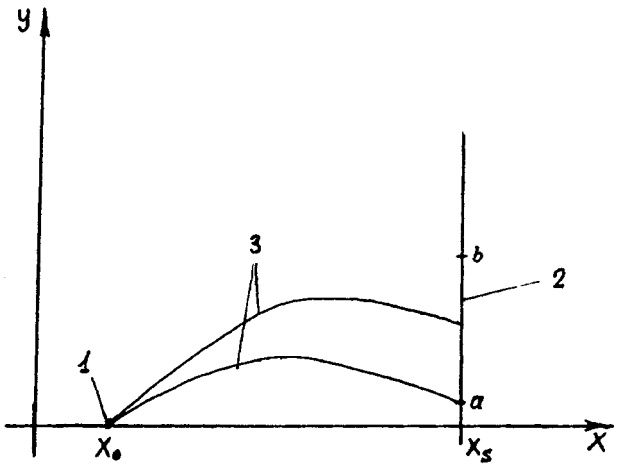

FIG. 1. Coordinate system and cross section of the electrodes: *1* — source, *2* — collector, *3* — particle trajectories.

$$I(X_s,\alpha)=\nu\int_0^\infty dm\int_0^{1/\nu}dt\int_a^h dY\int_{-\infty}^t dt_0\int_0^\infty d\dot{X}\times\int_{-\infty}^\infty d\dot{Y}\dot{X}f_0(m,\psi_1,\psi_2,\psi_3,\psi_4). \tag{5}$$

Equation (5) is the starting equation for the reconstruction of the mass spectrum. In order to find its explicit form we integrate the equations of motion.

Before integrating the equations of motion it is useful to transform to a dimensionless physical model following the scheme in Ref. 4. In dimensionless coordinates the equations are simplified and the interdependence among the various parameters becomes more transparent. As the unit of length we choose the distance L between the plates and go over to the dimensionless coordinates x and y and the dimensionless time τ:

$$x=X/L,\quad y=Y/L,\quad \tau=t/T, \tag{6}$$

where T is a scale factor defined by the condition

$$mL^2/T_2=q\Phi_0, \tag{7}$$

and q is the charge of a particle (the equality of the factors multiplying the ''kinetic'' and ''potential'' terms in the Lagrangian). The dimensionless and actual velocities and the energy are related in the following way:

$$\dot{x}=\frac{dx}{d\tau}=\sqrt{\frac{m}{q\Phi_0}}\frac{dX}{dt},\quad \dot{y}=\frac{dy}{d\tau}=\sqrt{\frac{m}{q\Phi_0}}\frac{dY}{dt}, \tag{8}$$

$$\varepsilon=m\frac{\dot{X}^2+\dot{Y}^2}{2}=\frac{mL^2}{T^2}\frac{\dot{x}^2+\dot{y}^2}{2}=\frac{mL^2}{T^2}W=q\Phi_0 W. \tag{9}$$

Here E and W are, respectively, the actual and the dimensionless energy. It can be seen that the unit of energy in this model is the energy of a particle passing through the characteristic potential Φ_0.

We now introduce the dimensionless parameter defining the actual mass m in fractions of some characteristic mass m_0:

$$\mu=m/m_0,\quad m_0=q\Phi_0/4\pi^2\nu^2L^2. \tag{10}$$

Finding in dimensionless coordinates the characteristics, φ_1, φ_2, φ_3, and φ_4, we obtain a new form of Eq. (5)

$$N(x)=\frac{1}{4\pi^2\nu I}\int_0^\infty G\mu d\mu\int_0^{2\pi\sqrt{\mu}}d\tau\int_{a/L}^{b/L}dy\int_{-\infty}^{\tau}d\tau_0\times\int_0^\infty\frac{2\pi\nu}{\sqrt{\mu}}\dot{x}\,d\dot{x}\int_{-\infty}^\infty d\dot{y}\,\delta(\varphi_1-x_0)\,\delta(\varphi_2-y_0)\times\delta\left(\frac{\varphi_3^2+\varphi_4^2}{2}-W_0\right)\delta\left(\tan^{-1}\frac{\varphi_4}{\varphi_3}-\vartheta_0\right). \tag{11}$$

Here

$$G(\mu)=g(m(\mu)),\quad N(x)=I(X(x)), \tag{12}$$

and x_s is a parameter, the dimensionless coordinate of the collector, which for brevity will be dropped from the formulas.

Carrying out the inner integral, we can convert Eq. (11) to the form

$$N(\alpha)=\frac{\dot{x}_0}{2\pi}\int_0^\alpha v(s)4\arcsin\frac{s}{\alpha}ds+\dot{x}_0\int_\alpha^\infty v(s)ds, \tag{13}$$

where

$$s=h\mu\Bigg/\sqrt{\left(1-\cos\sqrt{\mu}\frac{x_s-x_0}{\dot{x}}\right)^2+\left(\sqrt{\mu}\,\frac{x_s-x_0}{\dot{x}}-\sin\sqrt{\mu}\,\frac{x_s-x_0}{\dot{x}}\right)^2},$$

$$v(s)ds=\frac{G(\mu)}{\mu}d\mu. \tag{14}$$

Differentiating Eq. (13) with respect to the upper limit and making an elementary transformation, we obtain the Shlömilch equation

$$P(\alpha)=\int_0^\alpha w(s)\frac{1}{\sqrt{\alpha^2-s^2}}ds, \tag{15}$$

where

$$sv(s)=w(s),\quad \frac{\pi\alpha}{2x_0}\frac{dN(\alpha)}{d\alpha}=P(\alpha), \tag{16}$$

for which the formula for the inverse transformation is known.[5] Performing the inversion, we find the function $v(s)$:

$$v(s)=\frac{2}{\pi}\int_0^s\frac{P'(\xi)}{\sqrt{s^2-\xi^2}}d\xi. \tag{17}$$

Substituting this expression into Eq. (14), we find $G(\mu)$. Then we can transform again to dimensional mass and determine $g(m)$ by formula (12).

A computer implementation of this calculation using formula (17) for an actual mass spectrum of the integrated current to the collector can be carried out by a variety of means. For example:

a) Direct calculation of $v(s)$ from the integral formula (17), in view of the improper nature of the integral, becomes possible for a numerical simulation if the singularities are removed by means of the obvious transformation

$$\int_0^s \frac{P'(\xi)}{\sqrt{s^2-\xi^2}}d\xi=\int_0^s \frac{P'(\xi)-P'(s)}{\sqrt{s^2-\xi^2}}d\xi+\frac{\pi}{2}P'(s). \quad (18)$$

b) It is possible to use any convenient approximation to the experimentally measured function $P'(\xi)$ in Eq. (17) that ensures calculation of $v(s)$ in a class of known functions. For example, in a trigonometric approximation to $P'(\xi)$ by a section of a Fourier series, we obtain the following representation for the required function $v(s)$

$$v(s)=\frac{2}{\pi}\sum_{n=0}^{N} C_n\int_0^s \frac{\cos n\pi\xi}{\sqrt{s^2-\xi^2}}d\xi=\sum_{n=0}^{N} C_nJ_0(n\pi s), \quad (19)$$

where C_n are the Fourier coefficients and $J_0(x)$ is the zero-order Bessel function.

c) Sometimes it is useful to use a polynomial approximation to $P'(\xi)$, in which case the calculational algorithm looks like

$$v(s)=\frac{2}{\pi}\sum_{n=0}^{N} d_n\int_0^s \frac{\xi^n}{\sqrt{s^2-\xi^2}}d\xi$$

$$=\frac{1}{\pi}\sum_{n=0}^{N} d_nB\left(\frac{n+1}{2},\frac{1}{2}\right)s^n, \quad (20)$$

where d_n are the coefficients of the polynomial representation and $B(\frac{n+1}{2},\frac{1}{2})$ is the beta function (see Ref. 6).

[1] A. A. Sysoev and M. S. Chupakhin, *Introduction to Mass Spectroscopy* [in Russian] (Atomizdat, Moscow, 1977).

[2] A. A. Matyshev, *Abstracts of the Russian Scientific-Technical Conference ''Innovative Science-Oriented Technology for Russia,''* April 24–27, 1995, Part 9, St. Petersburg, 1995.

[3] Ya. B. Zel'dovich and A. D. Myshkis, *Elements of Mathematical Physics* [in Russian] (Nauka, Moscow, 1973).

[4] Yu. K. Golikov *et al.*, *Calculation of the Elements of Electrostatic Electron Optics Systems* [in Russian] (Leningrad Polytechnic Institute, Leningrad, 1984).

[5] G. N. Watson *Treatise on the Theory of Bessel Functions*, 2nd edition, (Cambridge University Press, Cambridge, 1952) [Russ. transl. of 1st ed., IL, Moscow, 1949].

[6] I. S. Gradshteyn and I. M. Ryzhik, *Tables of Integrals, Series, and Products*, transl. of 4th Russ. ed. (Academic Press, New York, 1980) [Russ. original 5th ed., Nauka, Moscow, 1971].

Translated by J. R. Anderson

Propagation of shear waves in a magnetic liquid with frozen-in magnetization

V. V. Sokolov and V. V. Tolmachev

Moscow State Academy of Instrument Making and Information Science, N. É. Bauman Moscow State Technical University

(Submitted August 12, 1996)
Pis'ma Zh. Tekh. Fiz. **22**, 88–91 (December 26, 1996)

[S1063-7850(96)04012-8]

In Ref. 1 the equations of ferrohydrodynamics of a nonconducting ideal magnetic liquid, possessing magnetization frozen into the material of the liquid, were derived with the aid of a generalized principle of virtual work. A linear approximation of these equations made it possible to describe satisfactorily the experimental results on the anisotropy of the propagation velocity of ultrasound in a magnetic liquid in a static magnetic field and to predict the existence of a new magnetohydrodynamic mode — Alfvén-type waves. Just as in magnetohydrodynamics, this wave is transverse, but in this wave the magnetization and not the magnetic field intensity oscillates. In Ref. 2 the equations of ferrohydrodynamics of a nonconducting magnetic liquid were generalized taking account of dissipation effects due to thermal conductivity, viscosity, and the finiteness of the time τ^* for establishing an equilibrium value of the magnetic field intensity.

In the present Letter the properties of the predicted new magnetohydrodynamic mode are discussed in detail and the conditions under which this mode can be observed experimentally are determined.

Consider an infinite plane ($z>0$), bounding an incompressible, nonconducting, magnetic liquid that oscillates sinusoidally along the y axis with frequency ω. A static, external, uniform magnetic field H, directed along the z axis, is applied to the liquid. Let the temperature of the liquid be constant. In accordance with Ref. 2, the initial system of equations for this problem assumes the form

$$\rho\frac{dv_i}{dt}=-\frac{\partial p}{\partial x_i}+(H_i^{eq}-H_i)\frac{\partial(\rho m_j)}{\partial x_j}+\rho m_j\frac{\partial H_i^{eq}}{\partial x_j}+\eta\nabla^2 v_i; \tag{1}$$

$$\frac{\partial(\rho v_j)}{\partial x_j}=0; \quad p=\left(\frac{\partial f}{\partial\rho}\right)_{T,m}; \quad H_i^{eq}=\left(\frac{\partial f}{\partial m_i}\right)_{\rho,T};$$

$$\rho\frac{dm_i}{dt}=\rho m_i\frac{\partial v_i}{\partial x_j}+\frac{H_i^{eq}-H_i}{\tau}; \quad H_i=-\frac{\partial\psi}{\partial x_i};$$

$$\nabla^2\psi=4\pi\frac{\partial(\rho m_i)}{\partial x_j}.$$

The specific free energy f of the magnetic liquid is assumed to be a known function of the density ρ of the liquid, the temperature T, and the components m_i of the vector of the specific magnetization density.

We confine our attention to a linear approximation of the system presented above. We give the velocity of the oscillations of points in the plane in the form $v_y(z=0)=v_0\exp(-i\omega t)$ and $v_x(z=0)=v_z(z=0)=0$. From the symmetry of the problem we can see that $v_x(z)=0$, $m_x=m_y=0$, and $m_z=m_0$ and from the boundary conditions and the first equation of the system it follows that $v_z(z)=0$. We take account of the perturbation introduced by the shear wave by representing the free energy by the expression

$$f(\rho,T,m_i)=f_0(\rho_0,T_0,m_{i0})+\left(\frac{\partial f}{\partial m_i}\right)_{\rho,T}m_i'.$$

Then the perturbation of the equilibrium magnetic field intensity is related linearly with the perturbation of the specific magnetization $h_i^{eq}=\beta_{ij}m_j'$. We assume that the tensor

$$\beta_{ij}=\left(\frac{\partial^2 f}{\partial m_i\partial m_j}\right)_0$$

is diagonal with components $\beta_{xx}=\beta_{yy}=\beta_\perp$ and $\beta_{zz}=\beta_\parallel$.

As a result, the linear approximation of the initial system assumes the form

$$\frac{\partial v_y}{\partial t}=m_0\beta_\perp\frac{\partial H_y^{eq}}{\partial z}+\nu\frac{\partial^2 v_y}{\partial z^2};$$

$$\frac{\partial m_y}{\partial t}=m_0\frac{\partial v_y}{\partial z}-\frac{\beta_\perp}{\rho\tau^*}m_y;$$

$$\frac{\partial m_z}{\partial t}=\frac{\beta_\parallel}{\rho\tau^*}m_z. \tag{2}$$

Here $\nu=\eta/\rho$ is the kinematic viscosity. The last equation in the system (2) splits off and its solution is written in the form $m_z=m_0\exp(-\beta_\parallel/\rho\tau^* t)$.

A solution in the form of a damped shear wave for the two remaining equations of the system (2) leads to the following expressions for the propagation velocity

$$c=\sqrt{\frac{2(A^2+B^2)}{B+\sqrt{A^2+B^2}}} \tag{3}$$

and the absorption coefficient for the modified shear wave under study

$$\alpha=\frac{Ac\omega^2}{2(A^2+B^2)}, \tag{4}$$

where

$$A=\frac{m_0^2\beta_\perp\omega\tau}{1+\omega^2\tau^2}+\frac{c_s^2}{2}, \quad B=\frac{m_0^2\beta_\perp\omega^2\tau^2}{1+\omega^2\tau^2}, \quad \tau=\tau^*\rho/\beta_\perp.$$

 1063-7850/97/010005-02$10.00

In the case $m_0=0$ the expressions (3) and (4) pass into the well-known formulas for the propagation velocity $c_s=\sqrt{2\mu\omega}$ and the absorption coefficient $\alpha_s=\sqrt{\omega/2\nu}$ of shear waves in a standard viscous liquid. The other limiting case, corresponding to the absence of viscosity, $\eta=0$, describes a damped purely Alfvén wave, whose propagation velocity and absorption coefficient are given by the relations

$$c=\sqrt{\frac{2m_0^2\beta_\perp\omega\tau}{\omega\tau+\sqrt{1+\omega^2\tau^2}}},\qquad(5)$$
$$\alpha=(m_0\tau\sqrt{2\beta_\perp(1+\sqrt{1+\omega^2\tau^2})})^{-1}\sqrt{\omega\tau},$$

respectively. In the case of an ideal magnetic liquid with a frozen-in magnetization it follows from Eq. (5) that $c=m_0\sqrt{\beta_\perp}$. This result was obtained previously in Ref. 1.

It follows directly from the formulas (3) and (4) derived above that it is difficult to observe an Alfvén-type wave in a magnetic liquid with frozen-in magnetization, since it is masked by a shear wave and possesses a high absorption coefficient.

To determine the conditions under which it can be observed experimentally, we shall examine the frequency dependence of the velocity and the absorption for two cases.

Let $\omega\tau\gg1$ and $\omega\gg\rho\omega_0^2\beta_\perp/\eta$. Then from Eq. (3) follows $c=c_s$ and from Eq. (4) $\alpha=\alpha_s$. Therefore it is impossible to observe an Alfvén-type wave for these high frequencies, since the ordinary shear wave plays the determining role.

In the case $\omega\tau\ll1$ and $\tau^*\gg\eta(\rho m_0)^2$ we obtain $c=m_0\sqrt{2\rho\tau^*\omega}$ and $\alpha=\omega/c$. Therefore an Alfvén wave should be observed in this frequency range. Let us estimate the applicability of our approximation for the following typical values of the parameters of magnetic liquids: $\rho=1$ g/cm^3, $m_0=10$ G·cm^3/g, and $\eta=5$ cp, so that $\eta/(\rho m_0)^2=5\times10^{-4}$. Therefore if $\tau^*\gg10^{-3}$, then one of the conditions of our approximation is satisfied. Unfortunately, there are no published data on the value of τ^*. To satisfy the other condition, $\omega\tau\ll1$, the measurements must be performed in the infrasonic range.

[1] V. V. Sokolov and V. V. Tolmachov in *Sev. Int. Conf. on Magnetic Fluids*, Bhavnagar, India, 1995, pp. 194–195.
[2] V. V. Sokolov and V. V. Tolmachev in *14th Int. Riga Conf. on Magnetohydrodynamics*, Jurmala, Latvia, 1995, p. 168.

Translated by M. E. Alferieff

Modulational instability of electromagnetic waves in long Josephson junctions

F. Kh. Abdullaev

Physicotechnical Institute, Academy of Sciences of the Republic of Uzbekistan
(Submitted August 5, 1996)
Pis'ma Zh. Tekh. Fiz. **23**, 8–11 (January 26, 1997)

This paper examines the modulational instability of electromagnetic waves in long Josephson junctions under conditions where the electrodynamics of the junction are nonlocal. A region is found containing a modulational instability of nonlinear plane electromagnetic waves in the junction. © *1997 American Institute of Physics.* [S1063-7850(97)01701-1]

A great deal of attention has recently been focused on the phenomenon of modulational instability of waves in nonlinear media.[1,2] Examples are the modulational instability of electromagnetic waves in optical fibers, which is described by an instability in the solution of the nonlinear Schrödinger equation,[2] and in long Josephson junctions in connection with an instability in the solution of the sine-Gordon equation.[3,4] In addition to the theoretical interest, the phenomenon of modulational instability has a number of practical applications. It is used, in particular, for generating trains of ultrashort optical pulses with a high repetition rate[2] and for the development of logical devices.[5]

In many situations study of the modulational instability requires consideration of nonlocal modifications of the nonlinear Schrödinger equation and the sine-Gordon equation.[6,7] Specifically, in long Josephson junctions, when the electromagnetic wave is much shorter than the Josephson penetration depth λ_J and when $\lambda_J<\lambda$, where λ is the London penetration depth, the electrodynamics of the junction becomes nonlocal. The equation for the phase difference $\varphi(x,t)$ has the form of nonlocal sine-Gordon equation[7]

$$\varphi_{tt}=\frac{\lambda_J^2}{\pi\lambda}\int_{-\infty}^{\infty}K_0(|x-y|)\varphi_{yy}dy-\sin\varphi, \tag{1}$$

where $K_0(x)$ is the zero-order Macdonald function. This equation is not integrable. It is equivalent to the sine-Gordon equation with all the higher even partial derivatives with respect to the spatial variable x.

The purpose of this work was to study the modulational instability of small-amplitude electromagnetic waves in long Josephson junctions. We consider the evolution of nonlinear oscillations of small-amplitude waves (breather type waves) in the junction. We write the field φ in the form

$$\varphi=e^{i\Omega t}v^*(x,t)+e^{-i\Omega t}v(x,t). \tag{2}$$

Expanding $\sin(x)$ in a series and retaining terms up to and including the third order in the field, and setting

$$\Omega^2=1,\quad t=t/4,\quad \alpha=\frac{2\lambda_J^2}{\pi\lambda^2},$$

we obtain the equation

$$iu_t+\alpha\int_{-\infty}^{\infty}K_0(|x-y|)u_{yy}dy+|u|^2u=0. \tag{3}$$

This is the nonlocal nonlinear Schrödinger equation.

Let us consider the modulational instability of the solution in the form of a nonlinear plane wave $u_0=A\exp(iA^2t)$. We shall seek a solution in the form

$$u=[A+\psi(x,t)]\exp\{iA^2t\}. \tag{4}$$

This gives us an equation for the correction $\psi(x,t)$:

$$i\psi_t+\alpha\int_{-\infty}^{\infty}K_0(|x-y|)\psi_{yy}dy+A^2(\psi+\psi^*)=0. \tag{5}$$

Setting $\psi=v+iW$ we obtain from Eq. (5) the system of equations

$$\begin{aligned} &v_t+\alpha\int_{-\infty}^{\infty}K_0(|x-y|)w_{yy}dy=0,\\ &-w_t+\alpha\int_{-\infty}^{\infty}K_0(|x-y|)v_{yy}dy+2A^2v=0. \end{aligned} \tag{6}$$

Carrying out the Fourier transformation in Eqs. (6), we find for the Fourier components $\overline{v(k,t)}$

$$\overline{v_{tt}}(k)+\overline{\alpha K_0}(k)k^2(\alpha K_0(k)k^2-2A^2)\overline{v(k)}=0. \tag{7}$$

We obtain as a result the following dispersion relation

$$\Omega^2=\frac{\alpha\pi k^2}{\sqrt{1+k^2}}\left(\alpha\frac{\pi k^2}{\sqrt{1+k^2}}-2A^2\right). \tag{8}$$

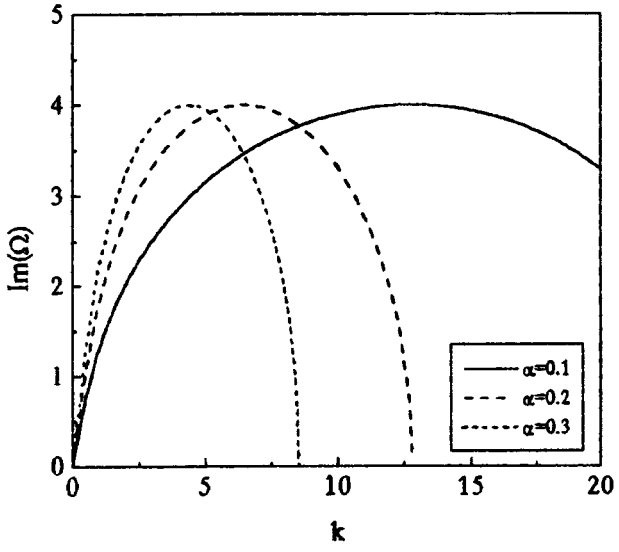

FIG. 1.

The plane wave becomes unstable when $\Omega^2<0$. We thus arrive at the condition that modulations of nonlinear electromagnetic plane waves are unstable when the wave numbers k are less than a critical value k_c

$$k_c^2=\frac{2A^4}{\alpha^2\pi^2}(1+\sqrt{1+\alpha^2\pi^2/A^4}). \tag{9}$$

Figure 1 shows the region of modulational instability for $A=1$ and $\alpha=0.1$, 0.2, and 0.3. Let us examine the value of k_c for various limiting cases:

a) taking $A^4/\alpha^2\pi^2\gg 1$, we find that $k_c=2\sqrt{2}A^2/\alpha\pi$.

b) taking $A^4/\alpha^2\pi^2\ll 1$, we find that $k_c=\sqrt{2}A/\sqrt{\alpha\pi}$.

The maximum gain is $g_m=\ \mathrm{Im}\,\Omega_m=A^2$, which is attained for modulations with the wave number $k_m\approx A^2/\alpha\pi$.

In summary, a region of modulational instability has been found for electromagnetic waves in long Josephson junctions. The modulated nonlinear plane plane wave in the development of a modulational instability will evolve into a train of pulses (small-amplitude breathers). The pulse repetition rate will depend on the modulation period of the initial wave $k<k_c$.

The modulational instability of large-amplitude waves in a nonlocal junction based on the nonlinear nonlocal sine-Gordon equation requires a separate treatment.

[1] V. I. Bespalov and V. I. Talanov, JETP Lett. **3**, 307 (1966).
[2] A. Hasegawa, Opt. Lett. **9**, 288 (1984).
[3] N. N. Akhmediev, V. M. Eleonskiĭ, and N. E. Kulagin, Izv. Vyssh. Uchebn. Zaved. Radiofiz. **31**, 244 (1988).
[4] N. M. Ercolani, M. G. Forest, and D. W. McLaughlin, Lett. Appl. Math. **23**, 149 (1986).
[5] M. Islam, *Ultrafast Optical Devices* (Oxford University Press, 1993).
[6] M. Alfimov, V. M. Eleonsky, and N. E. Kulagin, Chaos **2**, 454 (1992).
[7] A. Gurevich, Phys. Rev. B **46**, 3187 (1992).

Translated by J. R. Anderson

Acoustooptical processor for radio signals with discrete frequency modulation

N. A. Esepkina, A. P. Lavrov, and S. V. Dmitriev

St. Petersburg State Technical University
(Submitted November 18, 1996)
Pis'ma Zh. Tekh. Fiz. **23**, 12–19 (January 26, 1997)

A study is made of a processor for pulsed radio signals with discrete frequency modulation, where the frequency varies discontinuously within a pulse and takes on N different values. The spectral components are separated with an acoustooptic spectrum analyzer whose spectral plane is imaged onto a linear charged-coupled photodetector by means of a planar (one-dimensional) spatial converter made of optical fibers. In the imaging, the spectral components of the signal injected into the fiber are transposed by a special arrangement (permutation) of the fibers. The charge-coupled detector, which operates in the time-delay and accumulation mode, detects the spectral components and sums them with the required delay, and thereby compresses the signal and separates it from the noise. The compression factor is limited by the value of N and can be several hundred. Results of experimental investigations of a prototype of the processor are presented. [S1063-7850(97)01801-6]

1. Optical devices for processing radio signals by means of charge-coupled photodetectors have recently received a great deal of attention. With the use of modern basic elements (semiconductor lasers, broad-band acoustooptic modulators, multielement photodetectors) such devices provide characteristics superior to those of analogous electronic devices.[1] Additional possibilities of optical processors become evident when charge coupled photodetectors are used in the time delay and accumulation mode. This mode of operation allows the development of processors of the conveyor type, which are effective for the solution of various problems, such as constructing a radio image of the Earth's surface in synthetic-aperture systems (see Refs. 2, 3, and others). Previously we have demonstrated the possibility[4] of using these time-delay and accumulation devices for making adaptive acoustooptic processors for radio signals with linear frequency modulation.

In this paper we examine this type of acoustooptic processor for processing radio signals with discrete frequency modulation. Such signals are widely used in various measurement and communication systems. The change in the type of modulation (discrete in place of linear) has required that an additional element be introduced into the design of the processor — a fiber-optic converter.

2. A description of signals with discrete frequency modulation can be found in Ref. 5. We shall consider a signal with discrete frequency modulation as a collection of N sequential abutting elementary (partial) signals — simple radio pulses:

$$U_{\text{in}}(t)=\sum_{i=0}^{N-1} U_0 \cos[2\pi(f_d+\gamma_i\Delta f)t]\cdot \text{rect}\left(\frac{t}{\tau}-\frac{1}{2}-i\right), \tag{1}$$

where $\text{rect}(x)$ is defined in the following way: it equals unity if $|x|\leqslant 1/2$ and 0 if $|x|>1/2$; the quantity U_0 is the amplitude of an elementary signal, τ is its length, $f_i=f_d+\gamma_i\Delta f$ is the frequency of the ith elementary signal, f_d is the lower frequency of the signal, Δf is the discrete change in the frequency, $\{\gamma_i\}$ is the frequency-code sequence that defines the order of the time variation of the frequency in the signal. The frequency-code sequence $\{\gamma_i\}$ has a length N $(i=0,1,\ \ldots\ ,N-1)$ and represents a sequence of N distinct whole numbers in the range from 0 to $N-1$, whose order is defined by a special rule[5] and to an outside observer seems to be random. The partial signals occupy a collection of N neighboring channels over the spectrum with a total frequency band $N\Delta f$.

3. The structural design of the acoustooptic processor for processing signals with discrete frequency modulation is shown in Fig. 1. Its basic elements are *1* — a laser, *2* — a beam expander-shaper, *3* — an acoustooptic modulator, *4* — a Fourier-transforming lens, *5* — a fiber-optic converter, *6* — a linear charge-coupled photodetector, and *7* — a controller for the latter.

The principle of operation of this processor is as follows. The acoustooptic modulator with the Fourier lens carries out a spectral analysis of the radio signal incident on the acoustooptic modulator.[1] The intensity distribution of the diffracted light at the focal plane of the lens corresponds to the power spectrum of the radio signal. Consequently, when a signal with discrete frequency modulation is incident on the modulator at the focal plane of the lens (along the X_1 axis), a diffraction spot is formed that jumps about discontinuously in accordance with the changes in the frequency of the incident signal. The discrete locations of the centers of the spots are given by $X_{1i}=kf_i$, where k is a coefficient of proportionality determined by the optical elements of the acoustooptic spectrum analyzer. Figure 2a shows an example of the location of a diffracted spot in the focal plane of the processor for a signal with a short $(N=5)$ frequency-code sequence, $\gamma_i=3, 0, 2, 4, 1$, and the corresponding frequency-time representation of this signal.

A new element is included at the focal plane of the lens in this acoustooptic processor — a fiber-optic converter in the form of a single-layer flat bundle of optical fibers all of the same length. The number of fibers in the bundle is equal

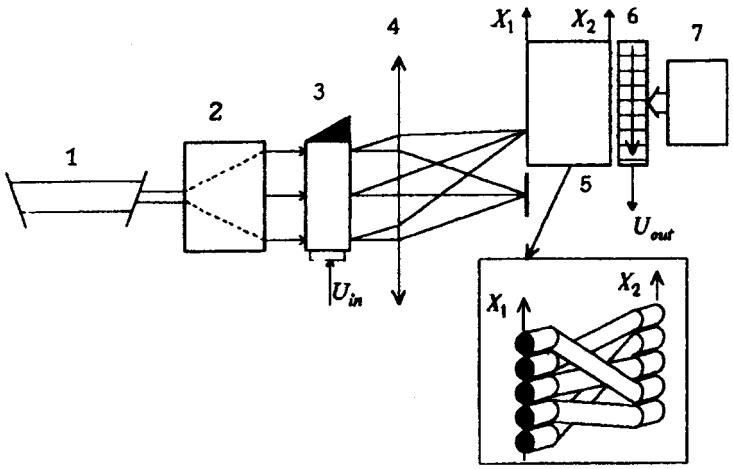

FIG. 1. Diagram of the acoustooptic processor for signals with discrete frequency modulation (*1* — laser, *2* — beam expander-shaper, *3* — acoustooptic modulator, *4* — Fourier-transforming lens, *5* — fiber-optic converter, *6* — linear charge-coupled photodetector, *7* — photodetector controller.

to the number of discrete frequency values in the signal with discrete frequency modulation; i.e., it is equal to N. The fiber-optic converter transmits the image with an intensity I_1 from its entrance plane to the output plane onto a discrete number of spots of dimension S corresponding to the diameter of the fiber core. In this processor the converter images the focal plane (along the X_1 axis, spots with centers at the points X_{1i}) onto the plane of the charge-coupled photodetector (along the X_2 axis). The input image is averaged within the confines of the spots. In addition to imaging, the fiber-optic converter also carries out a spatial conversion. This occurs by virtue of the transposition of the fibers in the output plane (Fig. 1). The transposition follows the frequency-coding by the sequence of the processed signal according to a simple rule: the spot labeled γ_i along the X_1 axis is imaged on the spot with the label i along the X_2 axis. The intensities I_1 and I_2 at the entrance and exit, respectively, of the fiber are thus related as $I_{2i}=I_{1\gamma_i}$.

When this converter is used in the processor the spectral components of a signal with discrete frequency modulation, separated by means of the acoustooptic spectrum analyzer, are introduced into the corresponding fiber through the end and are transmitted to the plane of the photodetector, illuminating the exit ends along the X_2 axis one after the other (Fig. 2b). In this way the light spot is transported from the illuminated end along the photodetector with an average velocity $V_s=\Delta x/\tau$.

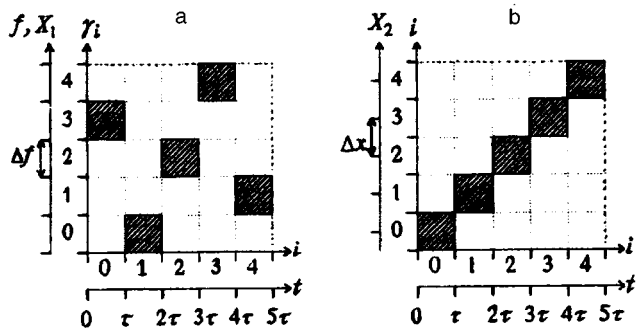

FIG. 2. Change with time of the signal frequency with discrete frequency modulation and the positions of the center of the diffraction spot at the entrance to the fiber-optic converter (a) and at the exit from the converter (b).

The photodetector in the processor operates in the time delay and accumulation mode. In this mode of operation its elements are shifted from one end to the other by a continuous chain (a conveyor) with the elements simultaneously carrying out spatial discretization and detection of the optical signal and accumulating it in the form of charge packets.[6] In the output unit these packets are converted into an output voltage U_{out}. In the time delay and accumulation mode the output voltage is

$$U_{\text{out}}(t)=\sum_{i=0}^{N-1} I_{2i}(t-(N-1)\Delta x/V_e), \tag{2}$$

where I_{2i} is the light intensity at the exit from the fiber-optic converter in the ith fiber (proportional to the power of the ith component of the signal) while V_e is the rate of motion of the elements of the photodetector: $V_e=l_eF$, where l_e is the spacing of the elements and F is the clock frequency applied to the photodetector from the controller (Fig. 1).

When V_s and V_e are equal, the output signal is

$$U_{\text{out}}(t)=\sum_{i=0}^{N-1} I_{2i}(t-(N-1)\tau), \tag{3}$$

i.e., the partial responses of all the frequency channels are detected and summed with the required delay. Thus a short video pulse is formed at the output with an amplitude proportional to the signal energy and a duration τ_c close to the duration of an elementary signal. Hence this processor compresses a signal with discrete frequency modulation and detects it. The instant of arrival of the signal is irrelevant to this processor.

The compression factor obtained in this processor, $K=N\tau/\tau_c$ is not greater than N and is limited by the baseline of the acoustooptic modulator and the number of elements of the photodetector. Presently existing element baselines permit a value $K_{\max}\approx 10^3$, which is much greater than in electronic processors based on a set of band-pass filters.[5] Because of the finite speed of the detector the duration of the

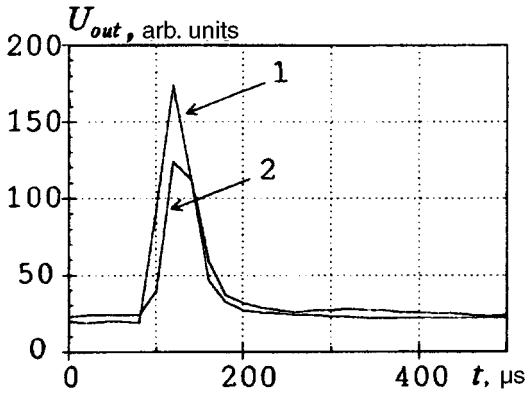

FIG. 3. Output signal of the acoustooptic processor for different signals with discrete frequency modulation. Curve *1* — Frequency code sequence of the signal matches the fiber-optic converter; curve *2* — the frequency-code sequence of the signal has been changed.

compressed signal is limited from below to a value $\tau_{c\min} \approx 0.1-0.2$ μs. To process signals with different frequency-code sequences it is necessary to replace the fiber-optic converter.

4. A laboratory prototype of an acoustooptic modulator was made using an acoustooptic modulator based on a TeO_2 crystal with a time aperture of 10 μs and a 500 element linear photodetector of the type FPZS-1L. The fiber-optic converter (the fiber bundle) consisted of 16 fibers with a core diameter of 100 μm and a distance of 140 μm between centers at the entrance and exit planes, and corresponded to a signal with a frequency-code sequence $\gamma_i = 7, 2, 8, 12, 1, 4, 9, 13, 0, 5, 10, 14, 3, 6, 11, 15$. The signal with discrete frequency modulation was formed by means of a voltage-controlled oscillator. The duration τ of an elementary signal was 20 μs, and the duration of the entire signal was 320 μs. An IBM-type PC was used to control the oscillator and record the output signal from the processor.

Various experiments were carried out with the prototype. As an example, Fig. 3 shows output signals obtained from the acoustooptic processor when signals with different frequency-code sequences were fed into it. Curve *1* corresponds to a signal matched with the arrangement of the fibers in the bundle, and curve *2* corresponds to a signal with a different frequency-code sequence (6 of the 16 signals are transposed in time). As one can see from this figure, when the frequency-code sequence is changed the amplitude is reduced by about 35%, which agrees with the calculations, while the dc component of the output signal is increased. The duration of the output signal is somewhat greater than the expected 30 μs.

The appropriate software must be developed to investigate the characteristics of the processor and for simulating its operation.

In summary, the results show that when acoustooptic techniques are used for separating the frequency components of a radio signal, along with a fiber-optic converter and a charge-coupled photodetector operated in the delay and accumulation mode, it is possible to make an acoustooptic processor that compresses radio signals having discrete-frequency modulation. Such a processor may find use in various radio electronic systems.

[1] O. B. Gusev, S. V. Kulakov, B. P. Razzhivin, and D. V. Tigin, *Optical Signal Processing in Real Time* [in Russian] (Radio i Svyaz', Moscow, 1989).
[2] D. Psaltis, Proc. IEEE **72**, 962 (1984).
[3] N. A. Esepkina, G. A. Gavrilov, A. P. Lavrov *et al.*, Pis'ma Zh. Tekh. Fiz. **18**(3), 32 (1992) [Sov. Tech. Phys. Lett. **18**, 72 (1992)].
[4] N. A. Esepkina, A. P. Lavrov, and M. N. Anan'ev, Izv. Vyssh. Uchebn. Zaved. Radioelektron. **33**(8), 51 (1990).
[5] L. E. Varakin, *Communication Systems with Noise-Like Signals* [in Russian] (Radio i Svyaz', Moscow, 1985).
[6] D. F. Barb, in *Solid State Imaging*, NATO Advanced Study Institute Series E, No. 16, ed. by P. G. Jespers, F. van der Wiele, and M. F. White, (Noordhoff, Leyden, 1976) [Russ. transl., Mir, Moscow, 1979].

Translated by J. R. Anderson

Dynamics of dislocations and disclinations of the field of a few-order optical fiber: I. Creation and annihilation of $C^{\pm}$ disclinations

A. V. Volyar and T. A. Fadeeva

Simferopol State University
(Submitted November 11, 1996)
Pis'ma Zh. Tekh. Fiz. **23**, 20–27 (January 26, 1997)

It is shown experimentally and theoretically that the interconversion dynamics of the field of the LP_{11} mode combination of a few-mode optical fiber is determined by the interaction of circularly polarized pure edge C^+ and C^- disclinations. The C^+ and C^- disclinations correspond to characteristics of the field for which the right- or left-circularly polarized electric field goes to zero. During propagation the uniformly linear-polarized dislocations D_y break down into four C^+ disclinations travelling in opposite senses. When each pair of C^- and C^+ disclinations meet they annihilate each other and form linear polarization. The field of the linearly polarized disclinations thus created sums up out of phase into the original field and forms a uniformly linearly polarized field with D_x dislocations. © *1997 American Institute of Physics.* [S1063-7850(97)01901-0]

In the propagation of light waves through an optical fiber interference-induced exchange of energy occurs between the fields of the natural modes having similar values of the propagation constant β. These field conversions are well illustrated in the example of the LP_{11} mode. This mode is four-fold degenerate — twofold in the parity and twofold in the polarization, and is a combination of an even or odd He_{21} mode and TM_{01} or TE_{01} eigenmodes, having identical propagation constants $\tilde{\beta}$ in the scalar approximation of the wave equation. In the first approximation of the vector wave function each of the eigenmodes obtains an additional polarization correction $\Delta\beta$ to the propagation constant.[1] This correction $\Delta\beta$ lifts the degeneracy of the LP_{11} mode and causes polarization conversions in the distributions of the transverse electric and magnetic fields.

We have shown in Ref. 2 that the field of the eigenmodes of an optical fiber includes optical vortices (screw dislocations), by means of which one can describe perturbations of the fields in the optical fiber. However, for a complete description of the evolution of the LP_{11} wave field it is still not enough to use only optical vortices. It is necessary to expand the classification schemes of scalar dislocations. In describing the evolution of a microwave vector field in free space Ney and Hajnel[3,4] introduced the concept of vector dislocations, calling them disclinations of the electromagnetic field and requiring that both the E_x and the E_y components of the field vanish in the vicinity of the disclination.

The purpose of this work was to study the interconversion of dislocations and disclinations of the field of the LP_{11} mode of a few-mode optical fiber.

1. The studies were made on the even $LP_{11x}^{(e)}$ mode linearly polarized in the plane $z=0$, with the assumption that these results can also be reproduced for the other three LP_{11} modes.

The field of the $LP_{11x}^{(e)}$ mode for a centrosymmetric medium can be written as[1]

$$e_t(LP_{11x}^{(e)}) = E_0\{\hat{x}\cos(\varphi)\cos(\delta\beta z) + i\hat{y}\sin(\varphi)\sin(\delta\beta z)\}F_1(R)\exp(i\tilde{\beta}z), \quad (1)$$

where $\hat{x}$ and $\hat{y}$ are the polarization unit vectors, φ and R are the azimuthal and radial coordinates, $\delta\beta$ is the half-difference in the polarization corrections of the TM_{01} and $He_{21}^{(e)}$ eigenmodes, $F_1(R)$ is the radial distribution function of the electric field: $F_1(R)=RF_1'(R)$ (Ref. 2).

Expression (1) shows that the field of the $LP_{11x}^{(e)}$ mode contains two pure edge dislocations.[3] In general the transverse mode, expression (1), is nonuniformly polarized and it cannot be described by means of dislocations of a scalar field.

Let us write expression (1) in the circular polarization basis $(\hat{e}^+, \hat{e}^-)$:

$$e=[\hat{e}^+\cos(\delta\beta z-\varphi)+\hat{e}^-\cos(\delta\beta z+\varphi)] \times F_1(R)\exp(i\tilde{\beta}z). \quad (2)$$

We require that the amplitude of the field vanish for right-circular polarization $\hat{e}^+$ or left-circular polarization $\hat{e}^-$. This requirement is expressed by the equations

$$\varphi=\pm\pi/2+\delta\beta z, \ \text{(a)} \quad \varphi=\pm\pi/2-\delta\beta z, \ \text{(b)} \quad (3)$$

where $\hat{e}^+=0$ for expression (a) and $\hat{e}^-=0$ for expression (b).

Equations (3) describe the motion of two circularly polarized parts of the field of the LP_{11} mode with variation in the longitudinal z coordinate. Following Ref. 4, we shall define a circular disclination C^+ as the state of the field for which the amplitude of its left-circular component vanishes $(\mathrm{Im}\,e^-=\mathrm{Re}\,e^-=0)$, and the disclination C^- as the state of the field for which the amplitude of the right-circular component vanishes $(\mathrm{Im}\,e^+=\mathrm{Re}\,e^+=0)$.

Then the dynamics of propagation and interaction of the C^+ and C^- disclinations can be represented in terms of the distribution of the intensity $I(\rho,\varphi)$ and the eccentricity

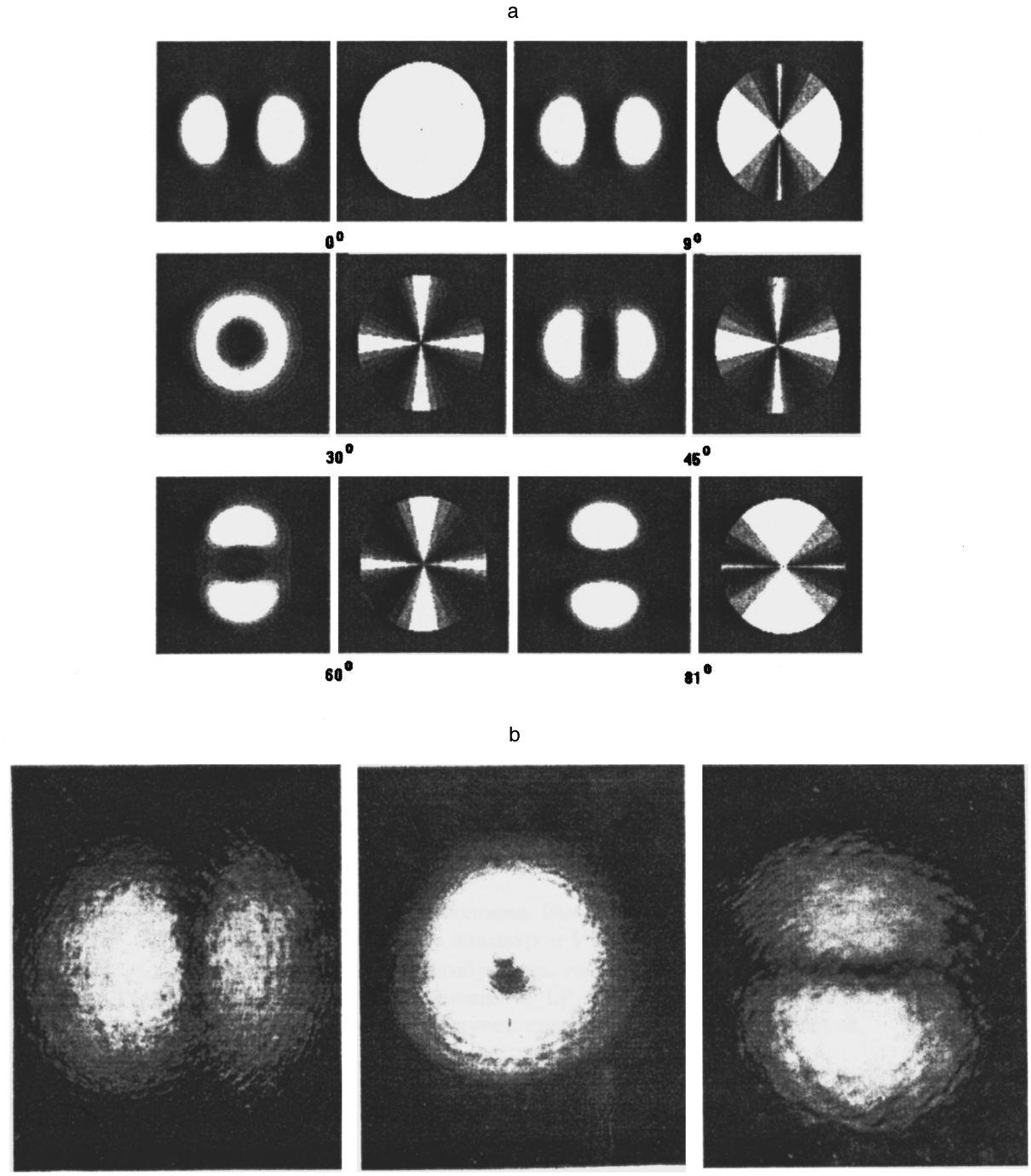

FIG. 1. (a) — Distributions of the intensity and eccentricity modulus of the LP_{11} mode for various cross sections $\Phi-\delta\beta z$ of the fiber (the dark regions indicate the circular polarization and the light regions the linear polarization); (b) — photographs of the distribution of the radiation field of the LP_{11} mode for the lengths $z=3.6$ m, 0.5 m, and 0.9 m.

$Q(\varphi)$ of the field of the LP_{11} mode (Fig. 1a). It can be seen from this figure that the pure edge C^+ and C^- disclinations are created from an $\hat{x}$-polarized dislocation D_x. Simultaneously an immobile L_y disclination is created. This disclination is linearly polarized along the y axis. The C^+ and C^- disclinations move oppositely to one another and annihilate at $\varphi=\pi/2$ and $3\pi/2$, creating an L_x disclination. The field of the created L_x disclination is polarized in antiphase to the field polarized along the x direction and lying on the axes $\varphi=\pi/2$ and $3\pi/2$. Therefore these two fields add and form a D_y dislocation with uniform polarization along the y axis. These processes can be represented as

$$D_x \rightarrow C^+ + C^- + L_y, \quad C^+ + C^- + L_x \rightarrow D_y. \tag{4}$$

Ordinarily the processes of creation and annihilation of field dislocations are represented by the curves $\mathrm{Re}\,E=0$ and $\mathrm{Im}\,E=0$ (Ref. 7) plotted in the x, y coordinates. Therefore the phase portrait shown in Fig. 2a contains lines for which $e^+=0$ or $e^-=0$ in accordance with expression (3). In a polar coordinate system the radial coordinate represents the

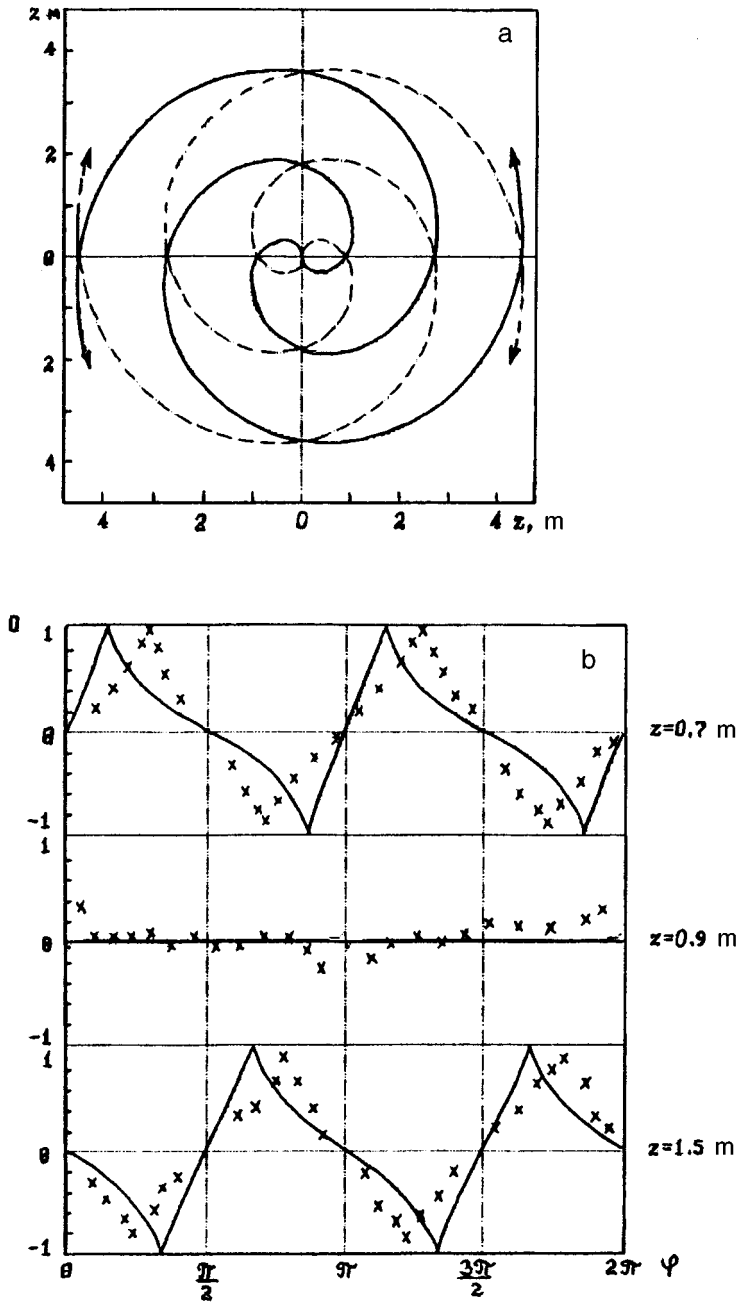

FIG. 2. a—Phase portrait of the creation and annihilation of C^+ and C^- disclinations; the dashed curve corresponds to C^+ disclinations and the solid curve to C^- disclinations; b — dependence of the eccentricity Q on the azimuthal coordinate φ at various lengths z along the fiber (the theoretical results are given by the solid line, and the experimental points by the crosses).

length z of a fiber, while the location of the axis of a disclination in the transverse cross section is represented by the azimuthal angle φ. The points of intersection of the curves correspond to a creation-annihilation event involving dislocations and disclinations.

2. To study experimentally the disclination dynamics we examined the distribution of the state of polarization of the radiation field in a few-mode optical fiber. We used a fiber with a radius $\rho = 3.5$ μm with a reduced diameter $V = 3.6$.

If this fiber is excited by a Gaussian beam of a TEM_{00} laser mode, then an HE_{11} mode is generated at the same time as the LP_{11} mode. The field of the HE_{11} mode does not have a singularity on the axis of the fiber, but the presence of this mode influences substantially the distribution and the number of dislocations of the field. To reduce the contribution of this mode the fiber can be excited with a TEM_{01} laser mode, or a holographic filter can be used. In addition, in order to excite only one of the LP_{11} modes and not a superposition of them, the linear polarization vector must be oriented parallel or perpendicular to the axis of the edge dislocation of the excitation field. In our experiment the fiber was excited by a holographic method by passing the excitation laser beam through the hologram of a pure edge dislocation. The length of the beats of the LP_{11} mode was $\Lambda = 2\pi/\delta\beta = 3.6$ m. To study the dependence of the eccentricity $Q = b/a$ on the length z_0 (here b and a are the semiminor and semimajor axes of the polarization ellipse) the fiber was broken off every $\Delta z_0 = 1$ cm and the Stokes parameter was measured.[6] The dependence of the eccentricity Q on the azimuthal coordinate φ for various lengths z_0 is shown in Fig. 2b. It is found that in parts of the radiation field symmetric about the z axis the circulations of the polarization states have opposite

signs. The azimuth of the inclination of the semimajor axis of the polarization ellipse makes an angle of either 0 or $\pi/2$ with the x axis, in agreement with the calculations. At the instant of annihilation of the circular disclinations the transverse radiation field is uniformly linearly polarized.

In Fig. 1b we show photographs of the fields corresponding to the lengths $z=2\pi/\delta\beta$, $\pi/(4\delta\beta)$, and $\pi/(2\delta\beta)$. The field in the first and third photographs corresponds to the pure edge dislocations D_y and D_x. The field shown in the second photograph resembles superficially a pure screw dislocation. However, the characteristic ''forked'' interference pattern cannot be obtained for arbitrary polarization of the reference beam. This is because the field in the transverse cross section is nonuniformly polarized: $e\sim\hat{x}X+\hat{y}Y$; i.e., it is a vector superposition of two pure edge dislocations.

To summarize, it has been shown both experimentally and model-theoretically that the propagation of the field of the LP_{11} mode is not a static wave process, but a dynamic sequence of creation and annihilation of dislocations and rotatary $C^{\pm}$ disclinations propagating along the axis of the fiber. The circularly polarized $C^{\pm}$ pure edge disclinations are created out of D_x dislocations; they move in opposite senses to one another with the same angular velocity and they annihilate to form D_y dislocations.

This work was partially supported by the International Soros Program for the support of higher education in the area of the exact sciences (ISSEP), Grant No. N PSU062108.

[1] A. W. Snyder and J. D. Love, *Optical Waveguide Theory* (Chapman and Hall, New York, 1983) [Russ. transl., Radio i Svyaz', Moscow, 1987].
[2] A. V. Volyar and T. A. Fadeeva, Pis'ma Zh. Tekh. Fiz. **22**(8), 63 (1996) [Tech. Phys. Lett. **22**, 333 (1996)].
[3] J. F. Nye, Proc. R. Soc. London Ser. A **387**, 105 (1983).
[4] J. V. Hajnal, Proc. R. Soc. London Ser. A **414**, 447 (1987).
[5] I. V. Basistiy, M. S. Soskin, and M. V. Vasnetsov, Opt. Commun. **103**, 422 (1993).
[6] A. V. Volyar, A. M. Bykov, and I. S. Volkov, [*sic*] Opt. Spektrosk. **61**, 190 (1986) [Opt. Spectrosc. (USSR) **61**, 123 (1986)].
[7] A. V. Ilyenkov, A. I. Khiznyak, and L. V. Kreminskaya, Appl. Phys. A **62**, 465 (1996).

Translated by J. R. Anderson

Laser control of the state of a plasma in a selective optical trap

A. P. Gavrilyuk, I. V. Krasnov, and N. Ya. Shaparev

Computation Center, Siberian Division of the Russian Academy of Sciences, Krasnoyarsk
(Submitted November 6, 1996)
Pis'ma Zh. Tekh. Fiz. **23**, 28–32 (January 26, 1997)

Laser cooling of resonant ions is shown to be applicable to the effective control of the temperature of charged particles in a low-temperature electron-ion plasma confined in a magnetic trap. [S1063-7850(97)02001-6]

A magnetooptical trap was proposed in Ref. 1 for an ultracold highly ionized charged plasma (with electron an ion temperatures T_e and $T_i<0.01$ eV). One of the main advantages of this optical confinement of a plasma is its selectivity: an ultrapure plasma with the ion component resonant with the laser radiation is accumulated in the trap and isolated from contact with walls. A natural consequence of this circumstance is the possibility of effective laser cooling of the plasma. It should be noted that despite the spectacular success in the use of laser cooling methods in fundamental physics experiments with atom and ion traps,[2,3] an electron plasma has never been considered a suitable candidate for these methods. We shall show that a combination of laser cooling of ions and high-frequency microwave heating of electrons under conditions of magnetooptical plasma confinement permits the state of the plasma to be controlled; i.e., it is possible to establish and maintain at will the electron and ion temperatures over a very wide range of possible values. We believe that this conclusion together with the idea of magnetooptical plasma confinement[1] opens up prospects for the creation of plasma devices of a new type, in which fairly weak electromagnetic radiation can fine-tune the main plasma parameters. The area of their application lies in the study of the fundamental properties and the possible applications of ultracold gas plasmas.

Let us consider a homogeneous completely ionized plasma confined in a magnetooptical trap[1] and subjected to a microwave field and uniformly irradiated with monochromatic light (in the form of a standing wave along the **n** direction with an amplitude $\mathbf{E}=\mathbf{E}_0\cos(k\mathbf{n}\cdot\mathbf{r})$) quasiresonant with a transition of the plasma ions and having a frequency ω shifted towards the red relative to the resonant frequency ω_{21}: $\omega-\omega_{21}=\Delta<0$. Then the ion is acted on by a frictional force, which in the case of a weak field ($|V|\ll\gamma$) and large detunings from resonance ($|\Delta|\gg\gamma, k\sqrt{T_i/m}$) can be written in the form[4]

$$\mathbf{F}=m\chi(\mathbf{v}\cdot\mathbf{n})\mathbf{n}, \tag{1}$$

where $\chi\simeq(\hbar k^2\gamma g/m\Delta)$ is the coefficient of friction ($\chi<0$), $g=|V/\Delta|^2$, V is the Rabi frequency ($V=dE_0/\hbar$), d is the dipole moment matrix element, γ is the rate of spontaneous decay of an excited ion, m is the ion mass, and **v** is the ion velocity. We assume that the ion plasma frequency is $\omega_i\ll\gamma$. From Eq. (1) we obtain the expression for the rate of change of the average ion kinetic energy ε_i resulting from laser cooling when the mean free path of the charged particles is short compared to the dimensions of the trap and the rate of cooling is low compared to the rate of ion–ion collisions

$$\left.\frac{\delta\varepsilon_i}{\delta t}\right|_c=\langle\mathbf{F}\cdot\mathbf{v}\rangle=\chi T_i, \tag{2}$$

where the angle brackets denote averaging over the equilibrium ion velocity distribution.

Because of the high frequency and relatively low intensity of the optical field under these conditions the direct action on the electrons by the optical field can be neglected. On the other hand, the slowing absorption of the microwave radiation with a frequency ω_h and intensity I in electron–ion collisions increases the electron kinetic energy ε_e. The rate of microwave heating of the electrons for $\omega_h\gg\nu_{ei}$ is[5,6]

$$\left.\frac{\delta\varepsilon_e}{\delta t}\right|_h=\frac{\mu I}{n}=(4\pi e^2/m_e c\omega_h^2)I\nu_{ei}, \tag{3}$$

where μ is the coefficient of slowing absorption, n is the density of charged particles, m_e is the electron mass, ν_{ei} is the effective rate of electron-ion collisions,[6] $\nu_{ei}=(4\sqrt{2\pi}/3)\times(e^4 n\ \ln\Lambda/m_e^{1/2}T_e^{3/2})$, and $\ln(\Lambda)$ is the Coulomb logarithm.

Taking into account relations (2) and (3) and the energy exchange between the electron and ion subsystems, we assume that the plasma lifetime τ in the trap[1] and the recombination lifetime τ_r are considerably longer than the characteristic collision time, $\sim\nu_{ei}^{-1}$ and the characteristic optical cooling time $|\chi^{-1}|$ (the condition that the plasma density is quasistationary), and write the energy balance equation for the charged particles

$$\frac{dT_e}{dt}=W_h(T_e,I)-\frac{4}{3}\,\nu_{ei}(T_e-T_i)\frac{m_e}{m},\quad W_h=\frac{2}{3}\cdot\left.\frac{\delta\varepsilon_i}{\delta t}\right|_h, \tag{4}$$

$$\frac{dT_i}{dt}=\frac{4}{3}\left\{\nu_{ei}(T_e-T_i)\frac{m_e}{m}+\frac{\chi}{2}\,T_i\right\}.$$

These equations differ from the standard equations describing nonresonant microwave heating in the second term on the right-hand side of the equation for the ion temperature—the term relating to the effect of laser cooling.

A qualitative analysis of the nonlinear autonomous system (4) in the phase plane shows that for $\chi(\Delta,V)<0$ it has a single stable stationary state (T_i,T_e). The steady-state temperatures satisfy the following relations

TABLE I. Characteristics of an ultracold plasma and their dependences on the intensity of the microwave field for fixed parameters of the optical field.

I, W/cm^2	10^{-2}	4×10^{-3}	10^{-3}	4×10^{-4}	10^{-4}
T_e, eV	5.7×10^{-2}	2.3×10^{-2}	5.7×10^{-3}	1.5×10^{-3}	6.0×10^{-4}
T_i, eV	6.5×10^{-5}	10^{-4}	2×10^{-4}	8×10^{-4}	6.0×10^{-4}
τ_r, s	2.1×10^{8}	3.5×10^{6}	6.6×10^{3}	16.0	0.26
τ_1, s	63	16.0	2.0	0.27	0.07

$$T_e - T_i = C_1 \cdot \frac{m}{m_e} \cdot \frac{I}{\omega_h^2}, \quad T_e^{3/2} T_i = C_1 \cdot C_2 \frac{\ln \Lambda n I}{\omega_h^2 |\chi|}, \qquad (5)$$

where C_1 and C_2 are a combination of physical constants: $C_1 = 3\pi e^2/m_e c$ and $C_2 = 8\sqrt{2\pi} e^4/3m_e^{1/2}$. It is readily seen from Eqs. (5) that by varying the intensity I of the microwave field, the intensity I_0, and the detuning of the optical field (which govern the coefficient of friction: $\chi \propto |V|^2/\Delta^3 \propto I_0/\Delta^3$), one can quite arbitrarily control the electron and ion temperatures.[1)] For $I \ll I_c = (C_2^{2/3}/C_1) \times (n/|\chi|)^{2/3} (m_e/m)^{5/3}$ the plasma is isothermal, $\theta = (T_e - T_i)/T_i \ll 1$:

$$T_i \simeq T_e \simeq (C_1 \cdot C_2 \cdot \ln \Lambda n I/\omega_h^2 |\chi|)^{2/5}. \qquad (6)$$

If $I > I_c$ the plasma is not isothermal, $\theta \sim 1$, while if $I \gg I_c$ it is highly nonisothermal, $\theta \gg 1$. The electron temperature is determined only by the microwave field, while the ion temperature (for fixed T_e) can be set by an appropriate selection of the parameters of the optical radiation (Δ, I_0)

$$T_e \simeq C_1 \frac{m}{m_e} \frac{I}{\omega_h^2}, \quad T_i \frac{\ln \Lambda \cdot n\omega_h}{|\chi| I^{1/2}} \left(\frac{m_e}{m_i}\right)^{2/3} \cdot \frac{C_2}{C_1^{1/2}}. \qquad (7)$$

A remarkable circumstance is that attaining and maintaining a given temperature in the ultracold plasma requires only fairly low intensities of the optical field I_0 and the microwave field I. In Table I we list the temperatures T_i and T_e and for comparison the characteristic recombination time τ_r and time τ_1 for establishing a quasi-steady state for $m = 100$ amu, $\gamma = 10^8$ s^{-1}, $k = 2\times10^5$ cm^{-1}, $I_0 = 0.1$ W/cm^2, $\Delta = 2\times10^9$ s^{-1} ($|\chi| = 21$ s^{-1}), $\omega_h = 10^{11}$ s^{-1}, and $n = 10^6$ cm^{-3}.

In conclusion we note that a plasma that is isolated from the walls, that is quasistationary, ultracold, in resonance with the optical radiation, and has *completely controllable parameters* may be a very convenient object for studying the collision of cold charged particles, highly nonisothermal plasma states ($\theta \gg 1$), the transition from a collisionless state to a collisional state with a reduction in the temperature T_e, the recombination of charged particles of a supercooled plasma,[7] and photoinduced collective phenomena in a plasma with resonant ions, and their spectroscopic manifestations.[8] A practical application of such a plasma may be to create a plasma source of ultrapure beams of ''cold'' ions.

This work was supported by the Russian Fund for Fundamental Research (Grant No. 95-02-04788).

[1)]For any selected pairs of values (T_e and T_i) with $T_e > T_i$ one can formally find a combination of parameters of the external fields $(I/\omega_h^2, I_0/\Delta^3)$ that satisfy Eqs. (5).

[1] A. P. Gavrilyuk, I. V. Krasnov, and N. Ya. Shaparev, JETP Lett. **63**, 324 (1996).
[2] P. E. Toshek, ''Atomic particles in traps,'' in *New Trends in Physics, Course 3*. Les Houches, eds. G. Grynberg and R. Slora (Elsevier, Amsterdam, 1984), Vol. 1, pp. 381–450.
[3] M. H. Anderson, J. R. Enser, M. R. Matthews *et al.*, Science **269**, 198 (1995).
[4] A. P. Kazantsev, G. I. Surdutovich, and V. P. Yakovlev, *The Mechanical Action of Light on Atoms* [in Russian] (Nauka, Moscow, 1987).
[5] Yu. P. Raĭzer, *The Physics of a Gaseous Discharge* [in Russian] (Nauka, Moscow, 1987).
[6] V. E. Golant, *Microwave Methods of Investigating Plasmas* [in Russian] (Nauka, Moscow, 1968).
[7] S. A. Maĭorov, A. N. Tkachev, and S. I. Yakovlenko, Usp. Fiz. Nauk **164**, 297 (1994) [Phys. Usp. **37**, 279 (1994)].
[8] I. V. Krasnov and N. Ya. Shaparev, Opt. Spektrosk. **80**, 577 (1996) [Opt. Spectrosc. **80**, 514 (1996)].

Translated by J. R. Anderson

Subhomogeneous spectroscopy of a Bose condensate of neutral atoms

I. E. Mazets and B. G. Matisov

A. F. Ioffe Physicotechnical Institute, Russian Academy of Sciences, St. Petersburg
St. Petersburg State Technical University
(Submitted November 21, 1996)
Pis'ma Zh. Tekh. Fiz. **23**, 33–38 (January 26, 1997)

A method is proposed for resolving experimentally the details of the resonant fluorescence spectrum of a Bose condensate within a homogeneous line whose width is greatly increased because of collective effects. A discussion is presented concerning the application of this method for determining the shifts of the resonant frequencies of the transitions in the condensate as compared to the usual case of nondegenerate atom ensembles. © *1997 American Institute of Physics.* [S1063-7850(97)02101-0]

An important advance in atomic physics of recent years has been the development of methods of vaporization cooling to the Bose-Einstein condensation point in alkali-metal vapors held in a magnetooptical trap.[1] For the first time it has appeared possible to study experimentally the properties of a Bose condensate of a nearly ideal gas, as opposed to the strongly interacting Bose systems associated with superfluidity and superconductivity. A number of articles, for example Refs. 2 and 3, have been published concerning the properties of such degenerate systems of neutral atoms. It has been pointed out[3] that the frequencies corresponding to resonant absorption of light in a Bose condensate are not known exactly. In fact, the transition frequencies must be shifted relative to those of the single atoms because of the small but nonetheless practically manifest van der Waals forces and because of the exchange of resonant photons. Measurement of these shifts would give important information on these interactions. Since a Bose condensate of neutral atoms is an only slightly nonideal system, experimental results and theoretical calculations can readily be compared directly. In our view this is of fundamental interest for modern quantum statistical physics.

However, there exists a substantial difficulty: the absorption line of a collection of a large number of identical atoms in the same quantum state is greatly broadened by collective effects.[3] The homogeneous line width of the permitted transitions in a Bose condensate under actual conditions is as much as tens of GHz. Therefore for an exact determination of the line shifts it is advisable to have available a method of subhomogeneous spectroscopy.

Such methods have been well developed for conventional spectroscopy over the last two decades. They are based on the phenomenon of coherent trapping of the population, involving the capture of atoms in a superposition of quantum states in which the atoms are not excited by resonant radiation because of destructive interference of the various excitation channels. The different aspects of this phenomenon have been thoroughly discussed in Ref. 4. Let us recall one particular aspect. The necessary conditions for achieving trapping by the action of two laser beams and resonant transitions from the two corresponding long-lived low-energy states into the same excited state are a) maximum mutual correlation of the fluctuations of the two laser beams or the use of highly stable lasers as in the experiment of Ref. 5; and b) satisfaction of the conditions for two-photon resonance — equal detunings of the two fields from the corresponding resonant frequencies. It is important to note that the width of the two-photon resonance is essentially the width of the Raman transition, which in the case of nonsaturating intensities of the laser radiation is much less than the inverse lifetime of the optically excited level used in this Raman transition. This circumstance also makes it possible to resolve the spectral features within a homogeneously broadened line.

Let us consider the Λ diagram of atomic levels, consisting of a low-energy ground state (g), a metastable state (m), and an optically excited level (e). The N atoms in the state g form a Bose condensate; i.e., the translational degrees of freedom of each atom are described by the wave function $|0\rangle$ of the lowest state of the harmonic oscillator potential of the trap. Two classical electromagnetic fields are applied to the system — a probe field P acting on the $g-e$ transition and a C (coupling) field, which couples the levels m and e. The Rabi frequency, which characterizes the $j-e$ field, and its wave vector are denoted respectively as V_j and k_j $(j=P,C)$. The detunings Ω_P and Ω_C (the frequency difference between the electromagnetic fields and the corresponding transitions) for fixed parameters of the laser radiation carry information on the shifts of the atomic levels under the conditions of Bose-Einstein condensation.

Let us write down the equations for the atomic field operators. These operators for the states where the condensation takes place are ordinarily[2,3] replaced by the c-numbers, $\sqrt{N}$. Then the following equations are valid for the annihilation operators $\hat{b}_e$ and $\hat{b}_m$ for atoms in the states $\exp(i\mathbf{k}_P\cdot\mathbf{r})|0\rangle\otimes|e\rangle$ and $\exp[i(\mathbf{k}_P-\mathbf{k}_C)\cdot\mathbf{r}]|0\rangle\otimes|m\rangle$, respectively

$$\frac{\partial}{\partial t}\hat{b}_e=-\Gamma\hat{b}_e+i\sqrt{N}V_p\exp(-i\Omega_P t)+iV_C\times\exp(-i\Omega_C t)\hat{b}_m, \tag{1}$$

$$\frac{\partial}{\partial t}\hat{b}_m=-\Gamma_m\hat{b}_m+iV_C^*\exp(i\Omega_C t)\hat{b}_e. \tag{2}$$

As pointed out above, because of collective effects in a Bose condensate the homogeneous width Γ of the $g-e$ transition

increases by several orders of magnitude compared to the ordinary radiative width γ of a transition in an isolated atom.[3] In this collective decay, the atoms return from the excited state to the condensate, and photons are emitted in a narrow solid angle $f \approx (k_P l)^{-2}$ in the direction $\mathbf{k}_P$. Here l is the rms spread in the coordinates of the atoms in the state $|0\rangle$. The collective decay constant was calculated in Ref. 3: $\Gamma = N\gamma f$. The ordinary incoherent decay of the excited state, although it does not contribute very much to the broadening, is important experimentally because it is accompanied by the emission of photons in all directions relative to the axis of the laser beam and therein lies the possibility of observing resonant fluorescence, whose intensity is proportional to $\langle \hat{b}_e^\dagger \hat{b}_e \rangle$. In addition, the population of the excited state can be assessed by scattering from the system an auxiliary light beam resonant with the transition from the e state to the second excited state e'.

We note that incoherent spontaneous decay in the channel $e-m$ has little effect on the population of the translational motion part of the state $\exp[i(\mathbf{k}_P - \mathbf{k}_C)\cdot \mathbf{r}]|0\rangle \otimes |m\rangle$.

The different relaxation processes that are characteristic of the metastable state are taken into account by introducing the decay constant Γ_m. It is clear that $\Gamma_m \ll \Gamma$. The $g-m$ transition is forbidden, and the presence of the condensate in the ground state cannot break this inequality. It should be noted that Γ_m should also include terms determined by fluctuations in the laser fields.[6] In investigating the Bose condensate we shall not impose such rigid limits on the stability of the lasers as are common in atomic beams or gas cells. Indeed, even if the rays P and C are obtained from independent sources with band widths of the order of several MHz, the corresponding contribution to Γ_m is three or four orders of magnitude smaller than Γ.

Let us now find the steady-state solution to the system (1) and (2). These equations yield an expression for the average number of excited atoms:

$$\langle \hat{b}_e^\dagger \hat{b}_e \rangle = \frac{N|V_P|^2}{I^2+\Omega_P^2} \cdot \frac{I_m^2 + (\Omega_P - Q_C)^2}{W_{bl}^2 + (\Omega_P - \Omega_C)^2}, \tag{3}$$

where

$$W_{bl} = \Gamma_m + \frac{|V_C|^2 \Gamma}{\Gamma^2 + \Omega_P^2}. \tag{4}$$

In the derivation of Eq. (3) we used the condition $I_m^2 \ll W_{bl}\Gamma$. Let us assume that the intensity of the field coupling the levels m and e lies in the range corresponding to the case $\Gamma_m \ll W_{bl} \ll \Gamma$. Then, as one can see from the solution (3), the resonant fluorescence spectrum will contain a subhomogeneous structure. In fact, if the field of the probe field is scanned relative to the frequency of the field C a narrow valley of width W_{bl} (a so-called ''black line'') will appear against the background of a Lorentz line shape of width Γ, the line being deeper the smaller the ratio Γ_m / W_{bl}. The dependence of the intensity of the resonant fluorescence on the detuning of the two fields is entirely analogous to the dependence associated with coherent population trapping in nondegenerate atomic ensembles.[4] Estimates show that attainment of a ratio $W_{bl}/\Gamma \sim 10^{-2}$ is an entirely realistic possibility. Simultaneously with the decrease in the number of atoms in excited states, the population of the metastable level

$$\langle \hat{b}_m^\dagger \hat{b}_m \rangle = \frac{N|V_P|^2}{\Gamma^2 + \Omega_P^2} \cdot \frac{|V_C|^2}{W_{bl}^2 + (\Omega_P - \Omega_C)^2} \tag{5}$$

increases in the vicinity of the black line.

The appearance of subhomogeneous structure in the resonant fluorescence spectrum can be given the following interpretation: destructive interference occurs in the scattering of the probe beam by the two dressed states formed in the mixing of the excited and metastable states by the field C. The half-widths of these two states are Γ and W_{bl}, respectively. Scattering of photons of the probe mode by these states is coherent, and at Raman resonance $\Omega_P - \Omega_C = 0$ the amplitudes of the two processes sum together, resulting in nearly zero value. We can conclude that the situation we have analyzed for the Bose condensate is closest to the coherent population trapping in double radiooptical resonance for nondegenerate atoms.[7]

Comparing the frequencies of the fields P and C for which the black line appears in the spectrum [Eq. (3)] with the frequencies corresponding to coherent population trapping in a nondegenerate atomic ensemble (for example, with the results of the experiment[5] on ^{87}Rb), one can find the difference in the shifts due to collective interactions of the $g-e$ and $m-e$ transition energies.

[1] M. H. Anderson, J. R. Ensher, M. R. Matthews *et al.*, Science **269**, 198 (1995); C. C. Bradley, C. A. Sackett, J. J. Tollett *et al.*, Phys. Rev. Lett. **75**, 1687 (1995); K. B. Davis, M. O. Mewes, M. R. Adams *et al.*, Phys. Rev. Lett. **75**, 3969 (1995).

[2] B. V. Svistunov and G. V. Shlyapnikov, Zh. Éksp. Teor. Fiz. **98**, 129 (1990) [Sov. Phys. JETP **71**, 71 (1990)].

[3] J. Javanainen, Phys. Rev. Lett. **72**, 2375 (1994); Phys. Rev. Lett. **75**, 1927 (1995).

[4] B. D. Agap'ev, M. B. Gornyĭ, B. G. Matisov *et al.*, Usp. Fiz. Nauk **163**(9), 1 (1993) [Phys. Usp. **36**, 763 (1993)].

[5] A. M. Akul'shin, A. A. Celikov, and V. L. Velichansky, Opt. Commun. **84**, 139 (1991).

[6] B. J. Dalton and P. L. Knight, Opt. Commun. **42**, 411 (1982); J. Phys. B 15, 3997 (1982).

[7] E. A. Korsunskiĭ, B. G. Matisov, and Yu. V. Rozhdestvenskiĭ, Zh. Éksp. Teor. Fiz. **102**, 1096 (1992) [Sov. Phys. JETP **75**, 595 (1992)]; M. Löffler, D. E. Nikonov, O. A. Kocharovskaya *et al.*, in *'ICONO'95: Coherent Phenomena and Amplification without Inversion''*, ed. by A. V. Andreev, O. Kocharovakaya, and P. Mandel, Proc. SPIE **2798**, 317 (1996).

Translated by J. R. Anderson

Model of a quantum well rolled up into a cylinder and its application to the calculation of the energy structure of tubelene

L. A. Mel'nikov and A. V. Kurganov

Saratov State University
(Submitted November 19, 1996)
Pis'ma Zh. Tekh. Fiz. **23**, 39–45 (January 26, 1997)

A model is presented for a quantum well rolled up into a cylinder and is used to describe the electronic structure of tubular clusters of carbon and the systems formed by them. The energy levels of a tubulene molecule are calculated. The estimates of the ionization potential and the nature of the conduction this cluster derived within this model are in agreement with known data. © *1997 American Institute of Physics.* [S1063-7850(97)02201-5]

An approach to developing an adequate mathematical description of the properties of nano-size objects in order to solve a number of applied problems may be through the use of the elements of the theory of quantum wells developed in the context of semiconductor nanostructures.

In this paper we consider an an electron gas in a potential field in the shape of a quantum well rolled up into a cylinder. Such a system is a modification of the model of a quantum well spread out into a sphere proposed in Ref. 1 for the calculation of the electronic structure of fullerene. The main differences in the present problem stem from the cylindrical symmetry of the potential and the choice of approximations.

If electron–electron interactions are neglected, the stationary one-electron states of the system are described by the Schrödinger equation with the Hamiltonian

$$\hat{H}=-\frac{\hbar^2}{2m}\nabla^2+U(r), \tag{1}$$

where m is the electron mass, r is the distance reckoned from the axis of the well, and the potential $U(r)$ has the form of a square-well potential with a depth U_0 and a width d, rolled up into a cylinder of radius R

$$U(r)=\begin{cases} 0 & 0\leqslant r\leqslant R-d/2 \\ U_0 & R-d/2\leqslant r\leqslant R+d/2 \\ 0 & r>R+d/2 \end{cases}. \tag{2}$$

The motion of the electron in the radial direction corresponds to a set of discrete energy levels, by analogy with the quantization of the motion transverse to an ordinary quantum well. The orbital motion of revolution also has a discrete energy spectrum determined by the quantization of angular momentum. Along the axis of the rolled-up quantum well the electron moves freely. The energy scale for the radial motion is determined by the depth U_0 of the well. The orbital component of the energy is proportional to the square of the ratio between the electron angular momentum and the radius of its orbit. The energy of motion along the axis is given by the square of the z component of the electron momentum.

Exploiting the cylindrical symmetry of the problem, one can seek the electron wave function in the form

$$\Psi_{n,\nu,\beta}(r,\varphi,z,t)=AF_{n,\nu}(r)\exp(i\nu\varphi)\exp(i\beta z)\exp(-i\omega t), \tag{3}$$

where A is an amplitude factor, the function $F_{n,\nu}(r)$ describes the radial dependence, while the quantum numbers ν and β describe the angular and axial dependences, respectively. As a result the Schrödinger equation reduces to the well-known Bessel equation in the radial component $F_{n,\nu}(r)$, whose solutions are the cylindrical Bessel functions. Imposing the condition of continuity on the solutions and their first derivatives at the boundary of the well, we obtain an equation for the determination of the electron energy eigenvalues. The radial and orbital components of the energy are coupled through the centrifugal displacement of the electrons and form discrete levels of the radial-orbital energy. The electron kinetic energy is the sum

$$E=E_{n,\nu}+E_\beta \tag{4}$$

of the energies of the radial-orbital and the axial motions.

We shall now use the idea of an electron gas in the quantum well rolled into a cylinder to construct a simple model for a tubular carbon cluster. Such clusters are highly interesting not only because of their unique electrical and mechanical properties,[2] but also because of their prospects for applications in making flat-panel displays,[3] nano-size emitters,[4–6] high-temperature superconductors,[7] and for a new generation of scanning electron microscope tips.[4] The tubular structures similar to carbon structures can be formed from atoms of other elements.[8]

Let us consider a C_{60+18N} tubular cluster ($N\gg 1$), called tubelene,[9] whose structure has been established in experimental observations of the formation of nano-fiber structures by tubelene.[10] It is a cylindrical fragment of a graphite surface enclosed on both ends with hemispheres — halves of C_{60} fullerene.[10] Tubelene is an achiral tubular cluster of the ''zigzag'' type[9,11] and has a ninefold principal axis of symmetry. Its surface can be generated when a fragment consisting of two carbon atoms is repeated in space by the translation vectors $\mathbf{a}_1$ and $\mathbf{a}_2$ (Fig. 1). Tubelene can be considered a quasi-one-dimensional crystal formed by N ring-shaped cells of length a.

Strictly speaking, this model corresponds to the limiting case of C_{60+18N} tubelene of infinite length ($N\to\infty$). How-

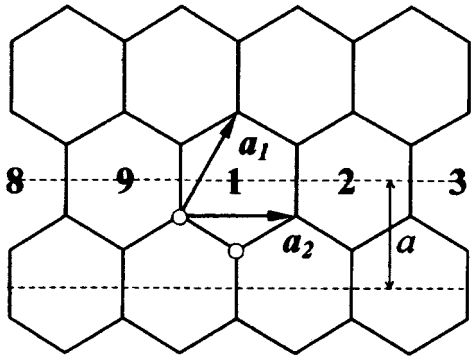

FIG. 1. A portion of the cylindrical surface of tubelene unrolled onto a plane. $\mathbf{a}_1$ and $\mathbf{a}_2$ are the primitive translation vectors of the two-dimensional Bravais lattice. $\mathbf{a}_1$ corresponds to translation along the helical chain of atoms and the vector $\mathbf{a}_2$ corresponds to turning by an angle $2\pi/9$ relative to the principal symmetry axis.

ever, because the ratio of the cluster length to its diameter is usually very great — 10^3 and greater — in the calculations relating to tubelene of this length we can regard the model as a first approximation and take the finite length into account by imposing certain conditions on the quantum number β of the wave function (3). In our model, it is additionally necessary to take into account the tubelene surface structure, which determines whether the conduction of the cluster is metallic or semiconducting.[11–13] We introduce periodic boundary conditions for the wave functions of the problem, assuming the periodicity unit is equal to the length L of the tubelene ($L=Na$). Then the quantum number β can assume the following series of values

$$\beta=0,\pm 2\pi/L,\pm 4\pi/L,\ldots,\pi/a. \tag{5}$$

The requirement that the wave function be periodic under a rotation by an angle of 2π about the main symmetry axis is satisfied by any integral values of the quantum number ν, which determines the number of angular nodes of the wave function. However, it is sensible to use only the states with angular momentum $\nu\leqslant 9$, since for $\nu>9$ the number of angular nodes becomes greater than the number of carbon atoms in the cross section of tubelene.

The structure of the ring-shaped fragments of tubelene has a large effect on the emission of electrons in an external field,[4] the growth of nanotubes, and other surface phenomena. Therefore in the calculation of the corresponding characteristics of tubelene it is necessary to take account of the electron states localized near its ends (Tamm states)[14,15] corresponding to the closed structure.

The parameters of the model for describing the energy structure of tubelene were selected in the following way. The diameter $2R$ of the quantum well rolled into a cylinder we set equal to the tubelene diameter, 0.71 nm (Ref. 16) while the depth U_0 and the width d of the potential enter as adjustable parameters. To determine these parameters we replaced the attractive potential of the carbon ion with a spherical square potential well. The ratio of its radius R_s to its depth U_s was chosen so that only two states reside in the well: one with an orbital quantum number $l=0$ and the other with $l=1$. In this model these states play the role of the $2s$ and $2p$ orbitals of the carbon atom. The values of R_s and U_s are chosen so that the model levels are situated at a depth corresponding to the ionization potentials I_{2s} and I_{2p} of the carbon atom. The wave functions of the model levels and the carbon levels have an equal number of zeros in the radial direction, as is required by the approximation of the linear combination of atomic orbitals.[1] In the construction of the quantum well its parameters were determined by the relations $U_0=U_s=27.6$ eV, $D=2R_s=0.35$ nm. This semiempirical approach yields good results even with the rather crude approximations used.

The results of a numerical solution to the characteristic equation for the electron are shown in Fig. 2 as an energy level diagram of the radial-orbital energies $E_{n,\nu}$ that correspond to the quantum numbers n and ν of the wave function (3) permitted by the structure of the tubelene surface. Each state is twofold degenerate in the spin quantum number. The

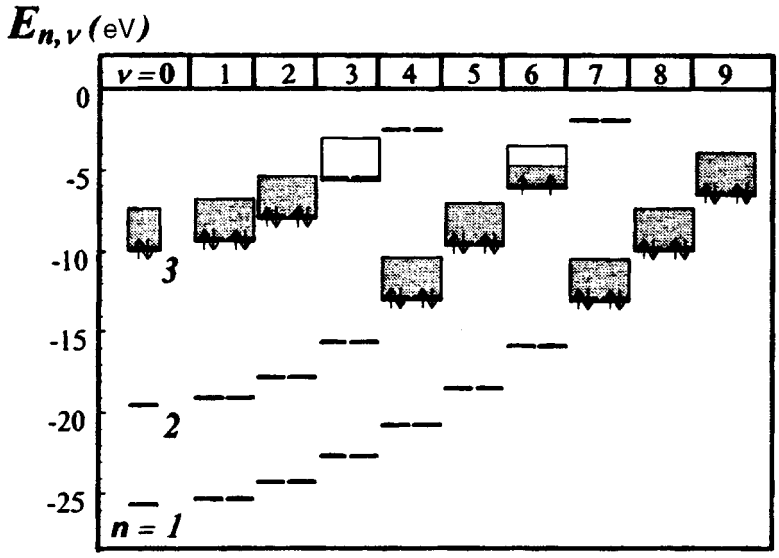

FIG. 2. Diagram of one-electron levels of the radial-orbital electron energy in a quantum well rolled into a cylinder. Each horizontal double dash indicates a state with two possible orientations of the electron spin. For the electrons filling the upper levels the mutual orientation of the spins is shown by the arrows. Also shown are the energy bands corresponding to the upper filled levels in tubelene — a quasi-one-dimensional crystal. The occupied sublevels of the bands are shaded.

states with nonzero ν, moreover, are again twofold degenerate in the two possible signs of ν. When the degeneracy is taken into account, the upper level is found to be only half filled. In tubelene considered as a quasi-one-dimensional crystal, the levels that are obtained are broadened into energy bands (Fig. 2) whose widths

$$E_\beta = \hbar^2 \beta^2 / 2m \tag{6}$$

are determined by the maximum values of β in the set given in Eq. (5). In the region of the upper filled level the electrons are redistributed between three energy bands, which as a result are only partly filled, which influences the metallic nature of the conduction. Our model gives 6.0 eV for the ionization potential of tubelene, which agrees with the results of band structure calculations of achiral tubular clusters with a similar surface structure and diameters close to that we selected for tubelene.[14,17,18]

In summary, the model of a quantum well rolled up into a cylinder, while not claiming to be an exact description of the electronic structure of tubular clusters, nonetheless yields estimates of the parameters of this object and reveals the regularities in the arrangement of the energy levels determined by the cylindrical symmetry and the dimensions of the system. This model is based on transparent approximations and does not require a great deal of computer time for the calculations. As a result, this model can be used to describe the tubular clusters formed in complex systems, such as multilayer clusters[2] or a fiber[10] of closely spaced single-layer clusters.[10] This description is equivalent to that of systems of two-dimensional quantum wells with an electron gas correspondingly embedded or rolled into a cylinder.

This work was carried out with the support of the Russian Fund for Fundamental Research (Grant No. 95-02-06445a).

[1] V. V. Rotkin and R. A. Suris, Fiz. Tverd. Tela (St. Petersburg) **36**, 3569 (1994) [Phys. Solid State **36**, 1899 (1994)].
[2] S. Ijima, Nature **354**, 56 (1991).
[3] L. Cowan and G. Smestad, OE Reports No. 147 (1996), pp. 2, 6.
[4] A. G. Rinzler, J. H. Hafner, P. Nikolaev *et al.*, Science **269**, 1550 (1995).
[5] W. A. de Heer, A. Chatelain, and D. Ugarte, Science **270**, 1179 (1995).
[6] L. A. Chernozatonskii, Yu. V. Gulyaev, Z. Ja. Kosakovskaja *et al.*, Chem. Phys. Lett. **233**, 63 (1995).
[7] K. Fossheim, E. D. Tuset, T. W. Ebbesen *et al.*, Physica C **248**, 195 (1995).
[8] R. Tenne, Adv. Mater. **7**, 965 (1995).
[9] L. A. Chernozatonskii, Phys. Lett. A **166**, 55 (1992).
[10] Z. Ya. Kosakovskaya, L. A. Chernozatonskiĭ, and E. A. Fedorov, JETP Lett. **56**, 26 (1992).
[11] R. Satio, M. Fujita, G. Dresselhaus, and M. S. Dresselhaus, Phys. Rev. B **46**, 1804 (1992).
[12] J. W. Mintmire, B. I. Dunlap, and C. T. White, Phys. Rev. Lett. **68**, 631 (1992).
[13] N. Hamada, S. Sawada, and A. Oshiyama, Phys. Rev. Lett. **68**, 1579 (1992).
[14] I. V. Stankevich and L. A. Chernozatonskiĭ, JETP Lett. **63**, 621 (1996).
[15] R. Tamura and M. Tsukada, Phys. Rev. B **52**, 6015 (1995).
[16] O. E. Omel'yanovskii, V. E. Tsebro, O. I. Lebedev *et al.*, JETP Lett. **62**, 483 (1995).
[17] X. Blase, L. X. Benedict, E. L. Shirley, and S. G. Louie, Phys. Rev. Lett. **72**, 1878 (1994).
[18] L. Lou, P. Nordlander, and R. E. Smalley, Phys. Rev. B **52**, 1429 (1995).

Translated by J. R. Anderson

Diffusion of promethium in silicon

D. É. Nazyrov, G. S. Kulikov, and R. Sh. Malkovich

M. Ulukbek Tashkent State University, A. F. Ioffe Physicotechnical Institute, Russian Academy of Sciences, St. Petersburg

(Submitted October 4, 1996)
Pis'ma Zh. Tekh. Fiz. **23**, 46–50 (January 26, 1997)

The first investigations have been made on the diffusion of promethium in silicon. In the temperature range from 1100 to 1250 °C the diffusion constant of promethium increases from $\sim 1\times 10^{-13}$ cm^2/s to $\sim 1.5\times 10^{-12}$ cm^2/s. The temperature dependence of the diffusion coefficient can be described by $\mathcal{D} = 5 \times 10^{-3}\exp[-(3.3\ \text{eV}/kT)]\text{cm}^2/\text{s}$. © *1997 American Institute of Physics.* [S1063-7850(97)02301-X]

One of the principal ways of enhancing the reliability of semiconductor devices, particularly for use in extremal conditions, is to create semiconductor materials that are stable against thermal and radiation influences. Recently, in a number of investigations inside and outside of Russia it has been established that the thermal and radiation stability of silicon, which is the main material of present-day semiconductor microelectronics, can frequently be greatly enhanced by introducing rare-earth elements into it.[1–3] The results of these and other investigations have served to stimulate a great deal of interest in doping silicon with rare-earth elements and also to motivate studies of the behavior of these impurities in silicon and their effect on the physical and physicochemical properties of the material.

In this paper we present the results of the first investigations of the diffusion of promethium in silicon.

For studying the diffusion we used plane-parallel polished wafers of *n*-type KÉF-15 silicon ~ 380 μm thick, from which we cut rectangular samples with an area of about 1.5 cm^2. Before the diffusant was deposited, the samples were washed in acetone, toluene, hydrofluoric acid and aqua regia, a boiling mixture of H_2O_2:HCl, and distilled water.

The diffusion was carried out from a layer of diffusant deposited on the sample surface in the form of an alcohol solution of the chloride of radioactive promethium ^{147}Pm. After the diffusant was deposited on the surface the samples were dried in air. The uniformity of the deposition was checked by an autoradiographic method.

The diffusion annealing was carried out in air in closed ampoules. The ampoules containing the samples were placed in a diffusion oven (SDO-1) equipped with an REPID programmable temperature regulator able to maintain a temperature with an accuracy of 1 °C. The temperature range of diffusion was from 1100 to 1250 °C. The annealing lasted from 8 to 48 h.

After the diffusion annealing the samples were washed many times sequentially in hydrofluoric acid, a boiling mixture of H_2O_2:HCl, and distilled water. This washing treatment usually removed completely the radioactive impurity remaining on the surface. Then the edge of the sample was trimmed back to a depth of about 80–100 μm, considerably greater than the diffusion depth (~ 10 μm).

The impurity profile was determined by successively removing layers and measuring the residual radioactivity of the sample. The layers were removed chemically in an etchant composed of 1HF: 40HNO_3. After each layer was removed the samples were washed in a boiling solution of H_2O_2:HCl and distilled water. The thickness of the removed layer was determined by weighing the sample with a VLR-20g semimicroanalytic balance. The thickness removed was usually 0.1–0.5 μm. The residual activity of the sample was measured in a UMF-1500M low-background apparatus with an SBT beta-ray spectrometer, on a BDBSZ-1 eM apparatus with a NaI(Tl) scintillation counter, and also an AI-1024 pulse-height analyzer.

Autoradiographic measurements were carried out on the sample to check the uniformity in the distribution of the radioactive isotope over the cross section of the sample as the layers were removed.

The data from the autoradiographic investigations showed that the deposition was uniform and the distribution of the diffused promethium isotope was even over the cross section surface at various depths from the original surface, and, as in the case with other rare-earth elements investigated by us, no inclusions of a second phase were present.[4–6]

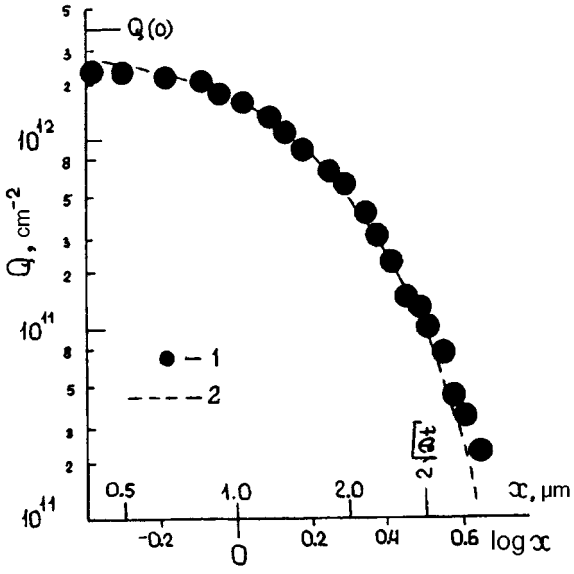

FIG. 1. Profile of the residual amount of radioactive promethium in silicon. $T = 1200$ °C, $t = 10$ h; ●—experiment, - - - —calculation from theory.

 1063-7850/97/010068-02$10.00

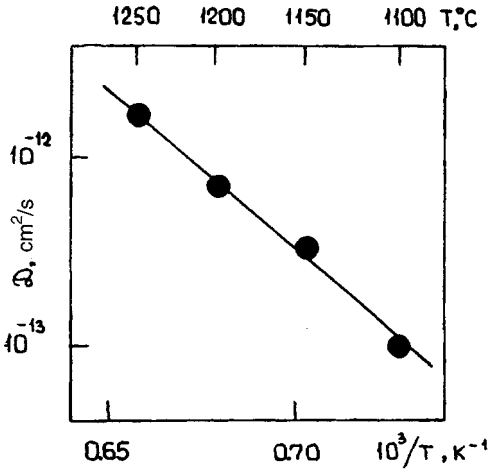

FIG. 2. Temperature dependence of the diffusion coefficient for promethium in silicon.

These results show that the curves of the residual amount of impurity (see, e.g., Fig. 1) can be described by the error function, erfc, corresponding to the solution of Fick's diffusion equation for an infinitely thin source. The diffusion coefficient of promethium in silicon calculated from the residual impurity curves increases with the temperature from $\sim 10^{-13}$ cm^2/s to $\sim 1.5\times 10^{-12}$ cm^2/s. Figure 2 shows the temperature dependence of the diffusion coefficient of promethium in silicon. The temperature dependence of the diffusion coefficient follows the Arrhenius law and can be described by the relation

$$\mathcal{D}=5\times 10^{-3}\exp\left(-\frac{3.3\ \text{eV}}{KT}\right)\ \text{cm}^2/\text{s}.$$

The results show that the penetration depth of promethium in silicon is given by the quantity $2\sqrt{\mathcal{D}t}$, and over the entire experimental temperature range does not exceed a few microns.

An analysis of our data shows that the diffusion coefficient and the activation energy of promethium in silicon lie in a range of values characteristic for the diffusion of typical group III elements in silicon, boron, aluminum, indium, gallium, and thallium, which are substitutional impurities and diffuse by way of the crystal lattice sites.[7] Thus our results support similar conclusions we have drawn previously regarding the diffusion mechanism of rare-earth elements in silicon.[4–6]

[1] J. Mandelkorn, L. Schwartz, J. Broder, H. Kautz, and R. Ulman, J. Appl. Phys. **35**, 2258 (1964).
[2] N. T. Bagraev L. S. Vlasenko. V. M Volle, V. B. Voronkov, I. V. Grekhov, V. V. Dobrovenskiĭ, and A. I. Shagun, Zh. Tekh. Fiz **54**, 917 (1984) [Sov. Phys. Tech. Phys. **27**, 547 (1984)].
[3] D. É. Nazyrov, A. R. Regel', and G. S. Kulikov, Preprint No 1122, A. F. Ioffe Physicotechnical Institute, Russian Academy of Sciences, Leningrad, (1987).
[4] D. É. Nazyrov, G. S. Kulikov, and R. Sh. Malkovich, Pis'ma Zh. Tekh. Fiz. **14**, 1102 (1988) [Sov. Tech. Phys. Lett. **14**, 483 (1988)].
[5] D. É. Nazyrov, G. S. Kulikov, and R. Sh. Malkovich Fiz. Tekh. Poluprovodn. **25**, 1653 (1991) [Sov. Phys. Semicond. **25**, 997 (1991)].
[6] G. K. Azimov, S. Z. Zaĭnabudinov, and D. É. Nazyrov, Fiz. Tekh. Poluprovodn. **23**, 556 (1989) [Sov. Phys. Semicond. **23**, 347 (1989)].
[7] W. Frank, U. Gösele, H. Mehrer, and A. Seeger, in *Diffusion in Crystalline Solids*, ed. by G. E. Murch and A. S. Nowick, New York, 1984, p. 76.

Translated by J. R. Anderson

Self-similarity and branching of wavelet transforms of microwave signals generated by a vircator

V. E. Vatrunin, A. E. Dubinov, and V. D. Selemir

Russian Federal Nuclear Center, All-Russia Scientific-Research Institute of Experimental Physics, Sarov (Arzamas-16)
(Submitted July 1, 1996)
Pis'ma Zh. Tekh. Fiz. **22**, 92–96 (December 26, 1996)

The turbulence regimes of an electron flow with a virtual cathode are studied. The microwave signals generated by a vircator are calculated by the method of large particles. The wavelet transforms of these signals are constructed, and it is shown that they have a complicated self-similar and branching structure. It is concluded that the turbulence of an electron flow is caused by macroscopic instabilities.
[S1063-7850(96)04112-2]

Microwave generators based on a virtual cathode, so-called vircators, are now some of the most promising devices in relativistic electronics.[1–3] However, the theoretical description of the behavior of the electron flow in them meets with well-known difficulties associated with the multivaluedness of the velocity of the electrons in the flow and with thermalization[4] and turbulence[5,6] processes in the initially monoenergetic flow near the virtual cathode, which result in the complicated structure of the generation spectra.[7]

The present work is a continuation of the series of investigations[4–7] of turbulence regimes of an electron flow in the presence of a virtual cathode in the flow.

Two types of turbulence in electron flows are distinguished:[8] weak turbulence, associated with an initial thermal spread of the velocities of the electrons injected into the drift chamber, and strong turbulence, associated with the macroscopic instabilities of the electron flow. It is conjectured that the latter type, against the background of which the initial thermal spread is not noticeable, determines the state of an electron flow with a virtual cathode.

By analogy with hydrodynamic macroscopic instabilities, such as Bénard convection, Taylor flow between rotating cylinders, and so on, the instability of an electron flow with a virtual cathode must be accompanied by self-similar (or self-affine) subdivision of the pulsation scales, complicated energy transfer along the spectrum of these pulsations, branching (bifurcation) of a number of dependences, and a fractal nature of the dynamical attractors of the flow.

In Ref. 5 the fractal dimensions of these attractors were calculated and it was shown that they are large ($d \sim 8-12$) and are in principle fractional. This indicates that here the turbulence of the electron flow is at least fractal and correlations in it decouple quite rapidly:

$$\langle E(t) \cdot E(t+\tau) \rangle = \text{const}/\tau^d, \tag{1}$$

where $E(t)$ is the microwave signal.

At the same time, this result is not revealing, and to demonstrate self-similarity and bifurcation in $E(t)$ the formalism of wavelet transforms,[9,10] which has already been tested in processing of complex signals, could be helpful.

To this end, the microwave generation signals $E(t)$ of a nonrelativistic vircator were calculated. The modeling and calculation were performed according to the program described in detail in Ref. 11 and employing the simplest variant of the large-particle method, in which the large particles are infinitely thin charged planes and the interaction space is represented in the form of two planar gaps: a diode gap L_d of unit length ($L_d = 1$) and a drift gap of length L_p (Fig. 1).

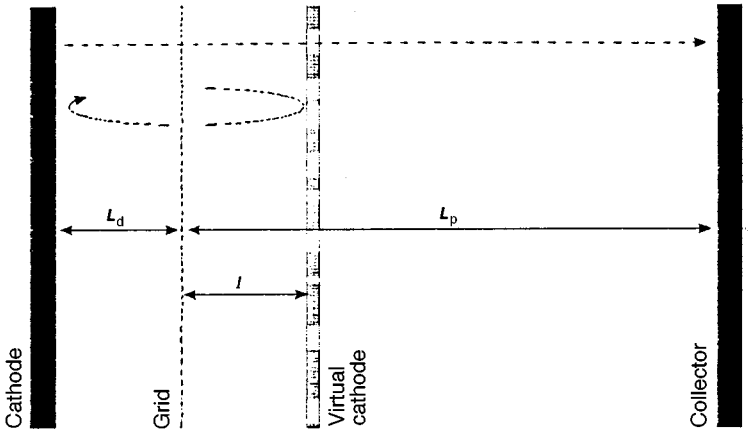

FIG. 1. Modeling scheme.

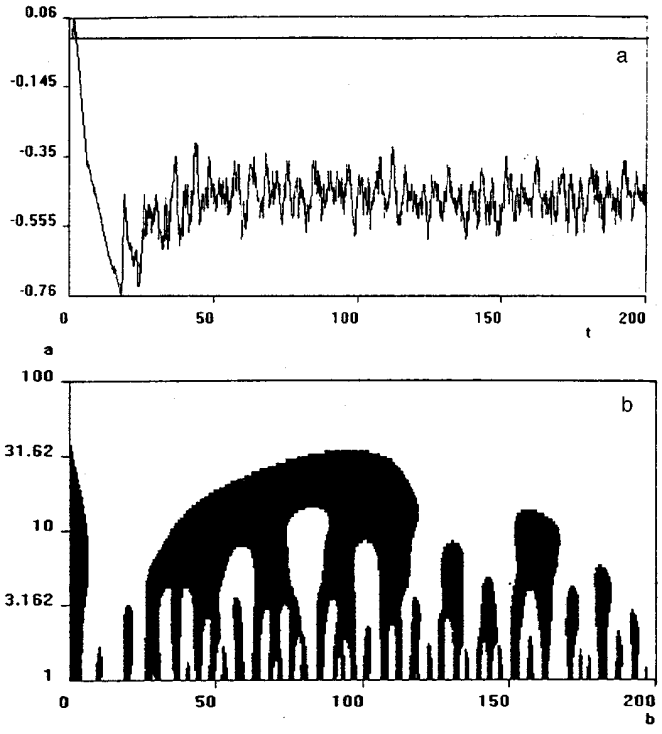

FIG. 2. Computational results: a — $E(t)$; b — section of the wavelet transform $W(a,b)$.

The potential U_e of the emitting electrode (cathode) equals zero, and the potentials U_a and U_c of the anode grid and the collector, respectively, equal unity.

The dynamics of the separate sheets was calculated by means of step integration of the system of normalized differential equations of motion:

$$\frac{d}{dt}z_i=\nu_i \quad \text{and} \quad \frac{d}{dt}\nu_i=E_i, \tag{2}$$

where the magnitude of the electric field is expressed in the form

$$E_i-\frac{U_a-U_e}{L_d}+\sum_{j<i}^{N_d^-}\lambda_j-\sum_{j>i}^{N_d^+}\lambda_j \tag{3}$$

in the diode gap and in the form

$$E_i=\frac{U_e-U_c}{L_p}+\sum_{j<i}^{N_p^-}\lambda_j-\sum_{j>i}^{N_p^+}\lambda_j \tag{4}$$

in the drift gap. Here $N_{d,p}^-$ and $N_{d,p}^+$ are the number of particles in front of and behind the ith sheet, respectively, and λ_i is the effective charge of the ith sheet.

It was found that for $\lambda_i=10^{-2}$ and all i a virtual cathode forms for $L_p>5$, and its position is determined by the average distance l from the anode grid approximately equal to L_d. The time-dependent behavior of the electric field $E(t)$ near the virtual cathode was calculated. The typical time dependence of the field is shown in Fig. 2a (the calculation was performed with $L_d=10$).

The wavelet transform $W(a,b)$ of the signal $E(t)$ was calculated as follows:

$$W(a,b)=a^{-1/2}\int \Psi\left(\frac{t-b}{a}\right)E(t)dt, \tag{5}$$

where the wavelet $\Psi(x)$, as in Ref. 9, was chosen in the form

$$\Psi(x)=(1-x^2)\exp(-x^2/2), \tag{6}$$

often called a Mexican hat type wavelet.

The section of the wavelet transform $W(a,b)$ by the plane $W(a,b)=0$ in a logarithmic scale with respect to a so that the region $W(a,b)>0$ is colored black is displayed in Fig. 2b.

The branched and self-similar structure of the picture of the wavelet transform attest to the fact that a state with strong turbulence, developing as a result of macroscopic instability, is indeed realized in the electron flow.

[1] B. V. Alyokhin, A. E. Dubinov, V. D. Selemir *et al.*, IEEE Trans. Plasma Sci. **PS-22**, 945 (1994).
[2] V. D. Selemir, B. V. Alekhin, V. E. Vatrunin *et al.*, Fiz. Plazmy **20**, 689 (1994) [Plasma Phys. Rep. **20**, 621 (1994)].
[3] A. E. Dubinov and V. D. Selemir, Zarubezhnaya Radioélektron., No. 4, 54 (1995).
[4] V. D. Selemir, A. E. Dubinov, and I. G. Prikhod'ko, Voprosy atomnoĭ nauki i tekhniki, Ser. Teoreticheskaya i prikladnaya fizika, No. 1, 23 (1993).
[5] V. E. Vatrunin, A. E. Dubinov, V. D. Selemir, and N. V. Stepanov, in *Fractals in Applied Physics* [in Russian], edited by A. E. Dubinov, Arzamas-16, 1995, p. 47.
[6] V. E. Vatrunin, A. E. Dubinov, V. D. Selemir, and N. V. Stepanov, in *Lectures on Microwave Electronics and Radiophysics* [in Russian], Saratov, 1996, Vol. 2, p. 89.
[7] V. E. Vatrunin, A. E. Dubinov, and V. D. Selemir, Voprosy atomnoĭ nauki i tekhniki, Ser. Teoreticheskaya i prikladnaya fizika, No. 2, 24 (1994).
[8] A. D. Gladun, Élektronnaya tekhnika, Ser. Elektronika SVCh, No. 8, 39 (1966).
[9] A. Arneodo, G. Grasseau, and M. Hotschneider, Phys. Rev. Lett. **61**, 2281 (1988).
[10] N. M. Astaf'eva and D. M. Sonechkin, Dokl. Ross. Akad. Nauk **344**, 539 (1995).
[11] V. E. Vatrunin, A. E. Dubinov, and V. D. Selemir, Preprint No. 31–93, All-Russia Scientific-Research Institute of Experimental Physics, Arzamas-16 (1993).

Translated by M. E. Alferieff

Conversion of infrared radiation into visible in ZBLAN glass with three-component doping by rare-earth elements

I. A. Grishin, V. A. Gur'ev, V. L. Mart'yanov, and A. P. Savikin

N. I. Lobachevskiĭ State University, Nizhniĭ Novgorod
(Submitted October 29, 1996)
Pis'ma Zh. Tekh. Fiz. **23**, 51–57 (January 26, 1997)

Experimental results are presented that lead to the conclusion that new laser systems and elements of fiber-optic communication lines can in principle be made on the basis of the material studied here, which have new spectroscopic characteristics. The effect studied in this paper is the following: an increase in the luminescence efficiency with frequency upconversion for three-element doping; this is a novel finding and has no analog. © *1997 American Institute of Physics.* [S1063-7850(97)02401-4]

1. INTRODUCTION

One of the ways to convert infrared light to the visible range is with sensitized luminescence and stage-wise pumping of the higher levels of trivalent rare-earth ions in fluoride crystals and glasses.[1] In earlier experiments[2] we found the optimum concentration of $Yb^{3+}+Er^{3+}$ donor-acceptor ion pairs for the efficient conversion of infrared radiation of a semiconductor laser ($\lambda_p=975$ nm) into green radiation with $\lambda_{lum}=$ 515–555 nm.

This article reports an experimental investigation of the luminescence and frequency up-conversion in the synthetic fluorozirconate glass ZBLAN (Ref. 3) doped with the combination $Yb^{3+}+Er^{3+}+Ho^{3+}$ (Table I).

2. EXPERIMENT

To investigate the luminescence with frequency upconversion we used a spectroscopic apparatus based on a DFS-12 grating spectrograph (resolution better than 0.1 nm) with an FÉU-79 photomultiplier. CAMAC crate modules connected to a 286 PC by a GeoSoft CC controller were used to process the photomultiplier signal, tune the region of the spectrum, and supply the laser pumping.

The glass samples were optically pumped in the same way as in Ref. 2, with the radiation from a cw InGaAs–GaAs semiconductor quantum-well laser at a wavelength $\lambda_p=975$ nm and a power up to 700 mW. The pump radiation was collimated onto the glass sample by a microscope objective for unambiguous reproducibility of the excited volume.

In the experiments we used samples of ZBLAN glass 2 mm thick with various concentrations of Ho^{3+} shown in Table I in mole per cent.

The characteristic luminescence spectra of the samples with the double doping Er + Yb (N1) and Ho + Yb (N2) are shown in Fig. 1, and for triple doping in Fig. 2.

3. DISCUSSION

The energy level diagram of this system of ions is shown in Fig. 3. In studying the processes that lead to an enhanced efficiency in the infrared → ''green'' conversion in the $Yb^{3+}+Er^{3+}$ pair (Ref. 2) we identified two main processes: an increase in the rate of pumping of the upper level of the transition $^4S_{3/2}\rightarrow{}^4I_{15/2}$ in Er and the effective quenching of the lower-lying metastable state $^4I_{13/2}$ (the lifetime is $\tau_R\simeq 7.8$ ms for the radiative transition to the ground state at the wavelength $\lambda_{lum}\sim 1.55$ μm).

The $^4I_{13/2}$ level of erbium can be quenched by introducing into the sample an additional type of rare-earth dopant ion whose energy level lies below the $^4I_{13/2}$ level and to which it is possible to transfer energy of excitation by the dipole-dipole interaction or phonon relaxation, for example, Tb^{3+}, Nd^{3+}, Ho^{3+}, or Pr^{3+}. The luminescence channels in most of these ternary compositions lie in the near- or mid-infrared range. Similar pumping schemes have been used for increasing the pumping efficiency for a number of crystalline infrared lasers (see, e.g., Ref. 5).

Our experiments with Tb^{3+} have shown that the higher-lying levels of this ion also interact with erbium, removing some of the energy from it, so that the efficiency of the green luminescence is substantially reduced. However, for Ho^{3+} we observed that the efficiency of the green luminescence is enhanced (the integrated intensity increased by a factor of 1.72 in the range $\lambda=530$–555 nm for samples N3 and N4 compared with N1). The reasons are as follows. First, the low-lying level of this ion, $^5I_7$, is able effectively to empty the higher level, $^4I_{13/2}$, of erbium via the dipole-dipole interaction assisted by phonons from the glass matrix (the energy gap is $\Delta E\simeq 1500$ cm^{-1} with an average phonon energy in ZBLAN of around 575 cm^{-1}; Ref. 2), and hence the erbium ions, giving up energy to the holmium ions, return to the ground state and again take part in the pumping process. This supposition is supported by the reduction of the infrared in-

TABLE I.

	ZrF_4	BaF_2	AlF_3	YbF_3	ErF_3	HoF_3	NaF
1	52	20	4	3	1	–	20
2	52	20	4	3	–	1	20
3	51.75	20	4	3	1	0.25	20
4	51.5	20	4	3	1	0.5	20
5	51	20	4	3	1	1	20

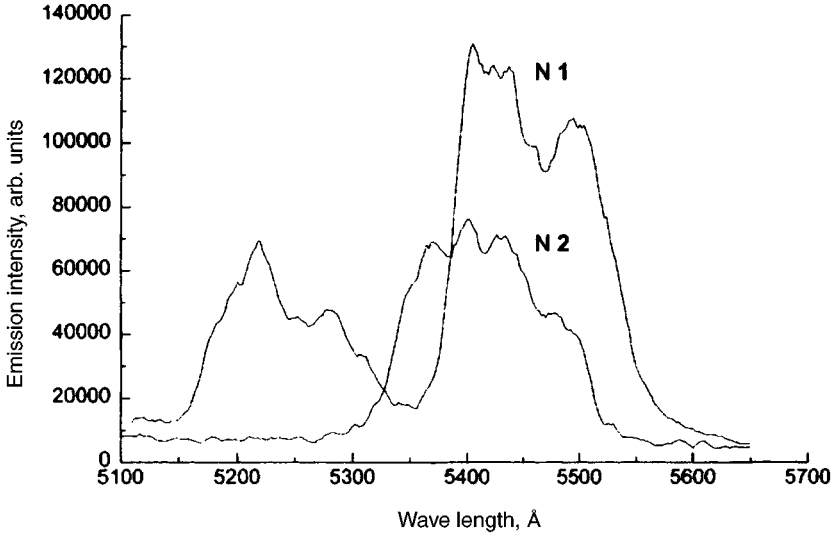

FIG. 1. Luminescence spectrum with frequency up-conversion in binary compositions Er^{3+} + Yb^{3+}: ZBLAN (N1) and Ho^{3+} + Yb^{3+}:ZBLAN (N_2).

tensity in the region of 1.55 μm with increased concentration of the holmium ions (Fig. 4).

Second, as one can see from the luminescence spectrum, the high-lying levels of Ho^{3+}, the $^5F_3$, and the overlapping $^5F_4$ and $^5S_2$ levels participate in the sensitized luminescence[4] in the region λ_{lum}= 535–550 nm. Because of the small energy gap between the upper radiative levels of holmium, $^5S_2$, and erbium, $^4S_{3/2}$, nonradiative transfer of energy to the erbium is possible, and this should reduce the intensity of the holmium emission in the region around 537 nm, but this effect is not observed experimentally. It is possible that this result explains the high rate of radiative transitions of holmium, $^5S_2 \rightarrow {}^5I_8$ ($\lambda_{lum} \simeq 537$ nm), compared with the inter-ion energy transfer. Moreover, this wavelength range coincides with the minimum of the erbium absorption and does not undergo quenching.

The transfer of energy from the $^2H_{11/2}$ level of erbium to holmium is also observed, as is indicated by the decrease in the intensity of the short wavelength part of the emission at 530 nm (the $^2H_{11/2} \rightarrow {}^4I_{15/2}$ transition; compare Figs. 1 and 2). In this case the rate of inter-ion energy transfer is obviously greater than the radiative relaxation of the erbium $^2H_{11/2}$ level.

4. CONCLUSIONS

As noted in Refs. 1 and 2, luminescence with frequency up-conversion in doped fluorozirconate ZBLAN glasses holds out promise for developing fiber-optic amplifiers and lasers for the visible, near infrared, and the near ultraviolet with pumping by high-efficiency infrared semiconductor lasers. The investigations carried out here into the effects of controlling the luminescence spectrum and enhancing the efficiency of the conversion by introducing additional dopant impurities can extend the capabilities of the devices that are created and improve their characteristics.

The results of these experiments are indicative of better luminescence characteristics of the ternary composition Yb^{3+} + Er^{3+} + Yb^{3+} compared to those of the binary compositions Yb^{3+} + Er^{3+} or Yb^{3+} + Ho^{3+}. The luminescence

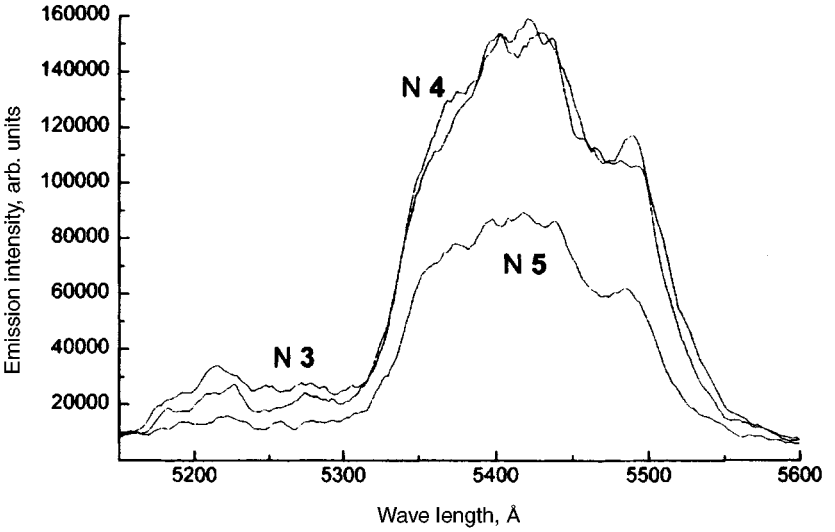

FIG. 2. Luminescence spectrum of the ternary compositions Er^{3+} + Yb^{3+} + Ho^{3+}:ZBLAN (labeled as in Table I).

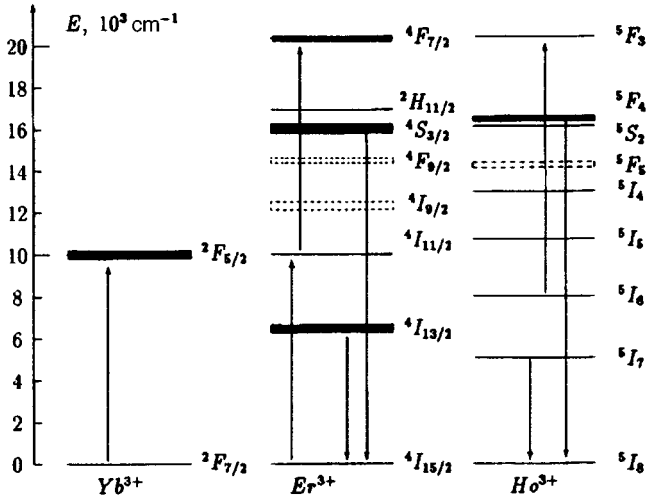

FIG. 3. Energy level diagram for Er^{3+} + Yb^{3+} + Ho^{3+} (the arrows indicate the excitation and luminescence transitions with frequency upconversion).

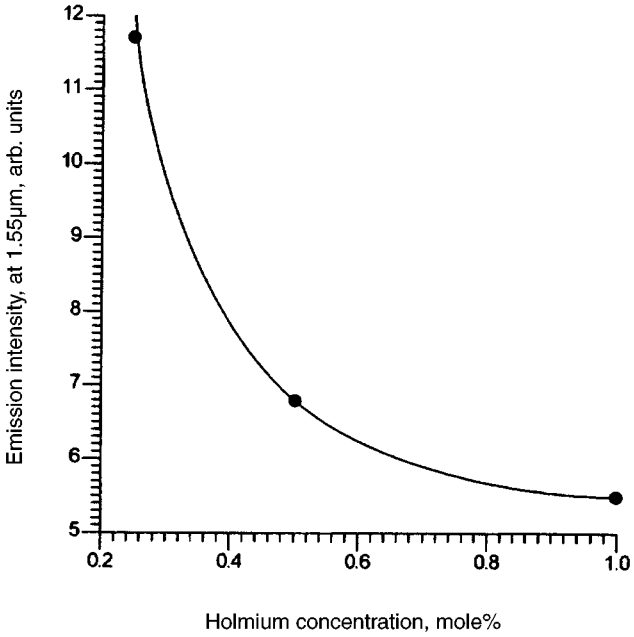

FIG. 4. Luminescence intensity of the composition Er+Yb+Ho:ZBLAN at 1.55 μm versus the holmium concentration.

intensity integrated over the spectrum, while increasing by a factor of 1.72, was, moreover, smoother and concentrated in the region of 535–555 nm. Experiments that are planned for studying the spectral dependence of the luminescence quenching time will permit a quantitative assessment of the probability of energy transfer and give a more detailed explanation of the observed phenomena.

The authors are indebted to Prof. A. A. Andronov for discussions and to N. B. Zvonkov for supplying the semiconductor laser and for his cooperation.

This work on the energy transfer processes in rare-earth doped fluorozirconate glasses was supported by the Russian Fund for Fundamental Research (Grant No. 96-02-16996a).

[1] F. E. Auzel, Proc. IEEE **61** , 758 (1973).
[2] I. A. Grishin, V. A. Guryev, A. P. Savikin, and N. B. Zvonkov, Opt. Fiber Tech. **1**, 331 (1995).
[3] I. A. Grisnin, G. G. Devyatykh, E. M. Dianov *et al.*, Kvantovaya Elektron. (Moscow) **14**, 377 (1987) [Sov. J. Quantum Electron. **17**, 229 (1987)].
[4] K. Tanimura, M. D. Shinn, W. A. Sibley, M. G. Drexhage, and R. N. Brown Phys. Rev. B **30**, 2429 (1984).
[5] T. Y. Fan and R. L. Byer, IEEE J. Quantum Electron. **QE- 24**, 895 (1988).

Translated by J. R. Anderson

Concerning the polarization vector of a wave reconstructed by a pseudodeep volume grating

S. Ya. Gorelik and I. M. Nagibina

St. Petersburg Institute of Precise Mechanics and Optics (Technical University)
(Submitted March 29, 1996)
Pis'ma Zh. Tekh. Fiz. **23**, 58–63 (January 26, 1997)

It is shown theoretically and experimentally that for non-Bragg readout of a pseudodeep hologram recorded in a thick-layer medium the wave reconstructed by the hologram changes its state of polarization. © *1997 American Institute of Physics.* [S1063-7850(97)02501-9]

A method has recently been proposed for recording and reconstructing images with the use of so-called pseudodeep holograms,[1,2] which are interesting because of their diffraction properties. In this paper we show that when the angle of incidence of the reconstructing wave onto the pseudodeep volume grating deviates from the Bragg angle the polarization vector of the reconstructed wave changes.

Let us consider a light-sensitive medium situated between the planes $z=x\ \cot\beta$ and $z=x\ \cot\beta+d/\sin\beta$ [where β is the angle of inclination of the medium to the horizontal plane and d is the physical thickness of the emulsion (Fig. 1)], which records the results of interference of an object plane wave S_0 and a reference plane wave R_0 with complex amplitudes $S_0=\exp(-j\sigma_0 x)$ and $R_0=\exp(-j\rho_0 x)$, where $\sigma_0=(0;\sigma_{0y};\sigma_{0z})$ and $\rho_0=(0;\rho_{0y};\rho_{0z})$ are the wave vectors of the object and reference wave respectively: $|\sigma_0|=|\rho_0|=2\pi n/\lambda$; λ is the wavelength in vacuum, n is the refractive index of the medium, and $x=(x,y,z)$ is the position vector. For linear recording the grating that is produced can be represented as the modulation of the permittivity ε and/or the conductivity σ of the medium:[3]

$$\varepsilon=\varepsilon_0+\varepsilon_1\cos(K\cdot x);\quad \sigma=\sigma_0+\sigma_1\cos(K\cdot x), \tag{1}$$

where ε_1 and σ_1, ε_0 and σ_0 are, respectively, the modulation amplitude and the mean values of ε and σ, and the vector K is defined by the relation $K=\rho_0-\sigma_0$.

We illuminate the grating by a wave with a complex amplitude $R=R(z)\exp(-j\rho x)$ traveling in the horizontal plane; its direction of propagation and wavelength are in general different from those used in the recording. This wave reconstructs a wave with a complex amplitude $S=S(z)\exp(-j\sigma x)$ with a wave vector σ determined by the vectors K and ρ, and in general it departs from the horizontal plane,[1] i. e., $\sigma=(\sigma_x;\sigma_y;\sigma_z)$.

The resultant electromagnetic wave E in the volume of the grating is a superposition of the object and reference wave, and its propagation in the volume of the light-sensitive medium is described by the wave equation

$$\nabla^2 E-\text{grad}\ \text{div}E+\mathcal{K}^2E=0, \tag{2}$$

where $\mathcal{K}$ is the complex propagation constant associated with the quantities ε and σ by the relation $\mathcal{K}^2=(\omega^2/c^2)\varepsilon-j\mu\omega\sigma$, c is the speed of light in vacuum, μ is the magnetic susceptibility of the medium, and ε and σ are given by expressions (1).

Substituting these values into expression (2) and neglecting second derivatives and waves traveling in the directions $\rho+K$ and $\sigma-K$ (Ref. 3), we obtain the following system of first-order coupled-wave equations

$$\begin{aligned}
&c_R R_x'+\alpha R_x=-j\varkappa S_x,\\
&c_s S_x'+\left(\alpha+jv+j\frac{\sigma_x^2}{2\rho}\right)S_x+j\frac{\sigma_x\sigma_y}{2\rho}S_y-\frac{\sigma_x}{2\rho}S_z'\\
&\quad+j\frac{\sigma_x\sigma_z}{2\rho}S_z=-j\varkappa R_x,\\
&c_R R_y'+\left(\alpha+j\frac{\rho_y^2}{2\rho}\right)R_y-\frac{\rho_y}{2\rho}R_z'+j\frac{\rho_y\rho_z}{2\rho}R_z=-j\varkappa S_y,\\
&c_S S_y'+\left(\alpha+jv+j\frac{\sigma_y^2}{2\rho}\right)S_y+j\frac{\sigma_y\sigma_z}{2\rho}S_z\\
&\quad-\frac{\sigma_y}{2\rho}S_z'+j\frac{\sigma_x\sigma_y}{2\rho}S_x=-j\varkappa R_y,\\
&\left(\alpha+j\frac{\rho_z^2}{2\rho}\right)R_z-\frac{\rho_y}{2\rho}R_y'+j\frac{\rho_y\rho_z}{2\rho}R_y=-j\varkappa S_z,\\
&\left(\alpha+jv+\gamma\frac{\sigma_z^2}{2\rho}\right)S_z+j\frac{\sigma_x\sigma_y}{2\rho}S_x-\frac{\sigma_x}{2\rho}S_x'\\
&\quad-\frac{\sigma_y}{2\rho}S_y'+j\frac{\sigma_y\sigma_z}{2\rho}S_y=-j\varkappa R_z,
\end{aligned} \tag{3}$$

where $v=(\rho^2-\sigma^2)/2\rho$; R_x,R_y,R_z and S_x,S_y,S_z are the x-, y-, and z components of the reconstructing and reconstructed waves, respectively, $c_R=\rho_t/\rho$, $c_s=\sigma_z/\rho$, $\varkappa$ is a coupling constant, α is the average absorption coefficient,[3] and the primes denote differentiation with respect to z.

An analysis of this system leads to the following conclusions.

1. When the reference wave is incident at the Bragg angle, and when $\sigma_x=0$, the system of equations (3) divides into two: the first two equations correspond to TE-polarization of the reconstructing wave and the rest correspond to TM-polarization; both of these systems are the same as those derived in Ref. 3.

 1063-7850/97/010073-02$10.00

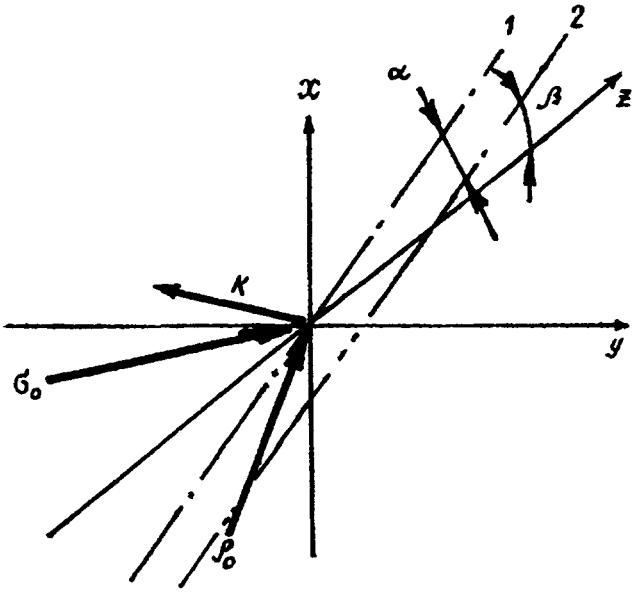

FIG. 1. Diagram of the recording of the result of the interference of two plane waves with wave vectors ρ_0 and σ_0. K is the grating vector; d is the physical thickness of the emulsion, β is the angle of inclination of the recording medium. The dashed lines indicate the traces of the intersection of the front (*1*) and the back (*2*) surfaces of the photographic emulsion with the vertical XZplane.

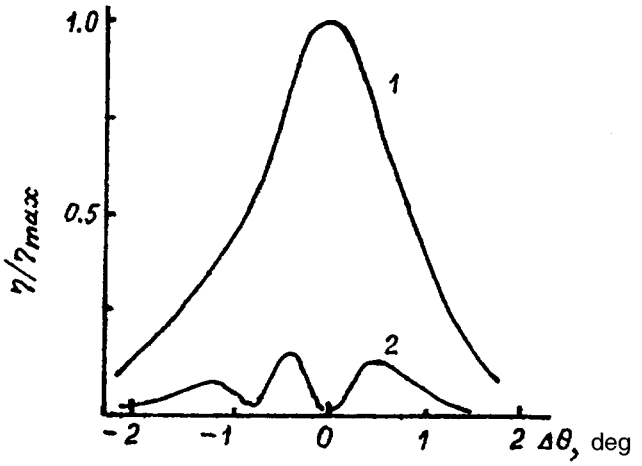

FIG. 2. Relative diffraction efficiency $\eta/\eta_{\max}$ of a pseudodeep volume grating for the vertical (*1*) and horizontal (*2*) component of the polarization of the reconstructed radiation, plotted against the direction of propagation of the reference wave at an angle $\Delta\Theta$ to the horizontal YZ plane.

2. Away from Bragg conditions the vertical and horizontal polarization components of the reconstructed wave are coupled. As a result the polarization vectors of the object and reference waves must differ from one another, at least within some range of variation of the angle of incidence.

3. No coupling occurs, however, between the vertical and horizontal polarization components of the reference wave, and consequently the polarization vector of the reference wave cannot change.

To check these conclusions we carried out experiments in which a diffraction grating was recorded in the symmetric two-beam scheme on Du Pont photopolymer film. Then the intensities of the vertical and horizontal components of the reconstructed radiation were measured as the angle of incidence was varied. The measured components were separated by a polarization filter. The spatial frequency of the grating in air was about 500 mm^{-1}. The wavelength of the radiation from a He–Ne laser was $\lambda = 0.4416$ μm and the angle of incidence β on the photographic material was about 20°. Radiation with TE-polarization was used in the recording and reconstruction. The results for the ''Omni-dex'' film with a light-sensitive layer 25 μm thick are shown in Fig. 2, where curve *1* corresponds to the vertical component of the polarization of the reconstructed radiation and curve *2* to the horizontal component. As expected, these curves indicate that the components of the polarization vectors of the initial and reconstructed waves coincide only for the Bragg angle of incidence of the reconstructing wave on the grating.

To eliminate the effect on the results due to induced anisotropy in the material, a wave with TE polarization was used to reconstruct a grating recorded under the same conditions by radiation with TM- polarization. The results were entirely similar to those shown in Fig. 2. However, the polarization vector of the reference wave in the two cases did not depend on the angle of incidence.

It must be mentioned that this phenomenon is not observed in investigations with thin amplitude- or phase pseudodeep gratings recorded with FP-R photographic film.

In summary, the results presented above allow us to state that the polarization of the wave reconstructed by a pseudodeep isotropic volume grating is the same as the polarization of the reference wave only for exact Bragg incidence of the latter on the grating, while this phenomenon is not characteristic of gratings recorded in thin photosensitive material.

To conclude, the authors would like to take this opportunity to thank Yu. N. Denisyuk for helpful discussions of the results of this work and for kindly providing the opportunity to carry out these experiments.

[1] Yu. N. Denisyuk and N. M. Ganzherli, Zh. Tekh. Fiz. **60**(11), 154 (1990) [Sov. Phys. Tech. Phys. **35**, 1321 (1990)].
[2] Yu. N. Denisyuk and N. M. Ganzherli, Pis'ma Zh. Tekh. Fiz. **18**(2), 15 (1992) [Sov. Tech. Phys. Lett. **18**, 31 (1992)].
[3] H. Kogelnik, Bell Syst. Tech. J. **48**, 2909 (1969).
[4] A. Gerrard and J. M. Burch, *Introduction to Matrix Methods in Optics* (Wiley, New York, 1975) [Russ. Transl., Nauka, Moscow, 1979].

Translated by J. R. Anderson

Localization of an rf capacitive discharge in a long strip line

Yu. P. Raĭzer

Institute of Problems in Mechanics, Russian Academy of Sciences, Moscow

M. N. Schneĭder

All-Russian Scientific Research Center, VÉTs, Istra
(Submitted November 18, 1996)
Pis'ma Zh. Tekh. Fiz. **23**, 64–70 (January 26, 1997)

The self-consistent problem of a an intermediate-pressure rf capacitive discharge in a long strip line is analyzed with allowance for heating of the gas. Steady-state distributions of the discharge parameters along the line are derived. It is shown that the discharge burns in certain regions, whose lengths and locations depend on the amplitude of the applied voltage.
 [S1063-7850(97)02601-3]

1. We shall consider the organization of an rf capacitive discharge in a gas, generated between long, closely spaced electrode strips by a high-efficiency and compact CO_2 laser.[1] The frequency f of the field can be increased by increasing the laser power.[2] However, for $f>100-150$ MHz harmful wave effects come into play, which result in large variations in the amplitude of the rf voltage V_a along the strip (along the x axis). In Ref. 3, where the distribution $V_0(x)$ was measured, the effect was also analyzed theoretically. It was assumed that a long line, like the electrodes of a strip line, is heated by the discharge with specified linear parameters that do not depend on the position x. The model correctly reflects the nature of the distribution $V_a(x)$, but does not address the nonuniformity of the discharge and its inverse influence on $V_a(x)$.

In this paper we examine the self-consistent problem of a long line maintaining an rf discharge. Here a key role is played by the effect of the normal current density, inherent in an rf discharge. It results from heating of the gas in the discharge and is also extremely important in connection with laser characteristics. The solution reveals new features of an rf discharge in a stripline system The discharge burns in certain regions on the x axis, whose extent and locations depend on the amplitude of the applied voltage. The discharge is anomalous everywhere except at the edges, where it is normal. When the voltage is increased the discharge regions expand, like it does with increased current in the normal regime at lower frequencies. For a fixed rf generator voltage and impedance of the external circuit, the current, voltage, and geometry of the discharge regions are completely determined by the current-voltage $(I-V)$ characteristic of the discharge system and the load line. The discharge volume can be regulated by varying the parameters of the external circuit. However, if the voltage is increased so as to approach filling the volume with the plasma, then the regions of enhanced anomalous discharge will be overheated to the point where laser generation breaks down. It thus becomes necessary to optimize the parameters of the discharge system and of the external circuit.

It is possible to use radical means to counter the sequences of wave effects by artificially equalizing the voltage along the strip with, let us say, auxiliary distributed inductances or sectored electrodes, but this greatly complicates matters (see the citations in Refs. 2 and 3). On the other hand, an understanding of the true nature of the wave effects on the discharge, which is the goal of this investigation, may help in optimizing uncomplicated systems.

2. Let us consider a steady-state discharge of the α type between the electrode strips of length l, and width a, separated by a distance h. A voltage $V(0)=V_a\exp(i\omega t)$ is applied at the middle, the point $x=0$ (Fig. 1). We write the equation for the complex amplitude of the voltage V and the current I along the electrode line

$$d\overline{V}/dx=-i\omega L_1\overline{I},\quad d\overline{I}/dx=\overline{V}/Z_1,\quad Z_1=Z/a. \tag{1}$$

Here L_1 is the inductance per unit length and Z_1 is the impedance per unit length of the interelectrode space of the

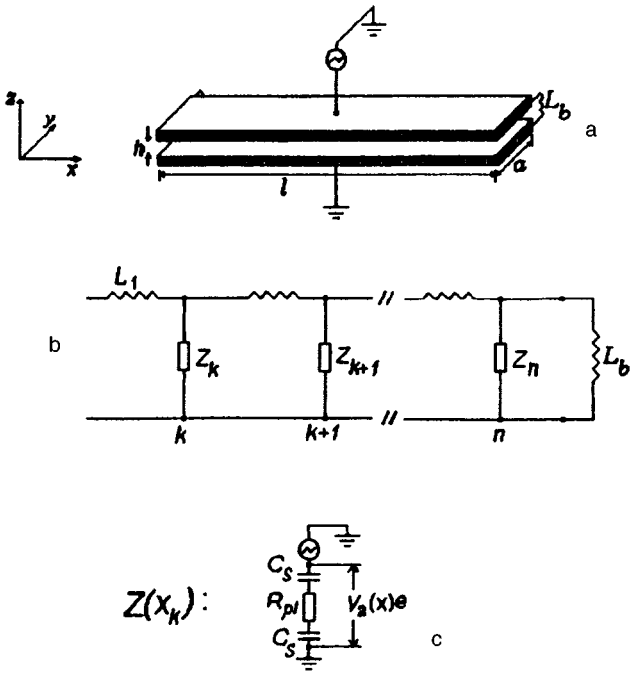

FIG. 1. a—Experimental arrangement of an rf discharge in a stripline;[3] b and c—equivalent circuit of a long line and an elementary transverse rf capacitance α discharge,[2] respectively.

 1063-7850/97/010075-03$10.00

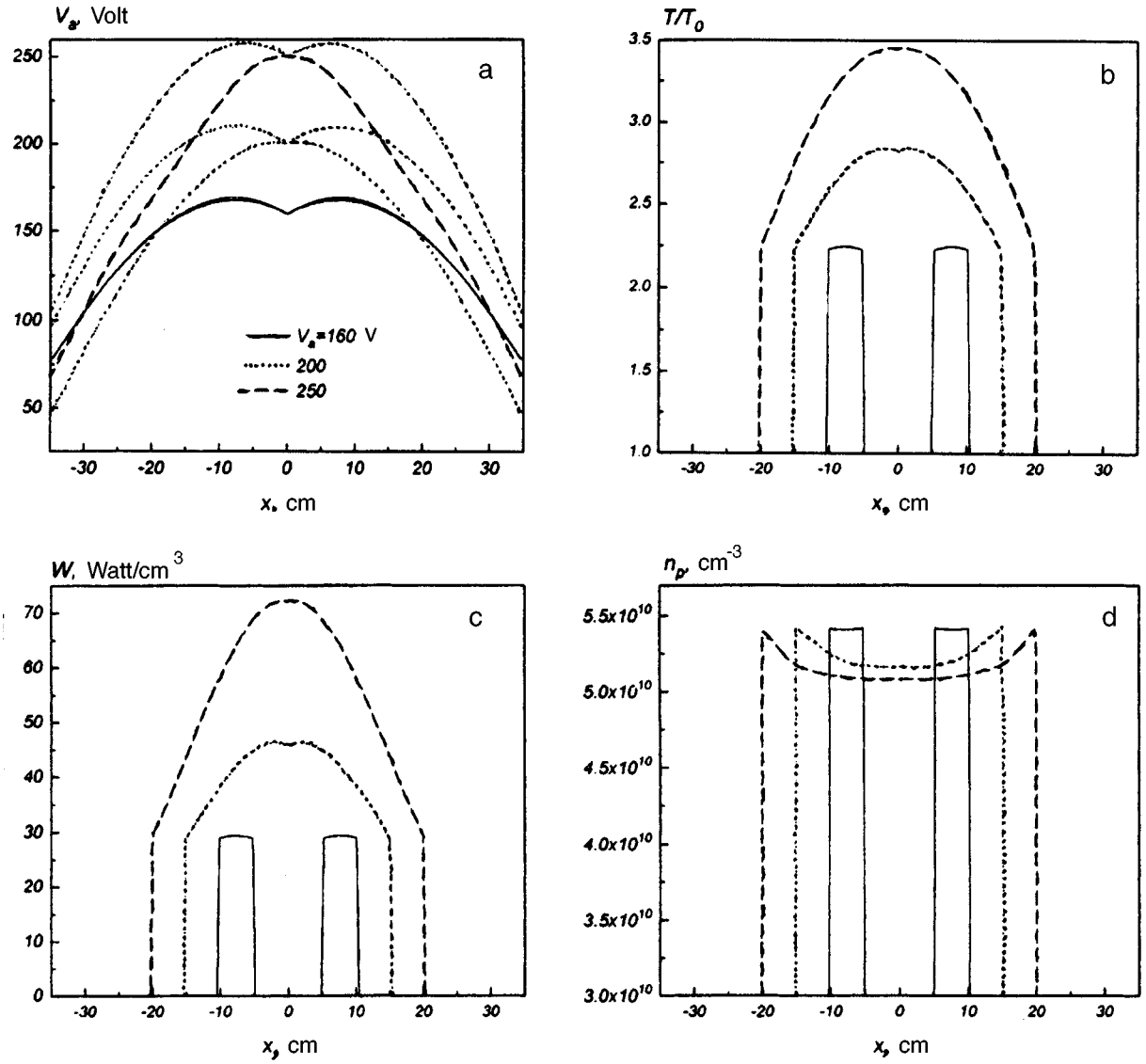

FIG. 2. Longitudinal distribution of the discharge parameters along the strip line for $L_b = 10$ nH and various values of $V_a(0)$: a—peak voltage $V_a(x)$ (the thinner lines represent the corresponding distributions of the voltage without allowance for the discharge); b—gas temperature; c—specific power deposition, and d—plasma density. N_2, $p=100$ Torr, $f=100$ MHz, $L_b=10$ nH.

discharge. The impedance Z per unit area of the electrodes has been calculated in Ref. 2 on the basis of a very simple discharge model:

$$Z(x)=\frac{hm(\nu_m+i\omega)/e^2n+2A\cdot 4\pi/i\omega}{1-\omega^2/\omega_p^2+i\omega\nu_m/\omega_p^2}\ [\Omega\cdot\mathrm{cm}^2]. \qquad (2)$$

The ion density in this model is assumed to be constant along the rf current and is equal to the density of the oscillating plasma, $n=n(x)$. The quantity ν_m is the effective frequency of collision of electrons with molecules, and $\omega_p=(4\pi e^2n/m)^{1/2}$ is the plasma frequency. The oscillation amplitude A of the plasma boundary satisfies the equation

$$A^2[(\omega^2-\omega_p^2\cdot 2A/h)^2+\omega^2\nu_m^2]=(eV_a/mh)^2. \qquad (3)$$

For parameters typical of lasers, $f=100$ MHz, $p=100$ Torr, $h=0.2$ cm, and $n\sim 10^{10}$–10^{11} cm^{-3}, we find $\nu_m\gg\omega$, $A\ll h$, $\nu_m\omega\gg\omega_p^2\cdot 2A/h$. Here, $A(x)\approx\mu_eE_a/\omega$, where $\mu_e=e^2/m\nu_m$ is the electron mobility, and $E_a\approx V_a/h$ is the nominal amplitude of the field in the plasma.

We relate $n(x)$ and the amplitude of the current density $j_a(x)\approx en\mu_eE_a$ with the voltage $V_a(x)$. This voltage is made up of the voltages V_s in the sheaths and that in the plasma, V_p, which are shifted in phase by about $\pi/2$. Therefore

$$V_a=(V_{as}^2+V_{ap}^2)^{1/2}, \qquad (4)$$

where $V_{as}=8\pi enA^2$ (Ref. 2) and $V_{ap}=E_a(h-2A)$. Since $\mu_e\propto N^{-1}$ (where N^{-1} is the number density of the molecules) and the pressure is $p=NkT$, when the gas is heated to a temperature T the quantity $V_{as}=(2e/\pi)\mu_e^{02}(E_a/p)^2(T/T_0)^2nf^{-2}$ remains constant ($p=N_0kT_0$, where $T_0=300$ K is the temperature of the cooled electrodes). The field E_a in the plasma and n are related by the condition of ionization-recombination balance

$$\nu_{i\mathrm{rf}}=\beta n, \quad \nu_{i\mathrm{rf}}\approx(2E_a/\pi B_1 N)^{1/2}\mu_e E_a \alpha(E_a). \tag{5}$$

The ionization rate $\nu_{i\mathrm{rf}}$ in the rf field can be expressed approximately in terms of the Townsend coefficient $\alpha(E) \propto N \exp(-B_1 N/E)$ (Ref. 2). If attachment occurs in the gas, then β can be chosen as the effective recombination coefficient. Finally, T is determined by the heat balance condition, where the heat is carried to the electrodes by thermal conduction. Approximately[2] we have

$$\Theta-\Theta_0=\langle jE\rangle h^2/12, \quad \Theta=\Theta(T), \quad \Theta_0=\Theta(T_0), \tag{6}$$

where $\Theta=\int_0^T \lambda\, dT$ is the heat flux potential, $\lambda(T)$ is the thermal conductivity, $\langle jE\rangle$ is the amount of Joule heating per cm^3 per second averaged over a period. The loss of vibrational energy is not large.[2]

Equations (4)–(6) determine the I-V characteristic of the discharge, $V_a(j_a)$. It has a minimum $V_{\min}$ that corresponds to the normal current density j_{an}. If $j_a<j_{an}$ and $V_a<V_{\min}$, then the discharge cannot burn. In regions where $V_a>V_{\min}$, we have an anomalous discharge, with the points x where $V_a=V_{\min}$ separating the zones with and without current. Using this proposition, which for the mathematical problem can be regarded as a physical postulate, we also solve the system of equations (1)–(6) with the boundary conditions at the ends of the line. Ordinarily the electrodes are closed on the ends by a ballast inductance L_b so that $V(l/2)=i\omega L_b I(l/2)$. The amplitude of the applied voltage, $V_a(0)=V(0)$, is assumed to be a specified parameter; then the solution gives the total discharge current $2\int_0^{l/2} a j_a dx$.

3. In Fig. 2 we show the results obtained from a numerical solution for close to the experimental conditions of Ref. 3: 100 MHz, 100 Torr, $h=$ 0.2 cm, $l=70$ cm, $a=10$ cm, electrode thickness 1 cm, which gives $L_1\approx 9.18\times 10^{-10}$ H/cm. In the absence of a discharge ($n\to\infty$), we find that $Z_1\to 1/i\omega C_1$, where $C_1=a/4\pi h=4.42\times 10^{-12}$ F/cm is the capacitance per unit length of the strip. The wave velocity along the line is $c_1=(L_1/C_1)^{-1/2}=1.57\times 10^{10}$ cm/s, and the wavelength is $\lambda_1=c_1/f\approx 157$ cm $\approx 2.2l$. The discharge is localized at those regions of the strip line where where $V_a(x)>V_{\min}$. For $V_a(0)<V_{\min}$ the plasma does not exist at the middle part of the strip line. For example, this regime of burning is obtained in the calculations for $V_a(0)=160$ V ($V_{\min}\approx 168$ V). When $V_a(0)$ is increased, the discharge fills most of the gap, but then the gas temperature increases (Fig. 2b) to the point where it is unsuitable for laser generation. Of course, for the same values of V_a and j_a of a discharge in a laser mixture containing helium, whose thermal conductivity is considerably higher than that of argon, the gas temperature is substantially lower. The calculated voltage distributions are in agreement with the experiments of Ref. 3.

For constructing a more detailed theory it is extremely important to make direct experimental measurements of the plasma density distribution, the gas temperature, and other parameters along the strip line for various amplitudes of the applied voltage and various frequencies.

[1] D. R. Hall and C. A. Hill, *Radio-Frequency Discharge Excited CO_2 Lasers* in *Handbook of Molecular Lasers*, ed. by P. K. Cheo, (Marshall Dekker, 1987).

[2] Yu. P. Raĭzer, M. N. Shneĭder, and N. A. Yatsenko, *Radio-Frequency Capacitive Discharges* (Nauka and MFTI, Moscow, 1995).

[3] A Lapucci, F. Rosetti, M. Ciofini, and J. Orlando, IEEE J. Quantum Electron. **QE-31**, 1537 (1995).

Depolarization of ferroelectrics by nanosecond electrical pulses

V. G. Gavrilyachenko, N. V. Reshetnyak, A. F. Semenchev, and A. N. Klebtsov

Scientific-Research Institute of Physics, Rostov-on-Don State University
(Submitted July 22, 1996)
Pis'ma Zh. Tekh. Fiz. **23**, 71–74 (January 26, 1997)

It is shown that the ordinary pulsed action on a ferroelectric cold cathode, which induces electron emission, results in depolarization of the ferroelectric. This phenomenon must be taken into account in the development and use of cold cathodes. © *1997 American Institute of Physics.* [S1063-7850(97)02701-8]

A large number of papers have been published dealing with electron emission from ferroelectric surfaces.[1–4] The electrons are emitted from a surface bearing a negative charge by the action of short, high-amplitude electrical pulses with a polarity opposite to the initial polarization of the sample.

The work reported here concerns a study of the stability of the state of polarization of a ferroelectric ceramic against this influence and the prospects for using these materials for cold cathodes in vacuum electron devices. The materials most effective for this purpose are of the titanium–lead zirconate system, modified with lanthanum.[1] For these experiments we chose the ferroelectric ceramic with the ratio Zr/Ti=65/35 plus 8% La.

The samples were 12 mm in diameter and 1 mm thick, poled by a field of 10 kV/cm with cooling from 150 °C through the Curie point to room temperature. The samples were then subjected to depolarizing voltage pulses from a thyratron generator, with a repetition rate and a pulse length and amplitude variable over the ranges $f=$ 20–2000 Hz, $\tau_p=100$–300 ns, and $U_p=200$–1000 V, respectively.

Measurements were made of the relative variation in the residual sample polarization as a function of the number of pulses of various amplitudes and durations. The variation in the polarization was determined by a nondestructive method using the following technique. It has been found[5] that for a polarized ferroelectric ceramic the relations between the piezoelectric modulus and the residual polarization are similar to those well known in the theory of the piezoelectric effect of ferroelectric single crystals. For the piezoelectric modulus d_{31}, which can be calculated by using the characteristic frequencies of a disk-shaped vibrator as measured by the resonance–antiresonance method,[6] this relation can be written as

$$d_{31}=Q_{12}^{*}P_r\varepsilon_{33}^{\sigma}/2\pi, \tag{1}$$

where Q_{12}^{*} is the electrostriction coefficient of the ferroelectric ceramic, P_r is the residual polarization, and $\varepsilon_{33}^{\sigma}$ is the permittivity of the free sample along the polarization axis.

The relative change in the residual polarization P_r/P_r^0 as a function of the number N of pulses can be determined from relation (1) under the assumption that Q_{12}^{*} remains unchanged:

$$P_r/P_r^0=d_{31}C^0/d_{31}^0C, \tag{2}$$

where P_r^0, d_{31}^0, and C^0 are the initial residual polarization, piezoelectric modulus, and capacitance of the sample, and P_r, d_{31}, and C are the same characteristics but after a series of N pulses. In relation (2) the ratio of the permittivities is replaced by the ratio of the capacitances, which were measured at a frequency of 1 kHz by means of a U8-2 bridge. The coefficients in relation (2) were measured at room temperature. The coercive field of the samples as determined from the dielectric hysteresis loop at room temperature is $E_c=2500$ V/cm. To check relation (2) the residual polarization was measured in a series of test experiments, both before and after the series of depolarizing pulses, by the pyroelectric current measured under short-circuit conditions when the samples were heated above the Curie temperature.

The results of our investigations are shown in Fig. 1, which displays typical curves of $(P_r/P_r^0)\sim f(N)$. One can see that the higher the values of U_p and τ_p, the faster the depolarization proceeds. We note that for a low-amplitude pulse ($U_p<500$ V), the pulse length τ_p in the range 100–300 ns has little effect on the dependence of (P_r/P_r^0) on N.

The experimental data show that during the action of pulses 100 ns or longer partial switching of the polarization occurs in the sample in individual crystallites. The number of switched crystallites accumulates with increasing N and the

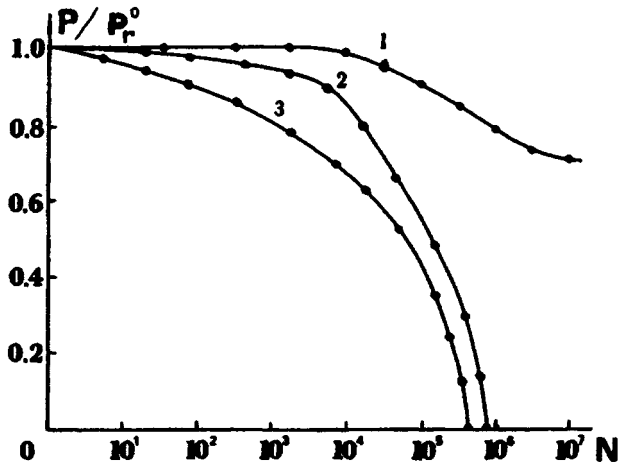

FIG. 1. Relative variation P_r/P_r^0 in the residual polarization of a ferroelectric ceramic PLZT due to the action of N pulses of reverse polarity: *1* — 500 V pulse amplitude and 100 ns pulse length; *2* — 1000 V pulse amplitude and 100 ns pulse length; *3* — 1000 V pulse amplitude and 250 ns pulse length.

 1063-7850/97/010078-02$10.00

rate of this process increases with increasing pulse amplitude and length. When a sample that has been depolarized by the short pulses has its polarization restored by cooling in a dc field through the Curie point (up to 10 polarization–depolarization cycles were investigated) the residual polarization is also restored, which indicates that the ferroelectric ceramic does not suffer any irreversible damage. It was also found that the depolarized ferroelectric ceramic can be polarized to $P_r = 0.2P_r^0$ at room temperature by 10^7 pulses of 1000 V and 100 ns long.

Our results show that ordinarily used pulsed voltages applied to a ferroelectric ceramic cold cathode to stimulate electron emission[1–4] causes depolarization of the ferroelectric ceramic, a phenomenon that must be taken into account in the development and investigation of ferroelectric ceramic cathodes.

[1] H. Gundel, J. Handerek, and H. Riege, Ferroelectrics **110**, 183 (1990).
[2] A. Sh. Aĭrapetov, A. K. Krasnykh, and I. V. Levshin, Pis'ma Zh. Tekh. Fiz. **16**(5), 46 (1990) [Sov. Tech. Phys. Lett. **16**, 182 (1990)].
[3] K. Biedrzycki and R. Le Bihan, Ferroelectrics **126**, 253 (1992).
[4] L. Schachter, J. D. Ivers, and J. A. Nation, J. Appl. Phys. **73**, 8097 (1993).
[5] E. G. Smazhevskaya and N .V. Fel'dman, *Piezoelectric Ceramics* [in Russian] (Sov. Radio, 1971).
[6] A. V. Turik and V. D. Komarov, Izv. Akad. Nauk SSSR Ser. Fiz. **34**, 2623 (1970).

Translated by J. R. Anderson

Two-feedback-loop oscillator with chaotic dynamics

É. V. Kal'yanov

Institute of Radio Engineering and Electronics, Russian Academy of Sciences, Fryazino Section, Fryazino
(Submitted October 2, 1996)
Pis'ma Zh. Tekh. Fiz. **23**, 75–79 (January 26, 1997)

This paper contains new results relating to an intensively developing field — the study of dynamic chaos. It is shown that the introduction of auxiliary wide-band feedback in an autostochastic oscillator with delay transforms chaotic oscillations into quasimonochromatic oscillations. [S1063-7850(97)02801-2]

The control of oscillations of autostochastic systems is the focus of a great deal of attention.[1] To solve this problem it appears necessary to use auxiliary feedback, a technique widely applied to generators of deterministic oscillations, which permits one to vary some of the parameters of these oscillators without degrading the other parameters.[2] No investigations have been carried out on the important problem of the effect of auxiliary feedback in generators of chaotic oscillations.

In connection with the wide use of oscillators with chaotic dynamics having delay in the feedback circuit,[3–5] it is of interest to study the possibility of using an additional feedback loop to control the oscillations of this oscillator.

This paper presents the results of theoretical investigations of an autostochastic oscillator with delay, containing an auxiliary wide-band feedback circuit with delay. It is shown possible to use this auxiliary feedback to convert the chaotic oscillations of this oscillator into regular oscillations.

The main circuit of this oscillator includes an amplifier closed in a loop, a double directional coupler, and a summing circuit. The amplifier in turn consists of series-connected delay lines, delaying the signal by a time T_1, a nonlinear element with a characteristic F, and a first-order filter with a time constant p. The useful signal is taken from the output of the direction coupler. The auxiliary feedback has a variable attenuator with a transmission coefficient d and a signal delay line with a delay time T_2. By means of the auxiliary feedback part of the signal taken from one of the outputs of the directional coupler (we shall call it the first one) is sent to a summing circuit along with the signal from the other (the second) output of the directional coupler, connected into the main feedback circuit.

Approximating the characteristic of the nonlinear element by the logistic curve,[5,6] we can write the equation describing the oscillatory process in the two-loop oscillator in the form

$$\begin{aligned} \dot{x} &= q_1 b_1 (1-b_2) y + q_2 d y_{T2}, \\ \dot{y} &= (G x_{T1} (1 + x_{T1}^n)^{-1} - y) r, \\ z &= (1-b_1)(1-b_2) y, \end{aligned} \tag{1}$$

where x and y are the oscillations at the input ($x = x(t)$) and at the output ($y = y(t)$) of the amplifier; $z = z(t)$ are the oscillations at the output of the oscillator (at the output of the directional coupler); $x_{T1} = x(t - T_1)$; $y_{T2} = y(t - T_2)$; G and n are, respectively, the gain and the nonlinearity parameter of the nonlinear element; b_1 and b_2 are the coupling coefficients for the first and second outputs of the directional coupler; q_1 and q_2 are the weighting factors of the summing circuit, and $r = 1/p$. The overdot denotes differentiation with respect to the time t.

The system of nonlinear differential-difference equations (1) were solved by the Runge-Kutta-Merson 4th order method. The results of the solution are illustrated in Figs. 1 and 2.

Figure 1 displays the bifurcation diagrams showing the variation in the maximum values of the oscillatory process, $z(t)$ (denoted by $[z(t)]$) versus the parameter that determines the transmission of the signal in the auxiliary feedback circuit. The bifurcation diagrams were obtained for an increase in the parameter d from 0 to 1, for $n = 6$ (Fig. 1a), and $n = 12$ (Fig. 1b), while the values of the rest of the parameters are $G = 32$, $p = 0.5$, $T_1 = 3$, $T_2 = 1.5$, $b_1 = b_2 = q_1 = q_2 = 0.5$. The value of the nonlinearity parameter, $n = 6$, corresponds to the derivative of the descending part of the characteristic in the region of its maximum steepness, equal to 52. This value of the derivative for $n = 12$ corresponds to the value 125.

As can be seen, for $n = 6$ and in the interval $d \in (0;0.52)$ there is a chaotic scatter of maximum values of the oscillatory process, which indicates the chaotic nature of the oscillations in this interval of the parameter d. For $d > 0.52$ the oscillations cease to be stochastic; then we observe regular variations in the maximum values of the oscillatory process with increasing parameter that determines the transmission of the signal in the auxiliary feedback circuit.

When the variation of the parameter d is reversed (decreasing from 1 to 0), hysteresis is observed and the region of deterministic oscillations is extended to lower values of d.

The characteristic attractors corresponding to the values $d = 0$ and $d = 1$ in the bifurcation diagram in Fig. 1a are shown in Fig. 2a and Fig. 2b, respectively. They were obtained in a projection on the plane $\{z(t), z(t-T)\}$ (for $T = T_1 + T_2$) in the time interval $t \in (160;200)$. In the chaotic oscillations the motions are entangled and the attractor is mapped by a complicated unclosed curve. Where the oscillations cease to be stochastic the self-oscillations have a relatively simple limit cycle.

For $n = 12$, Fig. 1b shows that the interval of values of d corresponding to chaotic oscillations is compressed into the region $d \in (0;0.32)$. The nature of the chaotic and regu-

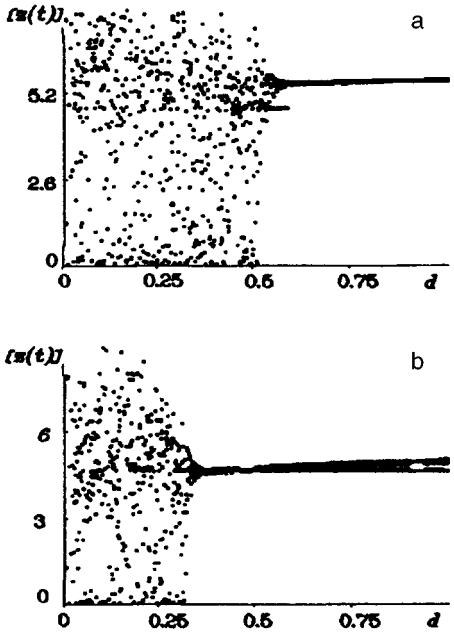

FIG. 1. Bifurcation diagram for $n=6$ (a) and $n=12$ (b).

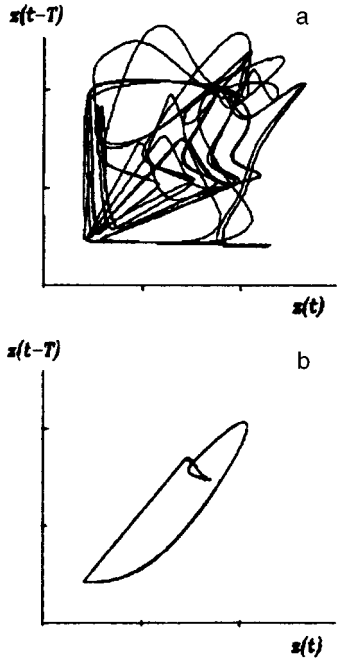

FIG. 2. Attractors of the oscillations for one (a) and two (b) delay feedback loops.

lar motions are similar to the attractors shown in Fig. 2.

Compression of the range of d corresponding to chaotic oscillations is observed with further increase in n. Conversely, for smaller values of n, for example, for $n=4$, the chaotic oscillations persist over the entire range of d from 0 to 1. This indicates a seemingly paradoxical situation where the destochastization with the aid of an auxiliary feedback circuit is effective for relatively larger nonlinearities.

It should be noted that if, for an appropriate choice of delay T_1 and for $d=0$, regular oscillations are generated, then regimes are possible where chaos can be induced by means of an auxiliary feedback loop. The choice of the delay T_2 is the important factor. This effect, inverse to that described, is also of practical interest.

These investigations indicate that the operation of an oscillator with two delaying feedback loops is more effective than with a single loop. The auxiliary feedback permits control of the oscillations of a generator with delay.

This work was carried out with the support of the Russian Fund for Fundamental Research (Grant No. 95-02-04300).

[1] V. V. Astakhov, A. V. Shabunin, A. N. Silchenko *et al.*, *The International Conference on Nonlinear Dynamics and Chaos. Applications in Physics, Biology, and Medicine*, ICND-96. Saratov, Russia, July 8–14, 1996, Book of Abstracts. P. 23.
[2] V. N. Yakovlev, *Oscillators with Multiple Feedback Loops* [in Russian] (Svyaz', Moscow, 1973).
[3] A. S. Dmitriev and V. Ya. Kislov, *Stochastic Oscillations in Radio Physics and Electronics* [in Russian] (Nauka, Moscow, 1989).
[4] V. A. Kats and D. I. Trubetskov, JETP Lett. **39**, 137 ((1984).
[5] É. V. Kal'yanov, Pis'ma Zh. Tekh. Fiz. **21**(18), 68 (1995) [Tech. Phys. Lett. **21**, 756 (1995)].
[6] L. Glass and M. C. Michael, *From Clocks to Chaos: The Rhythms of Life* (Princeton University Press, Princeton NJ, 1988) [Mir, Moscow, 1991].

Translated by J. R. Anderson

Increasing the concentration of recombination impurities as a means to suppress the amplification saturation effect in intrinsic threshold photoresistors with extracting contacts and impurity recombination of photo-generated carriers

V. A. Kholodnov and A. A. Drugova

Theoretical Division of the State Scientific Center of the Russian Federation, State Enterprise NPO ''Orion,'' Moscow

(Submitted November 5, 1996)
Pis'ma Zh. Tekh. Fiz. **23**, 80–87 (January 26, 1997)

It is shown possible to avoid the well-known deleterious properties of intrinsic photoresistors with extracting electrodes—gain saturation with increasing electric field. The gain saturation severely limits the photosensitvity of the device. This limitation is removed if the extracting electrodes are replaced with blocking electrodes, but this procedure is technologically very difficult to execute, and the method does not submit to reliable control. The possibility of avoiding saturation under conditions of a simultaneously large increase in the lifetime of the photogenerated carriers is of considerable interest for experimenters and for developers of photodetectors. © *1997 American Institute of Physics.* [S1063-7850(97)02901-7]

Intrinsic photoresistors, i.e., those that operate on the principle of interband absorption of radiation, are used as efficient photodetectors with internal gain, and in many cases the dominant channel for the recombination of photocarriers in the bulk of the photoresistor is through the trapping of these carriers at deep impurity levels.[1–8] To obtain gain the device requires an electric field E such that the lifetime τ_p of the photo-induced holes (or that of the photoinduced electrons, τ_n), must exceed the corresponding travel time, $t_p = W/\vartheta_p$ (or $t_n = W/\vartheta_n$) through the distance W between the contacts, where $\vartheta_p = \mu_p E$ and $\vartheta_n = \mu_n E$ are the hole and electron drift velocities, and μ_p and $\mu_n = b\mu_p$ are their mobilities. The photoelectric gain $I_{ph}/(qWg)$ (Ref. 5), where I_{ph} and g are the photocurrent density and the rate of carrier photogeneration and q is the electron charge, is strongly influenced by the recombination rate of the photocarriers at the current contacts ($x=0$ and $x=W$). It would, of course, be desirable that recombination not occur there at all (blocking contacts[9,10]), but making such ideal contacts is far from a simple matter, and for each particular situation the conditions on the contacts are not known reliably.

The other limiting case is more realistic: The photoelectron concentration $\Delta n(x) = n - n_e$ and the photohole concentration, $\Delta p(x) = p - p_e$ vanish at the contacts (extracting contacts[3,11,12]), where $n(x)$ and $p(x)$ are the electron and hole concentrations and n_e and p_e are their equilibrium concentrations. The undesirable property common to intrinsic photoresistors with extracting contacts is well known: gain saturation.[3,4,11,12] The saturation involves the following. When E is increased, the value of G at first increases and then if $t_n < \tau_n$ and $t_p < \tau_p$, the gain ceases to depend on E as long as field heating of the carriers is unimportant.

In papers[13] at an international symposium (USA) we have discussed the possibility of suppressing this undesirable effect in intrinsic threshold photoresistors with impurity carrier recombination by increasing the concentration N of recombination impurities In the present paper we present a brief mathematical basis for this possibility.

Let us assume that the recombination impurity is an acceptor in a neutral or a minus-one charge state, with the atom concentration equal to N_0 and $N_- = N - N_0$. The neutral atoms trap the electrons with a probability w_n and thermally generate holes, while the charged atoms trap holes with a probability w_p and thermally generate electrons, which corresponds to a single recombination level,[14–16] which frequently is the dominant level.[5–8,17,18] Let us assume that there are also shallow, completely ionized donors with a concentration N_D. Under these conditions the following relation holds[19–21]

$$N = n_t \frac{1+\delta}{2\delta^2} f(\delta), \tag{1}$$

where

$$\delta = \frac{N_-^e}{N_0^e}, \quad f(\delta) = B + A\delta - \delta^2,$$

$$A = 2\frac{N_D}{n_t}, \quad B = 4\frac{p_t}{n_t}, \tag{2}$$

N_-^e and N_0^e are the equilibrium concentrations of charged and neutral recombination centers and n_t and p_t are the equilibrium concentrations of electrons and holes when the recombination level lines up with the Fermi level.

As threshold photodetectors, photoresistors operate under very low illumination. Therefore in calculating G correctly, the approximation linear in g is usually used in the theory of threshold photodetectors.[3,4,22,23] Under these conditions, the expressions for the electron component

$$\Delta I_n = q\mu_n(E\Delta n + n_e \Delta E) + qD_n \frac{d\Delta n}{dx} \tag{3}$$

and the hole component

$$\Delta I_p = I_{ph} - \Delta I_n = q\mu_p(E\Delta p + p_e \Delta E) - qD_p \frac{d\Delta p}{dx} \tag{4}$$

of I_{ph} imply that for a given voltage on the photoresistor we have

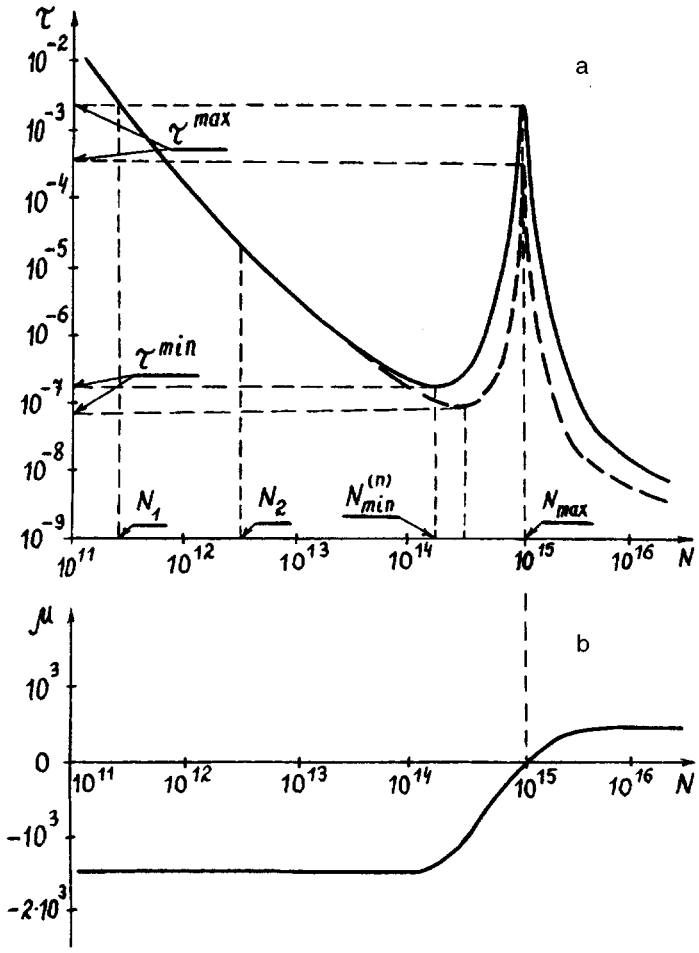

FIG. 1. Dependence of the electron lifetime $\tau_n\langle$—$\rangle$ and hole lifetime $\tau_p\langle$ - - - $\rangle$ in seconds (a) and ambipolar carrier mobility μ in $cm^2/V\cdot$ s (b) on the concentration N of recombination centers, in cm^{-3}, at room temperature. The specific example chosen was silicon. The following values were adopted: $\mu_n=1500$ $cm^2/V\cdot s$, $\mu_p=450$ $cm^2/V\cdot s$, the intrinsic carrier concentration is $n_i=1.45\times10^{10}$ cm^{-3}, $w_n=10^{-8}$ cm^3/s, $\theta=10^2$ (Refs. 8, 17, 18, and 22); $n_i/n_t=10^2$, and $N_D=10^{15}$ cm^{-3}.

$$I_{ph}=q(\vartheta_n\langle\Delta n\rangle+\vartheta_p\langle\Delta p\rangle), \tag{5}$$

where $\Delta E(x)$ is the deviation of the electron field from its value E in the absence of illumination, D_n and D_p are the diffusion coefficients of electrons and holes, and

$$\langle\Delta n\rangle=\frac{1}{W}\int_0^W\Delta n(x)dx,\quad \langle\Delta p\rangle=\frac{1}{W}\int_0^W\Delta p(x)dx. \tag{6}$$

From the linearized relations for the recombination-generation rates for electrons, R_n, and for holes, R_p (Refs. 16 and 21), and from the conditions for steady-state operation, $R_n=R_p$, the equations of continuity of the electron and hole currents, the linearized Poisson equation,[21] and expressions (3) and (4), we can obtain a (fourth order) equation for the distribution $\Delta n(x)$. As a rule, the following inequality holds

$$\frac{\varepsilon w_n}{4\pi q\mu_n}\ll\min\{1,\delta\}, \tag{7}$$

where ε is the permittivity, which for $n,\ p\ll N$, can be interpreted as the condition for screening of the space charge by impurity centers.[5,7,8] The inequality (7) lets us convert this equation to a second order equation familiar (in form) from the theory of photoresistors

$$D\frac{d^2\Delta n}{dx^2}+\mu E\frac{d\Delta n}{dx}-\frac{\Delta n}{\tau_n}+g=0, \tag{8}$$

in which

$$\frac{1}{\tau_n}=w_p n_t\frac{f(\delta)}{2\delta^2}\frac{\delta A+(2+\delta)B+\delta^3}{\theta f(\delta)+(1+\delta)(\theta B+\delta)},\quad \theta=\frac{w_p}{w_n}, \tag{9}$$

the ambipolar carrier mobility is

$$\mu=\frac{B\tau_n-\delta^2\tau_p}{(B+b\delta^2)\tau_n}\mu_n, \tag{10}$$

$$\frac{1}{\tau_p}=w_p n_t\frac{f(\delta)}{2\delta}\frac{\delta A+(2+\delta)B+\delta^3}{B+(A+\theta B)\delta+(\theta B+\delta)\delta^2}, \tag{11}$$

the bipolar carrier diffusion constant is

$$D=\frac{(B\tau_n+\delta^2\tau_p)D_n+\varkappa\varepsilon(4\pi q)^{-1}w_p\tau_n\tau_p E^2}{(B+b\delta^2)\tau_n}, \tag{12}$$

$$\varkappa=(1+\delta)f(\delta)\left[\frac{\delta}{\theta f(\delta)+(1+\delta)(\theta B+\delta)}+\frac{B}{B+(A+\theta B)\delta+(\theta B+\delta)\delta^2}\right], \tag{13}$$

and in the expressions for R_n and R_p (Ref. 21) we neglect the terms containing the derivative of ΔE with respect to x and thereby write $\tau_n\Delta p(x)=\tau_p\Delta n(x)$. From the solution of Eq. (8) and relations (5) and (6), we find that under the conditions considered here

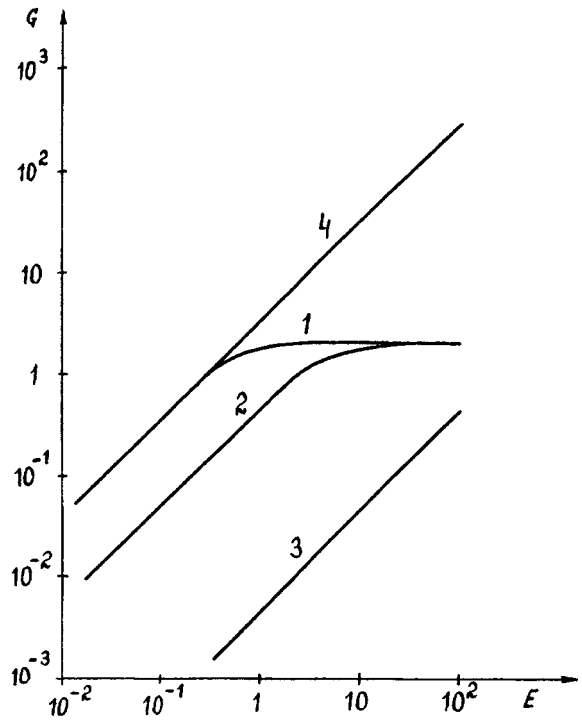

FIG. 2. Dependence of the photoelectric gain G on the electric field E, in V/cm at room temperature. The specific example chosen was silicon. The following values were adopted: *1*—$N=N_1$, *2*—$N=N_2$, *3*—$N=N_{\min}^n$, *4*—$N=N_{\max}\simeq N_D$ (Fig. 1a). $\mu_n=1500$ cm^2/V·s, $\mu_p=450$ cm^2/V·s, the intrinsic carrier concentration is $n_i=1.45\times10^{10}$ cm^{-3}, $w_n=10^{-8}$ cm^3/s, $\theta=10^2$ (Refs. 8, 17, 18, and 22); $n_i/n_t=10^2$, $N_D=10^{15}$ cm^{-3}, and W$=10^{-1}$ cm.

$$G=\left(\frac{\tau_n}{t_n}+\frac{\tau_p}{t_p}\right)\times\left\{1-4\frac{L}{W}\sqrt{\left(\frac{l}{2L}\right)^2+1}\,\frac{\sinh\left(\frac{W}{2L_1}\right)\sinh\left(\frac{W}{2L_2}\right)}{\sinh\left(\frac{W}{2L_1}+\frac{W}{2L_2}\right)}\right\}, \tag{14}$$

where $l=\mu\tau_nE$ and $L=\sqrt{D\tau_n}$ are the bipolar drift and diffusion lengths of the carriers, while their inverse bipolar diffusion-drift lengths are

$$\frac{1}{L_{1,2}}=\mp\frac{l}{2L_2}+\sqrt{\left(\frac{l}{2L^2}\right)^2+\frac{1}{L^2}}. \tag{15}$$

Relations (1), (2), and (9)–(15) determine in parametric form the function $G(N)$. The lifetimes τ_n and τ_p can be highly nonmonotonic functions of N (Fig. 1a).[20,21,23,24]. This is true when[20,21]

$$\xi_1\equiv\frac{1}{\sqrt{A}}\ll1,\quad \xi_2\equiv\frac{\sqrt{B}}{A}\ll1,\quad \xi_3\equiv\frac{3}{\theta B}\ll1,\quad \xi_4\equiv\frac{4B}{A^2}\ll1. \tag{16}$$

An analysis of expressions (1), (2), and (9)–(11) shows that μ goes to zero for some values of N (Fig. 1b) if the inequality (16) is satisfied. An important point is that it coincides with N in zero order in the small parameters (16) equal to N_D,[20,21] for which $\tau_n=\tau_n^{\max}$ and $\tau_p=\tau_p^{\max}$ (Fig. 1a). Therefore, as follows from Eq (14), the maximum gain $G_{\max}$ is obtained not for small $N\ll N_D$ as one might think, but for $N=N_D$, where, in contrast to the case $N\ll N_D$, we find that $G_{\max}\propto E$ (Fig. 2) up to very high fields E, where by virtue of the dependence $D(E)$ due to photoexcitation of space charge, even though small, the inequality $L<W$ may no longer hold. However, a separate analysis is required to demonstrate if this situation is realistic.

We wish to thank the Russian Fund for Fundamental Research for supporting this work. (Grant No. (96-02-17196).

[1] P. M. Downey, R. J. Martin *et al.*, Appl. Phys. Lett. **46**, 396 (1985).
[2] R. Loepfe, A. Schaelin *et al.*, Appl. Phys. Lett. **52**, 2130 (1988).
[3] *Optical and Infrared Detectors*, ed. by R. J. Keyes (Springer-Verlag, Berlin, 1977) [Russ. transl., Radio i Svyaz', Moscow, 1985).
[4] A. Rogalski *et al.*, *Infrared Photon Detectors*. Bellingham Washington, USA: (SPIE Optical Engineering Press, 1995).
[5] A. Rose, *Concepts in Photoconductivity and Allied Problems* (Interscience, New York, 1963) [Russ. transl., Mir, Moscow, 1966].
[6] R. H. Bube, *Photoconductivity of Solids* (Wiley, New York, 1960) [Russ. transl., IL, 1962).
[7] S. M. Ryvkin, *Photoelectric Phenomena in Semiconductors* (Fizmatgiz, Moscow, 1963).
[8] A. G. Milnes, *Deep Impurities in Semiconductors* (Wiley, New York, 1973) [Russ. transl, Mir, Moscow, 1977].
[9] D. L. Smith, J. Appl. Phys. **56**, 1663 (1984).
[10] Y. J. Sacham-Diamand and I. Kidron, Infrared Phys. **21**, 105a (1981).
[11] D. L. Smith, F. K. Lo, and J. D. Genova, J. Vac. Sci. Technol. **21**, 259 (1982).
[12] C. T. Elliott, in *Handbook on Semiconductors*, ed. by C. Hilsum (North-Holland, Amsterdam, 1982), Vol. 4, pp. 727–798.
[13] A. A. Drugova and V. A. Kholodnov, *Proceedings of the International Semiconductor Device Research Symposium*, Charlottesville, USA, 1995, Vol. 1, pp. 197–200.
[14] R. N. Hall, Phys. Rev. **87**, 387 (1952).
[15] W. Shockley and W. T. Read, Phys. Rev. **87**, 835 (1952).
[16] V.V. Osipov and V. A. Kholodnov, Fiz. Tekh. Poluprovodn. **4**, 2241 (1970) [Sov. Phys. Semicond. **4**, 1932 (1970)].
[17] R. A. Smith, *Semiconductors* (Cambridge University Press, Cambridge, 1959) [Russ. transl., Mir, Moscow, 1982].
[18] J. S. Blakemore, *Solid State Physics*, 2nd ed. (Pergamon Press, Oxford, 1962) [Russ. transl, Mir, Moscow, 1988].
[19] V. A. Kholodnov, *Theory of Injection Phenomena in Compensated Semiconductors*, Dis. na Soisk. Dokt. Fiz.-Material Nauk, Moscow, MFTI, 1973.
[20] A. A. Drugova and V. A. Kholodnov, Solid State Electron. **38**, 1247 (1995).
[21] V. A. Holodnov, Fiz. Tekh. Poluprovodn. **30**, 1011 (1996) [Semiconductors **30**, 538 (1996)].
[22] W.T. Tsang (ed.), *Semiconductors and Semimetals*, Vol. 22, Pt. D, *Lightwave Communication Technology: Photodetectors* (Academic Press, New York 1985) [Mir, Moscow, 1988].
[23] V. A. Kholodnov, *Theory of Threshold Semiconductor Photodetectors with Internal Amplification*, Dis. na Soisk. Dokt. Fiz.-Mat. Nauk. Moscow, Scientific Research Institute, Applied Physics, NPO ''Orion'' 1990.
[24] A. A. Drugova and V. A. Kholodnov, Pis'ma Zh. Tekh. Fiz. **18**(1), 23 (1992) [Sov. Tech. Phys. Lett. **18**, 8 (1992)].

Translated by J. R. Anderson

Formation of acoustooptical bound states by optical pulses

A. S. Shcherbakov and I. B. Pozdnov

St. Petersburg State Technical University
(Submitted November 4, 1996)
Pis'ma Zh. Tekh. Fiz. **23**, 88–95 (January 26, 1997)

An interesting aspect of the acoustooptical interaction is studied in this paper — the formation of acoustooptical bound states by optical pulses. An analysis is made of the solution of a system of three nonlinear partial differential equations describing the case of collinear acoustooptical interaction. A specific example of this solution is examined for the case of the interaction of a sequence of acoustic pulses with a digital sequence of optical pulses. It is shown that the values of the recorded sequences of scattered light correspond to the logical operation ''AND'' operating on the sequence of acoustic and optical pulses, that is, a programmable switching of the input optical digital signal by a sequence of acoustic pulses occurs. The experiment reported in this paper corresponds to the case of detuning of the wave vectors, but on the whole it supports the calculations In summary, this work demonstrates (experimentally and theoretically) the possibility of realizing an optoelectronic programmable switching of optical signals. [S1063-7850(97)03001-2]

The theoretical and experimental study of the formation of acoustoopticalal bound states with a time-independent amplitude of the incident optical wave[1,2] has motivated the development of a new class of optoelectronic devices, digital modulators-converters,[3,4] based on collinear acoustooptical interaction. However, the acoustooptical bound states may also be formed by means of optical pulses. In this work the pulsed regime is investigated for the cases of strong and weak coupling, and the possibility of using the bound states for acoustooptical programmable switches of digital sequences of optical pulses is examined.

The collinear acoustooptical interaction in an optically anisotropic medium is described by a system of three partial differential equations containing a quadratic nonlinearity

$$\frac{\partial U}{\partial x}+\frac{1}{V_0}\frac{\partial U}{\partial t}=-\gamma_u a_p a_s^* \exp(i\Delta k x),$$

$$\frac{\partial a_s}{\partial x}+\frac{1}{c_s}\frac{\partial a_s}{\partial t}=-\gamma_s a_p U^* \exp(i\Delta k x), \quad (1)$$

$$\frac{\partial a_p}{\partial x}+\frac{1}{c_p}\frac{\partial a_p}{\partial t}=\gamma_p a_s U \exp(-i\Delta k x), \quad (1)$$

where U, a_p, a_s, and V_0, c_p, and c_s are the complex amplitudes and the group velocities of the acoustic wave and the incident and scattered optical waves; γ_u, γ_p, and γ_s are the acoustooptical interaction constants, determined by the properties of the medium,[5] and Δk is the detuning of the wave vectors.

Let us consider first the case where the condition of phase synchronism of the interacting waves is fulfilled exactly, $\Delta k=0$. Assuming that the rates of change of the envelopes are the same and the group velocities of the acoustic and optical waves are incommensurate, $V_0 \ll c_p$, c_s, we shall use an analysis that is simplified from that of Refs. 6 and 7, and as in Refs. 8 and 9 neglect the terms in the partial derivatives with respect to the time in the second and third equations of the system (1). Then using the following substitutions, $a_p=A_0 \cos\psi/2$, $a_s=A_0\gamma_s^{1/2}\gamma_p^{-1/2}\sin\psi/2$, and $U=-(1/2)(\gamma_s\gamma_p)^{-1/2}\partial\psi/\partial x$ and transforming to the new system of coordinates, $z=A_0(\gamma_s\gamma_u)^{1/2}x$ and $\tau=A_0(\gamma_s\gamma_u)^{1/2}(2V_0t-x)$, where A_0 is the peak amplitude of the incident optical wave for $x\to-\infty$, we reduce the system of equations (1) to a sine-Gordon equation in the variable ψ. We consider only those solutions of this equation which in the laboratory system of coordinates (x,t) are described by the stationary localized envelope pulses. In particular, this requirement corresponds to a single-soliton solution of the sine-Gordon equation:[10]

$$\psi=4\tan^{-1}\left[\gamma \exp\left(\frac{z-\beta\tau}{\sqrt{1-\beta^2}}\right)\right], \quad (2)$$

where the factor $(1-\beta^2)^{1/2}$ gives the Lorentz contraction of the spatial dimensions of the pulse when it moves with a velocity β in the (z,τ) coordinate system $|\beta|<1$, γ is an arbitrary constant that determines the spatial displacement of the center of the soliton when it is formed; we set $\gamma=1$. Carrying out the inverse transformation to the initial field variables in the laboratory coordinate system, we obtain an expression for the amplitude of the acoustic wave

$$U=-U_0 \operatorname{sech}[U_0(\gamma_s\gamma_p)^{1/2}(x-Vt)], \quad (3)$$

where U_0 is the peak amplitude of the acoustic pulse, and $V=V_0(1-A_0^2\gamma_u U_0^{-2}\gamma_p^{-1})$ is the velocity of the tightly bound state in the laboratory frame. One can see from Eq. (3) that the spatial extent x_0 of the bound state and the peak amplitude U_0 of the acoustic pulse are related by the expression characteristic of a soliton, $x_0U_0=(\gamma_s\gamma_p)^{-1/2}$, which is a constant determined only by the properties of the anisotropic medium. Here the expressions for the amplitude of the incident and scattered optical waves are

$$a_p=-A_0 \tanh[x_0^{-1}(x-Vt)],$$

$$a_s=A_0\sqrt{\frac{\gamma_s}{\gamma_p}} \operatorname{sech}[x_0^{-1}(x-Vt)]. \quad (4)$$

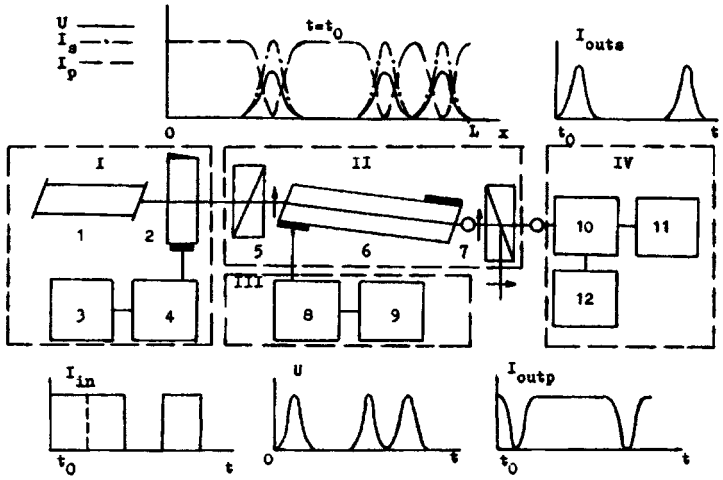

FIG. 1. Dynamics of the formation of optical digital sequences and experimental arrangement: U is the sequence of acoustic pulses in the medium, I_{in} is the input sequence of optical pulses, $I_{\text{out}\,p}$ and $I_{\text{out}\,S}$ are the sequences corresponding to the transmitted and scattered optical waves at the exit boundary of the medium at $X=L$. *I*—Unit for forming the input optical digital signal (*1*—laser, *2*—acoustooptical modulator, *3*—rf oscillator, *4*—digital sequence generator); *II*—switch (*5*—polarizer, *6—collinear acoustooptical cell*, *7*—analyzer); *III*—unit for forming the electronic digital signal (*8*—rf oscillator, *9*—digital sequence generator); *IV*—unit for recording the output signal from the switch (*10*—photomultiplier, *11*—oscilloscope, *12*—photomultiplier power supply).

Expressions (3) and (4) describe the acoustooptical tightly-bound state, whose velocity of propagation and spatial extent are completely determined by the peak amplitudes of the interacting waves.

The formation of an acoustooptical bound state is possible only when the acoustic wave and the incident optical wave are present simultaneously in the interaction region, and each can be equally well be described as the parameter that turns on or controls the interaction. This circumstance allows us to use the effect to form an acoustooptical bound state by optical pulses for programmable switching of an input optical digital signal represented by the incident optical wave, and by an electronic digital signal, excited in the medium by a binary sequence of acoustic pulses. If a sequence of optical pulses

$$U(x\cdot t)=U_0\sum_{k=0}^{N-1} b_k\ \mathrm{sech}[(V_0\tau)^{-1}(x-V_0(t-kT))] \tag{5}$$

propagates in the medium, where N is the number of digits in the digital number determining the sequence of the switching; $b_k\in\{0,1\}$, τ is the length of the pulses, and T is the repetition period of the pulses, which is chosen so that the area of overlap of the adjacent sech-shaped envelopes is sufficiently small. At the time t_0 a digital sequence of optical pulses of the same number of digits and a rectangular envelope is introduced into the medium with an intensity

$$I_{\text{in}}=A_0^2\sum_{l=0}^{N-1} d_l\theta(t-t_0-lT)\,\theta(lT+t_0+T-t),$$

$$\theta(x)=\begin{cases}0, & x<0;\\ 1, & x\geqslant 0,\end{cases} \tag{6}$$

where the duration of the optical pulses is taken equal to the period T. Because of the condition $V_0\ll c_p,c_s$, the spatial extent of each optical pulse is much greater than that of the entire acoustic sequence. The reduction scheme used the system of equations (1) above is equivalent to neglect of the transient processes with characteristic times of the order of $TV_0c_{s,p}^{-1}\lesssim 10^{-10}$ s. We can therefore assume that at each instant of time the acoustic sequence interacts with only a single optical pulse, whose intensity at the entrance to the medium is determined by the corresponding value of d_l. As a rule, the condition $\gamma_s\gamma_u A_0^2\ll\gamma_s\gamma_p U_0^2$ is satisfied experimentally, where $V=V_0$. In correspondence with the initial acoustic sequence (5) and the sequence of input optical pulses (6), a sequence of acoustooptical bound states is formed in the medium, whose scattered optical component is given by the relation

$$a_s^2=A_0^2\frac{\gamma_s}{\gamma_p}\sum_{l=0}^{N-1} d_l\theta(t-t_0-lT)\,\theta(lT+T+t_0-t)$$
$$\times\sum_{k=0}^{N-1} b_k\ \mathrm{sech}^2[(V_0\tau)^{-1}(x-V_0(t-kT))]. \tag{7}$$

If t_0 corresponds to the time when the leading edge of the first acoustic pulse, representing the digit in the first place, reaches the exit boundary of the medium, i.e., the point of observation $x=L$, where L is the length of the interaction medium, then at that point one observes a digital optical sequence of the form

$$I_{\text{out}\,S}=A_0^2\frac{\gamma_s}{\gamma_p}\sum_{k=0}^{N-1} g_k\ \mathrm{sech}^2[(V_0\tau)^{-1}(L-V_0(t-kT))],$$

$$I_{\text{out}\,p}=A_0^2-I_{\text{out}\,S}.$$

The values of the kth place of the number g are determined by the logical operation ''AND,'' carried out at the k-th place of the numbers b and d: $g_k=b_k\wedge d_k$. As a result of the interaction of the digital acoustic and optical sequences we obtain a programmable switching of the input optical digital signal by a sequence of acoustic pulses previously introduced into the medium. The efficiency of switching is governed by the efficiency of formation of the bound state[2] and in the present case is equal to $\eta=\gamma_s\gamma_p^{-1}$. Numerical estimates for acoustooptical cells based on α-quartz show switching of an optical digital signal with a 4-μs pulse length requires an acoustic power of 100 W/cm^2. Attaining such high acoustic powers experimentally presents definite difficulties. However, it is possible to reduce considerably the necessary acoustic power density by resorting to the formation of acoustooptical weakly bound states with wave-vector detuning;[2] in this way the functional principle of the

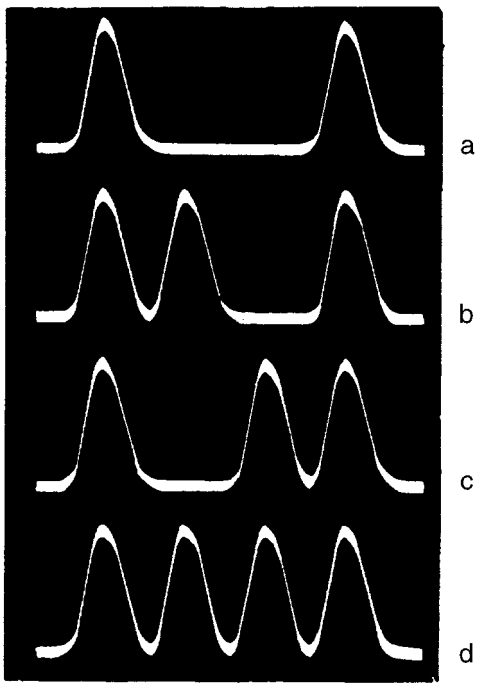

FIG. 2. Examples of oscilloscope traces of digital optical sequences at the switch output ($b \wedge d = g$): a—1011 $\wedge$ 1101 = 1001; b—1111 $\wedge$ 1101 = 1101, c—1011 $\wedge$ 1111 = 1011, d—1111 $\wedge$ 1111 = 1111.

switch is maintained. In the case of weak coupling the formation of bound states in a medium requires the excitation of a sequence of pulses of the same number of digits N but, unlike the case of expression (5), in rectangular form:

$$U(x,t) = U_c \sum_{k=0}^{N-1} b_k \theta\,[x - V_0(t-kT)]\theta \times [V_0(t-kT-\tau_c) - x],$$

where the duration τ_c of the square pulses is related by the localization condition to their amplitude U_c and the detuning of the wave vector, Δk.[2] The output signals of the switch based on acoustooptical weakly bound states is given by the expressions

$$I_{\text{out } S} = A_0^2 \eta \sum_{k=0}^{N-1} g_k \theta\,[L - V_0(t-kT)]\theta \times [V_0(t-kT-\tau_c) - L]\sin^2\{(\tau_c V_0)^{-1}\pi \times [L - V_0(t-kT)]\},$$

$$I_{\text{out } p} = A_0^2 - I_{\text{out } S}.$$

The efficiency η of switching is determined by the efficiency of formation of the weakly bound states.[2] The detuning of the wave vectors permits an experimental investigation of the switch based on the acoustooptical bound states. A diagram of the experiment with a prototype of the switch and a timing diagram are shown in Fig. 1. In the experiments we studied the formation of acoustooptical weakly bound states by optical pulses and examined the optoelectronic programmable switching of a 4-place optical signal at a wavelength 0.63 μm and a 4 μs pulse length by electronic (acoustic) pulses of the same length. The switch used a collinear acoustooptical cell made of α-quartz with a time aperture of 20 μs ($L = 9$ cm). In Fig. 2 we show an oscilloscope trace of the signal $I_{\text{out } S}$ in RZ code, corresponding to different numbers b and d, in one of the output channels of the switch. The efficiency of the switching was 4% with an acoustic power density of 1 W/cm^2 at a carrier frequency of 54 MHz and a frequency detuning of 0.25 MHz.

To summarize, we have studied the formation of acoustooptical bound states of optical pulses for both strong and weak coupling. The possibility of localization of the optical component of the bound state by means of optical input pulses and of using this effect for optoelectronic programmable switching of optical digital signals has been demonstrated experimentally.

[1] O. I. Belokurova and A. S. Shcherbakov, Pis'ma Zh. Tekh. Fiz. **15**(18), 1 (1989) [Sov. Tech. Phys. Lett. **15**, 703 (1989)].
[2] A. S. Shcherbakov and I. B. Pozdnov, Pis'ma Zh. Tekh. Fiz. **20**(17), 12 (1994) [Tech. Phys. Lett. **20**, 687 (1994)].
[3] A. S. Shcherbakov and I. B. Pozdnov, Pis'ma Zh. Tekh. Fiz. **21**(4), 31 (1995) [Tech. Phys. Lett. **21**, 144 (1995)].
[4] A. S. Shcherbakov and I. B. Pozdnov, Photonics and Optoelectronics **2**(2), 87 (1994).
[5] V. I. Balakshiı, V. N. Parygin, and L. E. Chirkov, *The Physical Principles of Acoustoopticals* [in Russian] (Radio i Svyaz', Moscow, 1985).
[6] R. K. Dodd, J. C. Eileck, J. Gibbon, and H. C. Morris, *Solitons and Nonlinear Wave Equations* (Academic Press, New York, 1982) [Russ. transl., Mir, Moscow, 1988].
[7] A. S. Shcherbakov and O. I. Belokurova, Proc. SPIE **1807** (Photonic Switching), pp. 368–381.
[8] G. N. Burlak and N. Ya. Kotsarenko, Pis'ma Zh. Tekh. Fiz. **10**, 674 (1984) [Sov. Tech. Phys. Lett. **10**, 284 (1984)].
[9] O. I. Belokurova and A. S. Shcherbakov, Pis'ma Zh. Tekh. Fiz. **16**(16), 29 (1990) [Sov. Tech. Phys. Lett. **16**, 612 (1990)].
[10] G. L. Lamb, Jr., *Elements of Soliton Theory* (Wiley, New York, 1980) [Russ. transl., Mir, Moscow, 1983].

Translated by J. R. Anderson

Measurement of the amount of free and bound hydrogen in amorphous carbon

O. I. Kon'kov, I. N. Kapitonov, I. N. Trapeznikova, and E. I. Terukov

A. F. Ioffe Physicotechnical Institute, Russian Academy of Sciences, St. Petersburg
(Submitted October 24, 1996)
Pis'ma Zh. Tekh. Fiz. **23**, 3–8 (January 12, 1997)

The effusion of hydrogen and other gases from an amorphous carbon *a*-C:H film annealed at temperatures of 100–1000°C was studied. A direct method was used to determine the amount of hydrogen in the material as 26 at.%. The amount of free hydrogen was determined as 4 at.%. The temperature curve for the release of free hydrogen gas has a maximum at 400 °C. A broad hydrogen effusion peak was observed above 400 °C. The amount of hydrogen released by breaking of weak C–H bonds was determined as 10 at.% and that released by breaking of strong C–H bonds was determined as 12 at.%.
[S1063-7850(97)00101-8]

The synthesis and physical properties of amorphous carbon (*a*-C:H) films have been studied fairly extensively but the mechanisms for formation of the structure of these films and their correlation with the observed physical properties are still not fully understood. Depending on the method of growth, *a*-C:H films may contain appreciable quantities of free and bound hydrogen. The hydrogen content is a key factor determining the structure of the films and defining their physical properties. Thus the spectroscopy of hydrogen in *a*-C:H films is an extremely pressing problem.

Infrared spectroscopy is the conventional optical method of studying bound hydrogen. This can be used to determine the type of binding of the carbon and hydrogen atoms in the films, their concentration, and the degree of hybridization.[1] However, it has recently been shown that this method cannot be used to detect some sp^2-hybridized carbon atoms or to estimate the total quantity of hydrogen in the film.[2] Preliminary data indicate that between one third and one half of the incorporated hydrogen is not bound with carbon atoms but is trapped in interstitial sites and is in atomic or molecular form.

In the present paper we use a direct method to investigate the state of hydrogen in *a*-C:H films, by studying the effusion of hydrogen from the film material as a function of temperature.

The samples were grown by rf decomposition of a methane–hydrogen mixture in a capacitive reactor on crystalline silicon substrates. A preliminary description of the films was given in Ref. 3.

A method of stepwise heating in vacuum was used to investigate the release of the gaseous component from the films as a function of temperature. We used an entirely metal extraction system with an externally heated furnace and calibrated expansion volumes. The total quantity of released gases was determined by a manometric technique. The hydrogen was then removed from the system by diffusion through a palladium membrane heated to 500°C. The amount of hydrogen was measured from the pressure difference in the system before and after removing hydrogen from the gaseous products.

The results of this experiment to study the effusion of hydrogen from an *a*-C:H film are plotted in Fig. 1 (curve *1*). Also plotted is the temperature dependence of the release of the remaining (apart from hydrogen) gaseous products (curve *2*), which may include traces of argon (used as diluent gas) trapped in the structural framework of the carbon during growth of the film or absorbed on the surfaces of microinhomogeneities (such as pores, column and grain boundaries, and so forth) and thus not forming a chemical bond with the carbon. We estimated that the argon concentration did not exceed 10^{-4} at.%. In addition to argon, these gaseous products may also include methane and more complex hydrocarbons formed in the plasma during decomposition of the methane and trapped in the film like the argon. All gases trapped or absorbed in the carbon structure but not bonded chemically with the carbon will subsequently be described as gases in state ''A.''

In addition to argon and other gases, obviously a certain amount of hydrogen may also be in state A. Regardless of whether it is in molecular or atomic form, this hydrogen will be described as free.

As the film material is heated, hydrogen is released in stages: first, hydrogen in state A, then weakly chemically bound hydrogen, and then strongly bound hydrogen with rearrangement of the carbon matrix structure. We examined the mechanism for this process in Ref. 4.

At low temperatures (but higher than the film formation temperature T_s), hydrogen from state A begins to be released, since this is the most weakly bound. The infrared spectroscopy data indicate that no transformation of the film structure occurs at this stage. At temperatures of 100–300°C the magnitude, position, and half-width of the absorption bands, 2920 and 1450 cm^{-1} (CH_2), 2950, 2860, and 1370 cm^{-1} (CH_3) remain constant. However, when the samples are annealed to 400°C, the refractive index at 20°C is increased from 1.56 to 1.62. This indicates that the density of the film is increased with the existing chemical bonds being conserved. This process corresponds to the initial gently sloping section of the gas release curve at annealing temperatures up to 300–400°C (see Fig. 1, curve *1*).

The release of hydrogen from state A may be estimated quantitatively by comparing the curve giving the release of the nonhydrogen component from state A (curve *2*) and the initial section of the hydrogen release curve (curve *1*). At low temperatures (20–200°C), the gas release curves should be described by the same law for both components and the

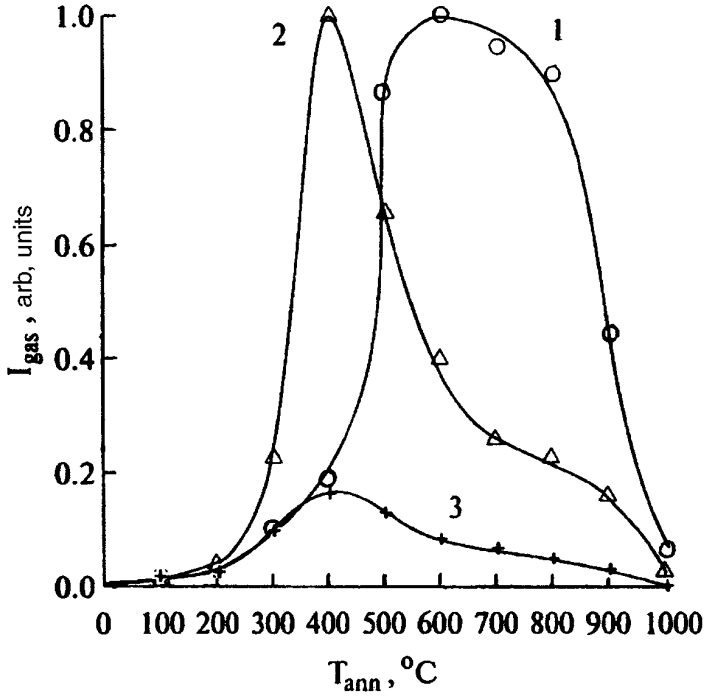

FIG. 1. Effusion of the gaseous component from amorphous carbon films versus temperature: curve *1* — total for hydrogen, curve *2* — all gaseous components except hydrogen, curve *3* — free hydrogen.

general form of the release curves for hydrogen and the nonhydrogen component from state A should be the same at all temperatures in the range. The curve describing the release of hydrogen from state A, i.e., atomic and molecular free hydrogen, obtained on the basis of this agreement is plotted (curve *3*).

The peaks and nonmonotonicities observed on this curve should correspond to an increased rate of hydrogen release (as well as argon and other gases) from state A accompanying rearrangement of the carbon structure. These features may be observed as a peak at 400°C, a tail at 550–600°C, and a weak peak at 800°C.

The areas below the curves can be used to estimate the amount of free hydrogen in our *a*-C:H samples as 4 at.% and the amount of bound hydrogen (i.e., in C–H bonds) as 22 at.%. An analysis of the infrared spectroscopy data gives the amount of bound hydrogen in these samples as 21 at.%. It should be noted that the amount of free hydrogen in our films is not large compared with its total content.

At temperatures above 400°C the carbon structure undergoes rearrangement with initially weak and then stronger C–H bonds being broken. When the samples are annealed to 800 °C, the refractive index is increased to 1.8 and the intensity of all these infrared absorption bands falls to the measurement limit. In this case we observe a broad hydrogen release peak (see Fig. 1) which can be resolved fairly accurately into two peaks with temperature maxima of 500 and 750°C. This rearrangement of the structure is also accompanied by release of hydrogen from state A.

According to published data, the first peak, whose maximum fluctuates between 300 and 500°C according to different authors, is associated with effusion of hydrogen from adjacent sites[5] or breaking of weak C–H bonds in polymer chains.[6,7] The amount of hydrogen thus released is of the order of 10 at.%.

The second peak, observed at temperatures higher than 700°C is generally associated with breaking of strong C–H bonds[5,7,8] and transformation of the material to give a graphite-like structure. The amount of hydrogen released by breaking of strong C–H bonds is of the order of 12 at.%.

In summary, we have investigated the effusion of hydrogen and other gases from an *a*-C:H film annealed at temperatures of 100–1000°C. A direct method has been used to determine the amount of hydrogen in the material as 26 at.%. The amount of free hydrogen in the material has been estimated as 4 at.% and its gas release temperature curve has been obtained with a maximum at 400°C. Two effusion peaks have been identified for bound hydrogen, the first associated with breaking of weak C–H bonds, with a maximum at 500°C, and 10 at.% of hydrogen released, and the second associated with breaking of strong C–H bonds, with a maximum at 750°C and 12 at.% of hydrogen released.

This work was partly supported by grants from the Ministry of Science, No. 1S91.1LFO20, the Russian Fund for Fundamental Research, No. 96-02-16851-a, and the University of Arizona, USA.

[1] B. Discher, A. Burenzer, and P. Koidl, Solid State Commun. **48**, 105 (1983).
[2] A. Grill and V. Patel, Appl. Phys. Lett. **60**, 2089 (1992).
[3] J. Ataev, O. I. Konkov, E. I. Terukov, V. A. Vassilev, and A. S. Volkov, Phys. Status Solidi A **120**, 519 (1990).
[4] I. N. Trapeznikova, O. I. Konkov, E. I. Terukhov, and S. G. Yastrebov, Fiz. Tverd. Tela (St. Petersburg) **36**, 1519 (1994) [Phys. Solid State **36**, 2780 (1994)].
[5] J. Robertson, Progr. Solid State Chem. **21**, 199 (1992).
[6] W. Beyer and H. Wagner, J. Appl. Phys. **53**, 8745 (1982).
[7] S. Logothetidic, G. Kiriakidis, and E. C. Palowra, J. Appl. Phys. **70**, 2791 (1991).
[8] S. Logothetidic, G. Petalas, and S. Ves, J. Appl. Phys. **79**, 1040 (1996).

Translated by R. M. Durham